TURUN
YLIOPISTO
UNIVERSITY
OF TURKU

NOVEL PET IMAGING APPROACHES FOR NEURODEGENERATIVE DISEASE PROGRESSION

Saeka Shimochi

TURUN YLIOPISTON JULKAISUJA – ANNALES UNIVERSITATIS TURKUENSIS
SARJA – SER. D OSA – TOM. 1833 | MEDICA – ODONTOLOGICA | TURKU 2024

TURUN
YLIOPISTO
UNIVERSITY
OF TURKU

NOVEL PET IMAGING APPROACHES FOR NEURODEGENERATIVE DISEASE PROGRESSION

Saeka Shimochi

TURUN YLIOPISTON JULKAISUJA – ANNALES UNIVERSITATIS TURKUENSIS
SARJA – SER. D OSA – TOM. 1833 | MEDICA – ODONTOLOGICA | TURKU 2024

University of Turku

Faculty of Medicine
Department of Clinical Physiology and Nuclear Medicine
Doctoral Programme in Clinical Research
Turku PET Centre
MediCity Research Laboratory

Supervised by

Adjunct Professor Tove Grönroos, PhD
Turku PET Centre
University of Turku
Turku, Finland

Adjunct Professor Emrah Yatkin, DVM, PhD, Director
Central Animal Laboratory
University of Turku
Turku, Finland

Visiting Professor Hidehiro Iida, PhD
Turku PET Centre
University of Turku
Turku, Finland

Reviewed by

Research Director Patricia Iozzo, MD, PhD
Institute of Clinical Physiology
National Research Council (CNR)
Pisa, Italy

Professor Olof Eriksson, PhD
Department of Medicinal Chemistry
Uppsala University
Uppsala, Sweden

Opponent

Professor Gitte Moos Knudsen, MD, PhD
Department of Clinical Medicine
Faculty of Health and Medicine
University of Copenhagen
Copenhagen, Denmark

ISBN 978-951-29-9998-9 (PRINT)
ISBN 978-951-29-9999-6 (PDF)
ISSN 0355-9483 (Print)
ISSN 2343-3213 (Online)
Painosalama, Turku, Finland 2024

UNIVERSITY OF TURKU
Faculty of Medicine
Clinical Physiology and Nuclear Medicine
Turku PET Centre
SAEKA SHIMOCHI: Novel PET Imaging Approaches for
Neurodegenerative Disease Progression
Doctoral Dissertation, 131 pp.
Doctoral Programme in Clinical Research
December 2024

ABSTRACT

Neuropathic pain (NPP) and neonatal hypoxic–ischaemic encephalopathy (HIE) both have a limited understanding of neurological damage onset and progression, hampering the development of novel treatments. This thesis evaluated the feasibility of preclinical positron emission tomography (PET) imaging for tracking time-dependent pathophysiological alterations in NPP and HIE animal models.

PET imaging using the 18-kDa translocator protein tracer [^{18}F]F-DPA was conducted to evaluate gliosis-mediated inflammation in the spinal cord of a rat model of NPP. A new PET setup was used to assess brain oxygen metabolism in a rat model of HIE, in which ^{15}O-labelled gases are inhaled spontaneously by rat neonates, enabling a quantitative assessment of cerebral blood flow (CBF) and cerebral metabolic rate of oxygen ($CMRO_2$). The pathophysiological progression of HIE was longitudinally assessed by PET targeting inflammation ([^{18}F]F-DPA), hypoxia ([^{18}F]EF5), and uptake of the glucose analogue ([^{18}F]FDG). [^{15}O]O_2 and [^{18}F]FDG uptake levels within 48 h after hypoxic–ischaemic injury were further compared with the outcome of histological brain volume loss in a later phase.

[^{18}F]F-DPA showed specific uptake in the inflamed spinal cord on *ex vivo* PET and autoradiography 7 days after injury in NPP rats. *In vivo* PET did not allow for visualisation of the inflammation site due to insufficient [^{18}F]F-DPA uptake in the lesion and high background noise. The ^{15}O-labelled gas PET setup detected temporal changes in CBF and $CMRO_2$ associated with acute perfusion derangement within 48 h post-insult and tissue damage progression in HIE over 14 days along with maturation. On the injury day, transiently enhanced hypoxic and glucose uptake brain areas were detected, whereas inflammatory responses emerged 4 days post-injury and remained elevated until day 21. PET with [^{18}F]FDG and [^{15}O]O_2 within 48 h post-insult showed predictive values for early recognition of damage severity. This thesis highlights the utility and limitations of preclinical PET techniques for the development of advanced diagnostic, prognostic, and therapeutic approaches for NPP and neonatal HIE.

KEYWORDS: PET, neuropathic pain, neonatal hypoxic–ischaemic encephalopathy, animal model, neuroinflammation, hypoxia, glucose metabolism, oxygen metabolism

TURUN YLIOPISTO
Lääketieteellinen tiedekunta
Kliininen fysiologia ja isotooppilääketiede
Turun PET-keskus
SAEKA SHIMOCHI: Neurodegeneratiivisten sairauksien etenemisen seuranta PET-kuvantamisella
Väitöskirja, 131 s.
Turun kliininen tohtoriohjelma
Joulukuu 2024

TIIVISTELMÄ

Neuropaattinen kipu (NPP) ja vastasyntyneiden hypoksis-iskeeminen enkefalopatia (HIE) ovat keskushermostovaurioita, joiden synty- ja etenemismekanismeista on rajallisesti tietoa. Tämä vaikeuttaa uusien hoitomuotojen kehittämistä. Tässä väitöskirjassa arvioidaan positroniemissiotomografia (PET)-kuvantamismenetelmän käyttökelpoisuutta NPP- ja HIE-eläinmallien patofysiologisten muutosten seuraamisessa.

NPP-eläinmallin selkäytimessä ilmenevää glioosivälitteistä tulehdusta kuvannettiin TSPO/PET-merkkiaineella, [^{18}F]F-DPA:lla. Aivojen verenvirtausta (CBF) ja hapen aineenvaihduntatasoa ($CMRO_2$) mitattiin kvantitatiivisesti HIE-mallin rotan poikasissa käyttämällä tutkimusta varten kehitettyä ^{15}O- kaasulaitteistoa. HIE-vaurion patofysiologista etenemistä tutkittiin PET-kuvantamisella myös pitkittäisseurannassa tulehduksen ([^{18}F]F-DPA), hypoksian ([^{18}F]EF5), ja glukoosianalogikertymän ([^{18}F]FDG) osalta. Lisäksi verrattiin [^{15}O]O_2:n ja [^{18}F]FDG:n kertymiä 48 tuntia HIE-vaurion jälkeen myöhempään histologisesti määritettyyn aivovaurion laajuuteen.

[^{18}F]F-DPA:lla osoitettiin spesifinen kertymä rottien selkäytimen tulehdusalueella radioaktiivisuuden *ex vivo* kudosmittauksella ja alueen kudosleikkeiden autoradiografiamenetelmällä 7 päivää NPP-vaurion jälkeen. *In vivo* PET-kuvantamisella tulehdusaluetta ei kuitenkaan havaittu, koska pienen vaurioalueen matala radioaktiivisuuskertymä ei erottunut riittävästi taustakertymästä. ^{15}O-leimatuilla kaasuilla osoitettiin HIE-vaurion aiheuttamat vakavat perfuusioon liittyvät CBF:n ja $CMRO_2$:n muutokset 14 päivän ajan vauriosta. Vauriopäivänä havaittiin aivoalueita, joissa esiintyi tilapäistä hypoksiaa ja lisääntynyttä glukoosikertymää. Tulehdusvaste ilmaantui vasta neljä päivää vauriosta ja pysyi koholla 21 päivän ajan. PET-kuvantamisella 48 tunnin sisällä NPP-vauriosta [^{15}O]O_2:lla ja [^{18}F]FDG:llä osoitettiin olevan ennustearvoa vaurion myöhempään vakavuusasteeseen. Tämä työ osoittaa prekliinisen PET-kuvantamismenetelmän käyttökelpoisuuden NPP- ja HIE-vaurioiden uusien diagnostisten, ennusteellisten ja terapeuttisten menetelmien kehittämisessä.

AVAINSANAT: PET, neuropaattinen kipu, vastasyntyneiden hypoksis-iskeeminen enkefalopatia, eläinmalli, neuroinflammaatio, hypoksia, glukoosiaineenvaihdunta, happiaineenvaihdunta

Table of Contents

Abbreviations **8**

List of Original Publications **10**

1 Introduction **11**

2 Review of the Literature **14**
2.1 NPP 14
2.1.1 Pathogenesis of NPP 14
2.1.2 NPP animal models 16
2.2 Neonatal HIE 17
2.2.1 Pathogenesis and treatment of neonatal HIE 18
2.2.2 Neonatal HIE animal model 19
2.3 PET imaging 20
2.3.1 The PET principle 20
2.3.2 Small animal PET imaging 22
2.4 Neuroinflammation 23
2.4.1 TSPO as a biomarker of neuroinflammation 24
2.4.2 TSPO PET tracers 24
2.5 Cerebral oxygen metabolism 25
2.5.1 PET with [^{15}O]-labelled gases 25
2.5.2 Calculation of oxygen metabolism from PET images 26
2.6 Cerebral hypoxia 26
2.6.1 PET tracers targeting hypoxic tissues 27
2.7 Cerebral glucose metabolism 27
2.7.1 PET tracer targeting glucose metabolism 27
2.7.2 PET imaging of cerebral [^{18}F]FDG in HIE 28

3 Aims **29**

4 Materials and Methods **30**
4.1 Experimental design (I–III) 30
4.2 Animal models (I–III) 32
4.2.1 NPP model (I) 32
4.2.2 Neonatal HIE model (II, III) 33
4.3 Pain sensation test (I) 34
4.4 Radionuclide and PET tracer production (I–III) 34
4.5 PET/CT imaging (I–III) 37
4.6 The integrated ^{15}O-gas PET system (II) 37
4.6.1 Metabolism of inhaled [^{15}O]O_2 38
4.6.2 PET imaging with [^{15}O]-labelled gases 39

4.7 PET data processing (I–III) 40
4.8 PET data analysis (I–III) 40
4.9 *Ex vivo* biodistribution (I) 41
4.10 *Ex vivo* ARG (I, III) 42
4.11 Specificity of [^{18}F]F-DPA for targeting TSPO (I, III) 43
4.12 Histology and IHC (I–III) 43
4.13 Statistical analysis (I–III) 44

5 Results 46
5.1 Characterisation of the NPP animal model 46
5.2 Assessment of the inflamed region 46
5.2.1 PET imaging of the inflamed spinal cord region 47
5.2.2 ^{18}F radioactivity uptake in tissues 48
5.2.3 Localisation of inflamed area 48
5.3 Production rate of metabolised [^{15}O] H_2O (k_w) 49
5.4 Evaluation of ^{15}O-labelled gas PET system 50
5.5 PET findings in neonatal HIE 51
5.5.1 Temporal changes in CBF and $CMRO_2$ 51
5.5.2 *In vivo* PET evaluation of pathological progression 53
5.5.3 *Ex vivo* localisation of brain pathology 54
5.6 Histopathology of HIE brains 55
5.7 Predictive value of *in vivo* PET 56

6 Discussion 57
6.1 Assessment of PET imaging of the NPP model 57
6.1.1 *Ex vivo* findings 57
6.1.2 *In vivo* findings 57
6.1.3 Challenges in NPP PET imaging 58
6.2 Methodological advantages of [^{15}O]gas PET imaging 60
6.2.1 Quantification using a non-invasive approach 60
6.2.2 Defining the k_w value 61
6.2.3 Implementation of [^{15}O]gas PET in HIE 61
6.3 Pathophysiological findings of neonatal HIE 62
6.3.1 Changes in CBF and $CMRO_2$ 63
6.3.2 Hypoxic brain areas 63
6.3.3 Changes in brain [^{18}F]FDG uptake 64
6.3.4 Inflammatory response 65
6.3.5 Predictive value of PET for neonatal HIE 65
6.4 Limitations and future perspectives 66
6.4.1 Limitations 66
6.4.2 Alternative PET tracers for neuroinflammation 68
6.4.3 Future technical perspectives 68
6.4.4 Animals 69
6.4.5 Anaesthesia 70

7 Conclusions 71

Acknowledgements 72

References 75

Original Publications 85

Abbreviations

[^{18}F]FDG	2-Deoxy-2-[^{18}F]fluoro-D-glucose
AIF	Arterial input function
A_m	Molar activity
ANOVA	Analysis of variance
ARG	Autoradiography
ARRIVE	Animal Research: Reporting of *In Vivo* Experiments
BBB	Blood–brain barrier
BDNF	Brain-derived neurotrophic factor
CBF	Cerebral blood flow
CBV	Cerebral blood volume
CCI	Chronic constriction injury
CCL-21	Chemokine C-C motif ligand 21
CMRglc	Cerebral metabolic rate of glucose
$CMRO_2$	Cerebral metabolic rate of oxygen
CNS	Central nervous system
CSF-1	Colony-stimulating factor 1
CT	Computed tomography
DAMP	Damage-associated molecular pattern
FOV	Field of view
GFAP	Glial fibrillary acidic protein
GLUT	Glucose transporter
GMP	Good Manufacturing Practise
H&E	Haematoxylin and eosin
HI	Hypoxic–ischaemic
HIE	Hypoxic–ischaemic encephalopathy
HIV	Human immunodeficiency virus
HPLC	High-performance liquid chromatography
Iba1	Ionized calcium-binding adapter molecule 1
I/C	Ipsi-/contralateral
IHC	Immunohistochemistry
IL-1β	Interleukin 1β

i.v.	Intravenous
Ki	Inhibitory constant (binding affinity)
k_w	Production rate of metabolised $[^{15}O]H_2O$
L/T	Lumbar/thoracic
LV	Left ventricle
MAP2	Microtubule-associated protein 2
MCAO	Middle cerebral artery occlusion
MRI	Magnetic resonance imaging
NeuN	Neuronal nuclei
NLLSF	Non-linear least squares fitting
NPP	Neuropathic pain
P	Postnatal day
p.i.	Post-injection
P2X4R	Purinergic 2 type X subtype 4 receptor
P2X7R	Purinergic 2 type X subtype 7 receptor
PET	Positron emission tomography
PBS	Phosphate-buffered saline
PBR	Peripheral benzodiazepine receptor
PSL	Photostimulated luminescence
PSNL	Partial sciatic nerve ligation
SCI	Spinal cord injury
SD	Standard deviation
SNI	Spared nerve injury
SNL	Spinal nerve ligation
SUV	Standardised uptake value
SUV_{max}	Maximum standardised uptake value
T½	Half life
TAC	Time-activity curve
TNF-α	Tumor necrosis factor-α
TSPO	18-kDa Translocator protein
VOI	Volume of interest
3D OSEM	Three-dimensional ordered-subsets expectation–maximisation

List of Original Publications

This dissertation is based on the following original publications, which are referred to in the text by their Roman numerals:

I **Shimochi S**, Keller T, Kujala E, Khabbal J, Rajander J, Löyttyniemi E, Solin O, Nuutila P, Kanaya S, Yatkin E, Grönroos TJ, Iida H. Evaluation of [^{18}F]F-DPA PET for Detecting Microglial Activation in the Spinal Cord of a Rat Model of Neuropathic Pain. *Mol Imaging Biol*. 2022; 24:641650.

II **Shimochi S**, Ihalainen J, Parikka V, Kudomi N, Tolvanen T, Hietanen A, Kokkomäki E, Johansson S, Tsuji M, Kanaya S, Yatkin E, Grönroos TJ, Iida H. Small animal PET with spontaneous inhalation of ^{15}O-labelled oxygen gases: Longitudinal assessment of cerebral oxygen metabolism in a rat model of neonatal hypoxic-ischaemic encephalopathy. *J Cereb Blood Flow Metab.* 2024; 44:1024–1038.

III Saha E, **Shimochi S**, Keller T, Eskola O, López-Picón F, Rajander J, Löyttyniemi E, Forsback S, Solin O, Grönroos TJ, Parikka V. Evaluation of PET imaging as a tool for detecting neonatal hypoxic-ischemic encephalopathy in a preclinical animal model. *Exp Neurol*. 2024; 373:114673.

1 Introduction

Positron emission tomography (PET) is a non-invasive molecular imaging modality that allows spatiotemporal tracking of the *in vivo* biodistribution of molecules labelled with positron-emitting radionuclides (Krishnamoorthy *et al*., 2017). In the study of neurodegenerative diseases, primarily characterised by progressive loss of neuronal function and structure leading to sensory, motor, and cognitive disabilities (Martin, 1999), *in vivo* PET monitoring may detect harmful physiological events before they cause irreversible damage to the central nervous system (CNS), thereby guiding personalised therapy with subsequent follow-up (Barthel *et al*., 2022). To date, small animal PET has been widely used to identify background mechanisms, including disease onset and progression, and to study the efficacy of novel therapeutic strategies in translational contexts utilising favoured animal models for a wide range of neurodegenerative diseases.

Neuropathic pain (NPP) is a chronic condition that occurs after nerve damage from, e.g. cancer, infection, trauma, and diabetes (Jensen *et al*., 2011). The currently available clinical treatment has only partial analgesic effects, often leading to impaired quality of life. Pain is a subjective expression of a pathological condition that varies widely among individuals; therefore, a robust biomarker and diagnostic tool that accurately identifies NPP and treatment responses would be highly valuable. Accumulated evidence has linked NPP and microglia-mediated neuroinflammation in the spinal cord evoked by peripheral nerve injury (Tsuda *et al*., 2003). A previous report demonstrated that increased expression of the 18-kDa translocator protein (TSPO) in reactive microglia can be quantitatively detected in the spinal cord of a rat model of NPP, generated by partial sciatic nerve ligation, using the first-generation TSPO tracer, [^{11}C]PK11195 (Imamoto *et al.,* 2013). However, the achieved target/reference SUV ratio was only ~1.5, which might be insufficient to monitor changes in the progressive inflammation and healing process. In addition, carbon-11 has disadvantage properties, such as a limited half-life (T½ = 20 min) and a relatively high positron range in tissues leading to a reduced image quality. The newly-developed second-generation TSPO-specific radioligand, [^{18}F]F-DPA is advantageous over [^{11}C]PK11195 due to its higher binding affinity for TSPO and lower nonspecific binding potential (Keller *et al*., 2017). The lower positron

range and longer half-life (T½ = 109.8 min) of fluorine-18 are also advantageous. Thus, [^{18}F]F-DPA combined with a state-of-the-art (spatial resolution <1.0 mm) small animal PET scanner (Molecubes) may allow for robust *in vivo* identification of glial activation in small lesions in the spinal cord, as well as highly sensitive detection of its changes over time.

Neonatal hypoxic–ischaemic encephalopathy (HIE) is a common brain injury in newborns caused by impaired cerebral blood flow (CBF) and oxygen delivery to the brain at birth, resulting in neonatal death or life-long disabilities, such as cerebral palsy (Greco *et al*., 2020). Therapeutic hypothermia within 6 h after birth in cases of an incident is the sole effective and approved neuroprotective treatment in clinics, but the outcomes remain highly variable (Jacobs *et al*., 2013). Although novel therapies that may be an adjunct or alternative to therapeutic hypothermia have been extensively explored, high interindividual variability in brain damage severity and its worsening or healing course remains a major obstacle to consistent monitoring of prognosis in both preclinical and clinical settings. Thus, reliable diagnostic and prognostic indicators are highly desired to identify high-risk neonates, particularly in the acute phase.

One of the challenges in patients with HIE is to identify abnormal cerebral metabolic changes associated with deranged cerebral perfusion and oxygenation after a hypoxic–ischaemic (HI) event, as all of these cause an increased risk of irreversible tissue injury, which is further mediated by inflammatory responses. PET with ^{15}O-labelled gas inhalation is a commonly used diagnostic method in clinics for assessing cerebral perfusion and oxygen metabolism in several ischaemic disorders like stroke. Nevertheless, technical complexities, such as the need for tracheotomy and repeated arterial blood sampling (Temma *et al*., 2008; Watabe *et al*., 2013), have hindered its preclinical application. Recently, Temma *et al.* (2017) developed a novel PET method that enables the spontaneous inhalation of ^{15}O-labelled gases without the need for tracheotomy in mice. [^{15}O]O_2 gas is the sole tracer that captures cellular oxygen metabolism, directly reflecting neuronal loss or survival. Together with [^{15}O]CO_2, holding equivalent kinetics to intravenous (i.v.) [^{15}O]H_2O, repetitive and fully quantitative assessment of cerebral metabolic variables with tissue perfusion after HI insult could be achieved using a minimally invasive protocol. Additionally, PET targeting hypoxia ([^{18}F]EF5), uptake of the glucose analogue ([^{18}F]FDG), and neuroinflammation ([^{18}F]F-DPA) may help identify the temporal profile of the evolution and maintenance of brain injury and find solutions for therapeutically modulating them. Non-invasive *in vivo* PET measurement may also allow for early recognition of risk factors that impact poor outcomes, which is critical when selecting infants requiring timely interventions.

Hence, this thesis aimed to demonstrate whether small animal PET can non-invasively monitor disease progression in two different neurodegenerative disease

models using PET tracers targeting multiple pathophysiological processes. The work in this thesis describes the evaluation of the TSPO tracer [^{18}F]F-DPA to target small inflamed lesions in the spinal cord of an NPP rat model (**I**). In addition, a novel small animal ^{15}O-labelled gas inhalation PET system was installed, enabling the non-invasive and fully quantitative monitoring of oxygen metabolic changes related to brain damage processes in a neonatal HIE animal model (**II**). Finally, HIE damage progression was further longitudinally monitored for pathophysiological changes in tissue hypoxia, glucose uptake, and neuroinflammation using [^{18}F]EF5, [^{18}F]FDG, and [^{18}F]F-DPA, respectively (**III**). The outline and relationships of studies **I-III** to each other are shown in Figure 1.

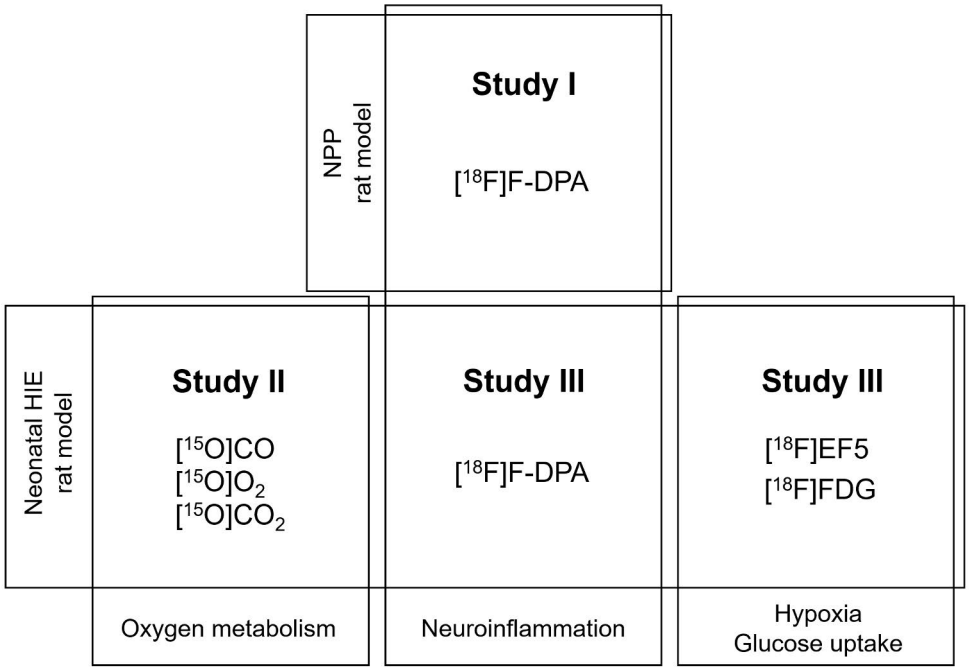

Figure 1. Interrelationships among studies **I–III**.

2 Review of the Literature

2.1 NPP

According to the International Association for the Study of Pain, NPP is defined as 'pain caused by a lesion or disease of the somatosensory nervous system' (Jensen *et al*., 2011). Unlike nociceptive or inflammatory pain, NPP typically stems from peripheral or central nerve injury due to diverse aetiologies, such as diabetic neuropathy, cancer, chemotherapy, autoimmune disease (e.g. multiple sclerosis), infection (e.g. HIV, herpes), and trauma, resulting in a pathologically deranged somatosensory nervous system (Karimi *et al*., 2024). Patients experience unpleasant sensations, including spontaneous pain and exaggerated pain sensitivity evoked by painful stimuli (hyperalgesia) or even normal non-painful stimuli (allodynia) (Karimi *et al*., 2024). These symptoms often persist even after the primary cause has healed due to the disordered transmission of somatosensory signals to the CNS. It affects up to 10% of the general population worldwide with the characteristics of NPP (Colloca *et al*., 2017; van Hecke *et al*., 2014; Murnion, 2018). Robust diagnosis and management of NPP are often challenging. Pain symptoms are usually subjective manifestations of pathological conditions, and there is considerable individual variation in pain perception and tolerance, even among patients with the same primary cause of NPP. Furthermore, it is often resistant to commonly used pain-relief drugs like nonsteroidal anti-inflammatory drugs, opioids, and acetaminophen, which may even have undesirable side effects and leave patients in significant distress and disability (Scholz *et al*., 2019). Consequently, NPP is a considerable socioeconomic burden, so there is an urgent need to spur the development of novel non-invasive diagnostic and effective therapeutic modalities.

2.1.1 Pathogenesis of NPP

Under normal conditions, acute nociceptive pain plays an important role in sensing dangerous stimuli that threaten physiological homeostasis. External noxious stimuli are transferred through dorsal root ganglion neurones into the dorsal horn of the spinal cord (Figure 2). Pain information is then transmitted through nervous fibres that cross to the opposite side of the spinal cord, ascending the lateral column to the

thalamus, and finally to the cerebral cortex, where pain sensation is perceived (Scholz and Woolf, 2002). In patients with NPP, peripheral nerve injury due to diverse primary causes evokes aberrant excitability of the nervous system, especially in the primary afferent neurone and in the dorsal horn of the spinal cord, leading to hyperalgesia or allodynia (Scholz and Woolf, 2002).

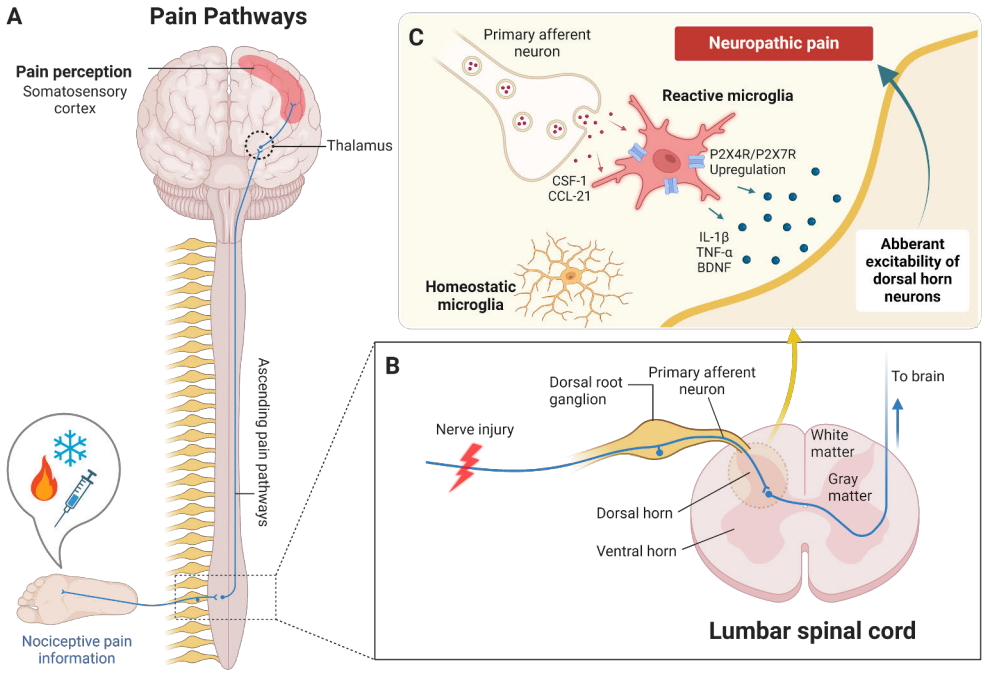

Figure 2. Pathogenesis of NPP involving spinal microglial reactivity after peripheral nerve injury. Acute nociceptive pain stimuli under normal conditions are transmitted via dorsal root ganglion neurones to secondary sensory neurones in the spinal dorsal horn, travelling up to the somatosensory cortex and eliciting potential defensive actions against pain sensation (**A**). Under pathophysiological conditions, peripheral nerve injury causes spinal dorsal horn microgliosis (**B**), in which overexpression of P2X4R/P2X7R triggers various pain-inducing responses by releasing mediators like BDNF (**C**). This aberrant excitability of the spinal nervous system triggers even innocuous tactile stimuli that evoke painful sensations. *Modified from Tsuda et al. (2013) and Inoue and Tsuda (2018) using BioRender.com.*

Accumulating evidence has suggested a notable role for spinal microgliosis elicited by peripheral nerve injury, with morphological and gene expression changes, in the development and maintenance of NPP (Kohno *et al*., 2022). Peripheral nerve injury causes excitability of primary afferent neurones, releasing a variety of mediators such as colony-stimulating factor 1 (CSF-1) and chemokine C-C motif ligand 21 (CCL-21), which can activate receptors on microglia. Recently,

upregulation of purinergic P2X4 receptors (P2X4R) and P2X7R on reactive microglia in the spinal cord has been noted, releasing mediators such as brain-derived neurotrophic factor (BDNF), tumor necrosis factor α (TNF-α), and interleukin 1β (IL-1β), which are responsible for the aberrant excitability of spinal dorsal horn neurones (Tsuda *et al*., 2003). It has also been demonstrated that inhibition of microglia-mediated inflammation in the dorsal horn of the spinal cord, in particular inactivating spinal P2X4R/P2X7R, results in resilience against hyperalgesia and allodynia induced by peripheral nerve injury (Echeverry *et al*., 2017; Tsuda *et al*., 2003; Huang *et al*., 2017).

2.1.2 NPP animal models

While diagnostic imaging and quantitative pain sensory testing provide important information on the pathophysiological aspects of pain in patients, current knowledge on the mechanism of NPP development is largely based on studies using animal models (Scholz *et al*., 2019). Given the multiple aetiological factors causing NPP, various rodent models have been developed to identify the underlying pathogenic mechanisms and potential drug targets (Jaggi *et al*., 2011). Among them, the sciatic nerve injury model has been most frequently employed because of its readily reproducible characteristics (Lee *et al*., 2000), including the chronic constriction injury (CCI) (Bennett and Xie, 1988), partial sciatic nerve ligation (PSNL) (Seltzer *et al.*, 1990), spinal nerve ligation (SNL) (Ho Kim and Mo Chung, 1992), and spared nerve injury (SNI) (Decosterd and Woolf, 2000) models (Figure 3). Such peripheral nerve injury generates chronic abnormal pain perception in the hind paw due to hypersensitivity to mechanical, heat, and cold stimuli. Upregulated spinal glia in the dorsal horn have been implicated in all sciatic nerve ligation models (He *et al*., 2012; Echeverry *et al*., 2017; Narita *et al*., 2006; Tsuda *et al*., 2003; Kobayashi *et al*., 2012) as well as disease-specific neuropathy models, such as the Streptozotocin model of diabetic neuropathy (Tsuda *et al*., 2008; Wodarski *et al*., 2009) and experimental autoimmune neuritis (Zhang *et al*., 2008). Echeverry *et al.* (2017) revealed that sciatic nerve injury-triggered pain hypersensitivity persists long-term (>3 months) in the PSNL rat model and is maintained by spinal glial activation.

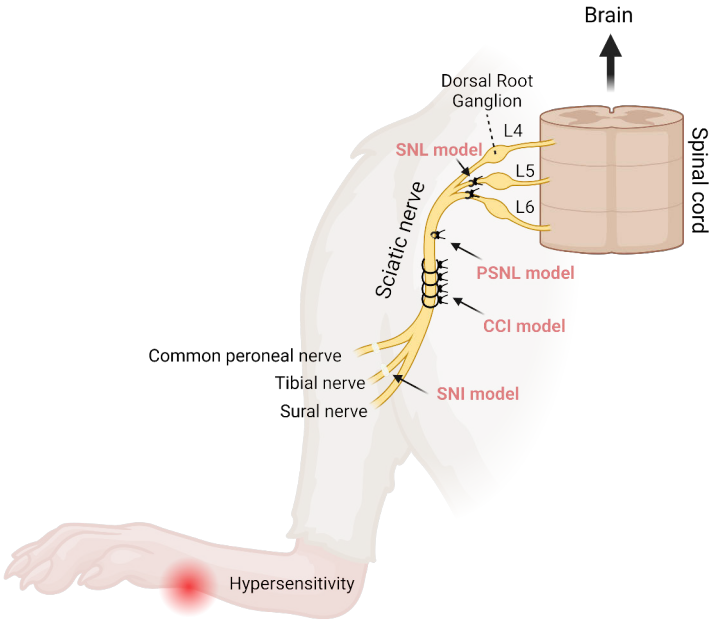

Figure 3. Illustration showing different sciatic nerve injury animal models commonly used. SNL is caused by tight ligation of the entire spinal segmental nerve. The PSNL model involves a single tight ligation of a part of the sciatic nerve, whereas the CCI model involves four loose ligations around the entire sciatic nerve. SNI is caused by injury to two of the three terminal branches of the sciatic nerve. *Created using BioRender.com.*

2.2 Neonatal HIE

HIE is a serious birth complication among neonates caused by impaired blood flow (ischaemia) and oxygen delivery (hypoxia) to the foetus or newborn brain during the prenatal, intrapartum, or postnatal period, leading to acute mortality and long-term neurological disabilities. The estimated incidence of live full-term birth is 1.5 per 1000 in developed countries, increasing up to 10–20 per 1000 children in developing countries due to limited diagnostic and interventional possibilities (Greco *et al*., 2020; Kurinczuk *et al*., 2010). Perinatal asphyxia contributing to neonatal HIE originates from a variety of circumstances during pregnancy, labour, delivery, or post-delivery, such as placental abruption, umbilical cord compression, uterine rupture, maternal hypotension, infection, or cardiac and respiratory failure after birth (Yıldız *et al*., 2017). The mortality rate of newborns with moderate and/or severe HIE is more than 10% worldwide, and up to 25% of survivors will suffer from permanent neurodevelopmental handicaps, including cerebral palsy, epilepsy, attention deficit hyperactivity disorder, or learning disability (Selway, 2010). Therapeutic hypothermia is currently the standard treatment worldwide and the sole approved therapeutic intervention for infants with HIE, but it has limited benefits,

especially in severe cases (Jacobs *et al*., 2013). Thus, neonatal HIE represents a significant and life-long burden for patients, families, and society. Understanding the pathophysiology of perinatal HI brain damage is essential for the design of effective and timely therapeutic interventions.

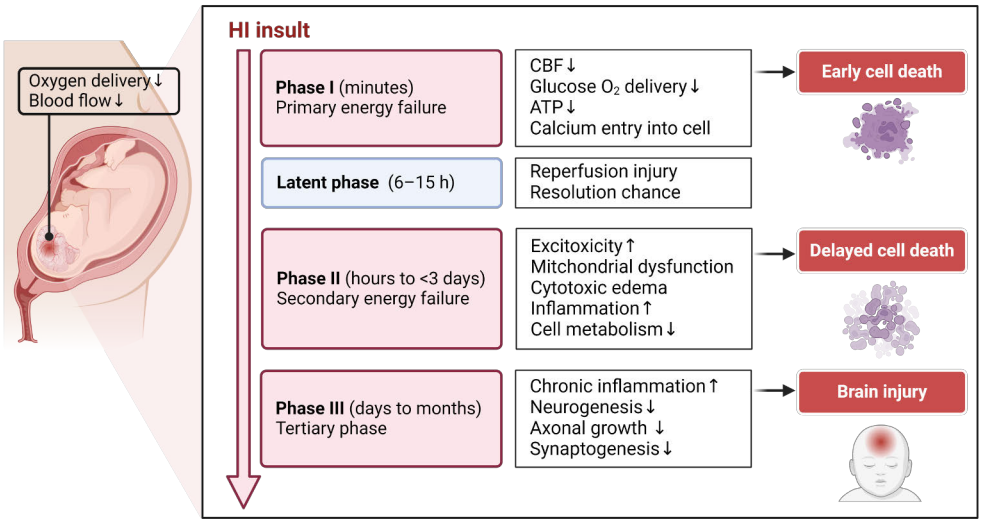

Figure 4. Development process of neonatal HIE. HI injury occurs after a decrease in oxygen delivery and blood flow to the neonatal brain, leading to the development of three distinct pathophysiological phases (I–III) that appear in hours, days, and even months. Immediately after injury (phase I), early cell death (necrosis) occurs, followed by a latent phase in which mild HIE may resolve without treatment. Following reperfusion in phase II, cell metabolism decreases and excitotoxicity increases, leading to delayed cell death (apoptosis/necrosis). Initial inflammatory responses become chronic in phase III, leading to neuronal loss and brain injury. *Modified from Dixon et al. (2015) and Nair and Kumar (2018) using BioRender.com.*

2.2.1 Pathogenesis and treatment of neonatal HIE

Impaired oxygen delivery to the brain around the time of birth often combined with reduced CBF due to compromised circulation causes a pathophysiological cascade of brain damage that can last from minutes to days or even months and years (Greco *et al*., 2020). This injury-evolving process can be divided into three main phases: primary energy failure, secondary energy failure, and tertiary energy failure, as illustrated in Figure 4. The initial hypoperfusion followed by rapid reperfusion with transient energy recovery can have deleterious effects on brain tissues, known as reperfusion injury (Lin *et al*., 2016). Most therapeutic approaches for neonatal HIE aim to prevent the cascade of these events occurring in the so-called ‘therapeutic time window’, which starts with reperfusion and leads to secondary energy failure of oxidative metabolism when delayed neuronal death occurs. Therapeutic

hypothermia, which lowers a patient's head or whole-body temperature to 33.5°C, aims to reduce cellular energy metabolism and should be typically initiated within 6 h after birth to restore cellular metabolic function during the latent phase (Jacobs *et al*., 2013). In some affected infants, persistent active mechanisms, such as chronic inflammations may prevent tissue repair, neurogenesis, and maturation, leading to tertiary brain damage (Greco *et al*., 2020; Tetorou *et al*., 2021). Several potential experimental treatments that may complement the neuroprotective effects of therapeutic hypothermia, such as xenon gas (Dingley *et al*., 2014), erythropoietin (Wu *et al*., 2022), and stem cell therapy (Kabatas *et al*., 2021; Cotten *et al*., 2023) have moved to clinical trials, but conclusive results and safety validations have not yet been achieved.

2.2.2 Neonatal HIE animal model

Several rodent models have been established in rats and mice to replicate the clinical pathogenesis of neonatal HIE (Hamdy *et al*., 2020). Of these, the Rice–Vannucci model, originally developed as an adult stroke rat model (Levine, 1960) tailored for immature rats (Rice *et al*., 1981) and mice (Sheldon *et al*., 1998; Albertsson *et al*., 2014), has been the most widely used model in neonatal HIE studies (Millar *et al*., 2017). The protocol consists of permanent ligation of the unilateral common carotid artery followed by systemic exposure to hypoxia (8% O_2, 30 min to 2 h) in immature rats originally at postnatal day 7 (P7) (Rice *et al*., 1981; Vannucci and Vannucci, 2005) (Figure 5). Age selection at the time of HI injury significantly affects the outcome severity of the injury (Odorcyk *et al*., 2020, Huang *et al*., 2017). Generally, P9–P11 rat pups are used in preclinical studies because their brain development stage is considered equivalent to that of human newborns (Semple *et al*., 2013; Patel *et al*., 2014). The neuropathological changes are typically restricted to the hemisphere ipsilateral to the ligation, mainly in the cerebral cortex, subcortical and periventricular white matter, striatum, thalamus, and hippocampus (Vannucci and Back, 2022). Thus, the contralateral hemisphere has been conventionally used as a control (Vannucci and Vannucci, 2005). Pathophysiological alterations in this model include decreased CBF (Ohshima *et al*., 2012), cerebral oxygen depletion (Bergeron *et al.*, 1999), and decreased cerebral glucose uptake (Vannucci *et al*., 2005; Odorcyk *et al*., 2020) in the early phase after HI insult. An inflammatory response has also been demonstrated (McRae *et al*., 1995). One significant drawback of this model is the high variability in the size and severity of injury among animals, making comparisons between experiments difficult (Vannucci and Hagberg, 2004, Vannucci and Vannucci, 2005). Large animal models of perinatal HIE, such as foetal sheep and newborn piglets, are also widely used because they allow for closer comparisons

of brain size, neuroanatomy, maturity, and term asphyxiated condition in neonatal patients in advanced translational contexts (Koehler *et al*., 2018).

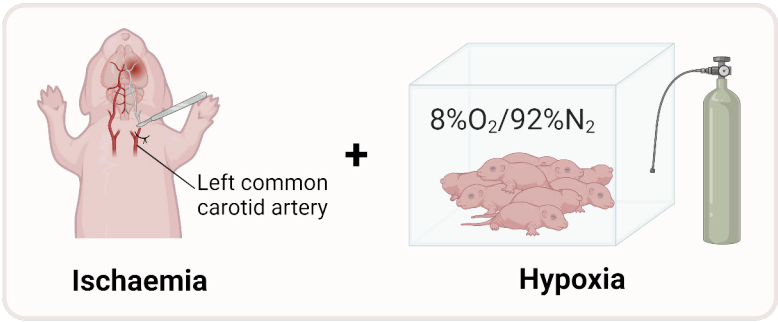

Figure 5. The Rice–Vannucci model is based on unilateral ligation of the common carotid artery combined with a 30-min to 2-h systemic hypoxic exposure (Rice *et al*., 1981; Vannucci and Vannucci, 2005). *Created using BioRender.com.*

2.3 PET imaging

2.3.1 The PET principle

PET is a nuclear medicine technique that visualises metabolic activities and biological processes inside the body with high sensitivity (Ter-Pogossian, 1992; Krishnamoorthy *et al*., 2017). PET utilises positron-emitting radionuclides attached to targeting molecules, so-called radioactive tracers or radiopharmaceuticals, that are administered to the subject and allowed to distribute inside the body (Mason and Mathis, 2003; Rong *et al*., 2023). Thus, PET can visualise and quantify specific molecular targets, such as ligands, receptors, proteins, and enzymes, that are relevant to disease onset and staging before structural changes originating from diseased tissues can be detected by other diagnostic techniques, such as computed tomography (CT) or magnetic resonance imaging (MRI). PET/CT imaging is commonly used for diagnostic or research purposes in the fields of oncological, neurological, cardiovascular, and metabolic diseases.

The principle of the PET methodology is illustrated in Figure 6. The initial step is the generation of positron-emitting radionuclides like oxygen-15 (^{15}O), carbon-11 (^{11}C) and fluorine-18 (^{18}F) via various nuclear reactions conducted by a cyclotron. In the second step, the produced radionuclides are incorporated to the molecule (precursor) of choice via a radiochemical synthesis process. Before administration of the tracer to the study subject, quality control is performed to ensure pH, endotoxin levels, purity, molar activity (if required), and solvent residues to meet Good Manufacturing Practise (GMP) compliance standards for human use. GMP-

level quality control is not usually needed in preclinical studies. The subject then receives the tracer, most usually via i.v. injection, and is placed inside the PET scanner, which records the radionuclide decay that occurs via emitted positrons in a process called annihilation.

Depending on the energy of the radionuclide, emitted positrons travel a specific distance (positron range) before encountering an electron, which triggers annihilation. The annihilation will release two high-energy (511 KeV) annihilation photons (γ-rays) travelling in opposite directions. The length that a positron can travel in tissues can range from a few millimetres to more than a centimetre, depending on the positron energy. Fluorine-18 has a low positron energy ($E_{\beta+\,max} = 0.63$ MeV), resulting in a narrower positron range and thus providing superior-resolution PET image quality. The positron energy is higher for e.g. carbon-11 ($E_{\beta+\,max} = 0.96$ MeV) and oxygen-15 (^{15}O, T½ = 2 min, $E_{\beta+\,max} = 1.73$ MeV) (Conti and Eriksson, 2016).

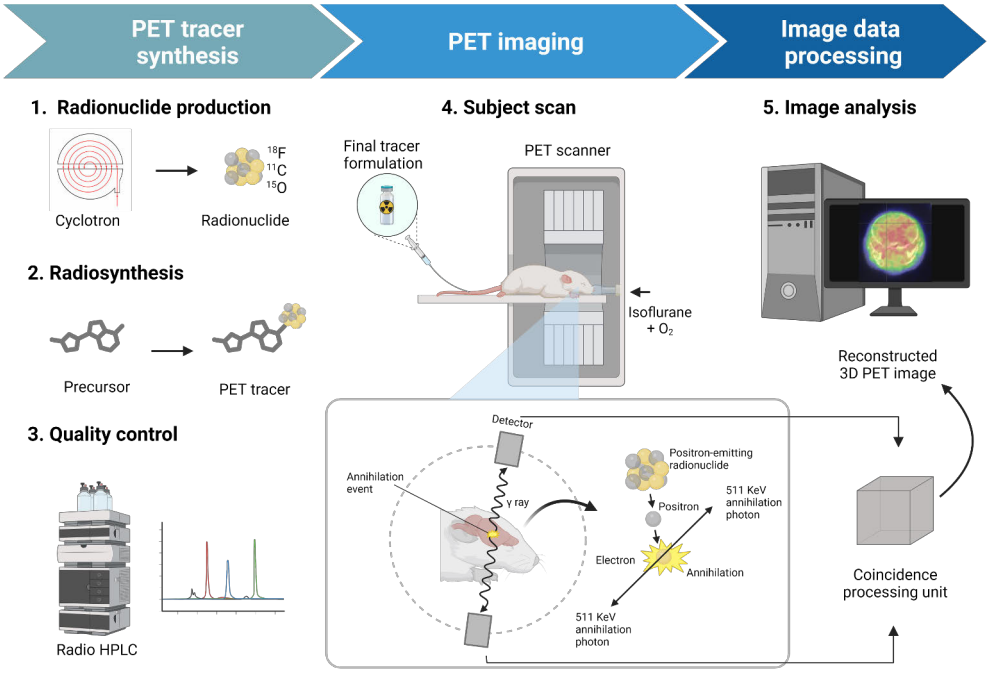

Figure 6. Principle of the PET methodology in a typical preclinical study protocol. *Modified from Rong et al. (2023) using BioRender.com.*

The ring-arrayed detectors of the PET scanner acquire the coincidence photons that occur simultaneously. After correcting for multiple factors, such as attenuation

(image correction for tissue absorption of radionuclide detection), scatter, and random coincidences, the spatial location of the annihilation can be determined. An appropriate reconstruction algorithm is required to generate 3D PET images representing the spatial tracer distribution. CT images are most often used as an anatomical reference and to correct for attenuation.

2.3.2 Small animal PET imaging

The main advantage of small animal PET imaging is that physiological events can be followed over time, either dynamically in the range allowed by the radionuclide or longitudinally in the same subject. This enables e.g. to determine the biodistribution or receptor occupancy of pharmaceuticals and study of pathophysiological changes during disease progression and interventions. Another advantage is the reduced number of animals required to obtain this information. However, this technique is also vulnerable due to certain limitations that are absent in human studies, which might affect the qualitative and quantitative outcomes, as described below:

Anaesthesia: Mice and rats should be anaesthetised for immobilisation during imaging procedures that last for minutes to hours, in which isoflurane mixed with oxygen is typically used. It is important to be aware that the use of isoflurane may affect the tracer's distribution and binding potential (Hildebrandt *et al*., 2008; Miranda *et al*., 2021).

Physiological homeostasis: Owing to the small size of rodents, it is more difficult to ensure steady body physiological/biological conditions during each scan period, although unchanged physiological/biological conditions are a prerequisite in PET experiments in most cases to extract biologically meaningful information from PET images. Continuous monitoring of vital signs, such as body temperature, heartbeat, and respiratory rate, is important to ensure physiological homeostasis between animals on different study days in longitudinal studies so that a non-negligible impact on the image quality outcome may be minimised.

Injected volume: Another constraint is the limited amount and activity of radiotracers administered to mice and rats. The injection volume is limited to less than 10% of the animal's total blood volume. See also 'Detection sensitivity' below.

Spatial resolution: As mice and rats are most commonly used as preclinical models, higher spatial resolution is required to detect specific tracer accumulation in the small structures of target organs of small animals. The typical spatial resolution of

clinical PET systems is approximately 4–6 mm, whereas state-of-the-art small animal PET scanners have a spatial resolution of less than 1 mm, which does not yet provide a comparative visualisation of structural detail in rodents.

Detection sensitivity: The system detection sensitivity of a PET device is the percentage between the emitted and measured annihilation photons and provides information about the ability of the PET system to detect coincidence events resulting from annihilation. High sensitivity is required when e.g. studying receptors expressed at low densities, tracers with low molar activity, or radioactivity concentrations within a restricted injectable amount. Extended axial field-of-view (FOV) PET has become a recent trend to allow for more extended coincidence assessment at each local region, thereby enabling further increased sensitivity and the ability to assess arterial input function (AIF) at the same time as assessing brain function. This will be an important feature in translational research towards clinical research using a recently developed total-body PET scanner.

Counting rate performance: An increase in the administration dose is typically an option to compensate for a PET device's limited sensitivity. However, this approach becomes limited because of the considerably increased number of radio detectors with more sophisticated electronic circuits, resulting in imperfect corrections for accidentally detected coincidence events, dead-time estimates, and scatter distribution calculations. At this time, fairly well-validated scan protocols are required to avoid possible degradation of the reconstructed PET images.

2.4 Neuroinflammation

Neuroinflammation is an inflammatory response that occurs in the brain and spinal cord and is elicited by a variety of neuropathic factors, including infection, injury, toxins, autoimmunity, and ischaemia (Ransohoff, 2016). Microglia are the primary resident immune cells, and like peripheral macrophages, they actively patrol the entire CNS even in non-pathological situations. Microglia regulate CNS homeostasis via phagocytic activity by clearing pathogens, damaged cells, and debris. During postnatal development, the homeostatic functions of microglia include trophic support of developing neurones, synaptic formation aid, and phagocytosis of apoptotic neurones (Kierdorf and Prinz, 2017). In response to altered homeostasis, microglia lose their ramifications and transform into reactive microglia with marked proliferation, so-called microgliosis, which protects neurones from invading pathogens by producing inflammatory mediators such as cytokines and chemokines. However, many studies have linked excessive inflammation mediated by CNS glial cells, particularly microglia, to the exacerbation of chronic neurodegenerative

diseases. A better understanding of microglia-mediated inflammation at different neurodegenerative disease stages may pave the way for novel treatment interventions that modulate inflammatory activity.

2.4.1 TSPO as a biomarker of neuroinflammation

In this context, microgliosis is a useful imaging target for examining the evolution and progression of various CNS diseases. TSPO, originally called peripheral benzodiazepine receptor (PBR), is a protein with five transmembrane helical domains situated on the outer mitochondrial membrane of cells in most peripheral organs. TSPO has been implicated in many cellular processes, including steroidogenesis, inflammatory responses, oxidative stress, mitochondrial homeostasis and energy production, apoptosis, and cell proliferation, but its regulatory effects are not completely understood (Bonsack and Sukumari-Ramesh, 2018). The function of TSPO may vary between cells depending on their specialised roles in different tissues. Although TSPO expression in the CNS is very low, it is markedly elevated in reactive microglia, astrocytes, macrophages, and endothelial cells in response to CNS injury (Largeau *et al*., 2017). PET imaging using TSPO-targeting tracers has proven to be a powerful molecular imaging tool for longitudinally detecting neuroinflammation *in vivo* in a variety of neurological, neurodegenerative, and psychiatric diseases (Van Camp *et al*., 2021).

2.4.2 TSPO PET tracers

The most commonly used TSPO-specific ligand is [^{11}C]PK11195, which was developed in the 1980s as a first-generation TSPO ligand (Le Fur *et al*., 1983). Although both clinical and preclinical [^{11}C]PK11195 PET studies are still routinely conducted on various brain diseases, several shortcomings of this tracer, including a poor signal-to-noise ratio due to low affinity to TSPO and high lipophilicity, and poor blood–brain barrier (BBB) penetration (Chauveau *et al*., 2008), have encouraged the development of second-generation TSPO tracers, such as [^{11}C]PBR28 (Kreisl *et al*., 2010) and [^{18}F]DPA-714 (Arlicot *et al*., 2012), and third-generation tracers, including [^{18}F]GE180 (Fan *et al*., 2016). Keller *et al.* (2017) recently developed a TSPO tracer, [^{18}F]F-DPA, which has a lower metabolic rate than [^{18}F]DPA-714, at least in rodents, and superior TSPO binding affinity (Ki = 1.7 nM) compared with [^{18}F]DPA-714 (Ki = 7.0 nM) and [^{11}C]PK11195 (Ki = 3.6 nM).

[^{11}C]PK11195 was previously reported to quantitatively detect spinal gliosis in a PSNL rat model of NPP (Imamoto *et al.,* 2013). Another study using an experimental cerebral ischaemia rat model demonstrated that [^{18}F]DPA-714 displayed a higher signal-to-noise ratio than [^{11}C]PK11195 (Boutin *et al.,* 2013).

[^{18}F]DPA-714 was also reported to provide accurate quantitative information on TSPO expression in a rat model of focal cerebral ischaemia (Martin *et al.,* 2010). In contrast, [^{18}F]GE180 PET did not detect acute-phase inflammatory responses (< 32 h post-injury) in a piglet model of HIE (de Lange *et al.,* 2018)

The superiority of [^{18}F]F-DPA over [^{18}F]DPA-714 and [^{11}C]PBR28 has been demonstrated in an Alzheimer's disease mouse model, showing higher transgenic-to-wild-type brain SUV ratios and faster clearance for [^{18}F]F-DPA compared with the other two tracers (Keller *et al.,* 2018; López-Picón *et al.,* 2022). These findings support the utility of [^{18}F]F-DPA for detecting low-grade neuroinflammation with shorter dynamic scans. [^{18}F]F-DPA was also used to detect changes in TSPO expression in lesions following olfactory ensheathing cell transplantation in a spinal cord injury (SCI) rat model (Zhang *et al.,* 2021).

2.5 Cerebral oxygen metabolism

2.5.1 PET with [^{15}O]-labelled gases

PET with ^{15}O-labelled gases has been the gold standard tool for decades to provide *in vivo* measures of oxygen metabolism, the main energy substrate of the brain, in addition to glucose. With ^{15}O-labelled tracers, quantitative measurements of cerebral haemodynamics (CBF and cerebral blood volume [CBV]) and oxygen metabolism (cerebral metabolic rate of oxygen [$CMRO_2$]) can be achieved using a protocol involving three sets of PET scans with the inhalation of three gaseous tracers of [^{15}O]CO, [^{15}O]CO_2, and [^{15}O]O_2. The fluctuations in these parameters are closely related to the severity and reversibility of cerebral ischaemia in, e.g. stroke patients; the technique is therefore applied for definitive diagnosis and treatment response monitoring. Despite the proven clinical value of PET with ^{15}O-labelled tracers, the requirement of an in-house cyclotron to produce ultra-short half-life (T½ = 2 min) ^{15}O-labelled tracers and logistical complexity in managing all operations hamper its broad application. Its kinetic modelling approach has also been challenging due to immature software programmes, in particular for estimating the metabolised [^{15}O]H_2O generated in the patient's body after the inhalation of [^{15}O]O_2. For the preclinical application of this technique, the administration of ^{15}O-labelled gases to small animals has required exceptionally invasive and laborious procedures, such as tracheotomy, repeated arterial blood sampling (Temma *et al*., 2008; Watabe *et al*., 2013), or the use of injectable [^{15}O]O_2-labelled haemoglobin (Temma *et al.,* 2010). Recently, Temma *et al.* (2017) succeeded in administering ^{15}O-labelled tracers to mice via spontaneous inhalation. This technique provided quantitative values of CBF and $CMRO_2$ and their time-dependent changes over a 1-month disease course of a bilateral common carotid artery stenosis mouse model, which replicates patients with

chronic cerebral hypoperfusion. However, there remains a need to develop a comprehensive system that significantly reduces the labour-intensive task of controlling the production and inhalation of three sets of gaseous radioactive tracers with fully automated quality control.

2.5.2 Calculation of oxygen metabolism from PET images

$[^{15}O]O_2$ inhalation PET provides quantitative $CMRO_2$ based on an estimation of the influx rate of $[^{15}O]O_2$ to the cerebral tissue from arterial blood, where arterial input function (AIF) must be preconditionally determined (Kudomi *et al*., 2009). Of note, the metabolic product of $[^{15}O]O_2$ in arterial blood, as a form of recirculation $[^{15}O]H_2O$, needs to be accurately determined before the computation of parametric images of $CMRO_2$. The arterial whole-blood radioactivity curve is obtained by measuring the radioactivity concentration of continuously withdrawn whole blood using a well counter device. Assessment of a time-dependent metabolised $[^{15}O]H_2O$ curve is achieved by separating plasma from whole-blood samples. However, this is a very labour-intensive procedure and imposes a significant burden on patients and particularly small animals. Iida *et al.* (1993) developed a mathematical formula to predict the production rate of metabolised $[^{15}O]H_2O$ ($\boldsymbol{k_w}$) based on a physiological model, eliminating multiple blood samplings. Moreover, Kudomi *et al.* (2009) demonstrated the adequacy of this physiological model technique for the reliable estimation of $CMRO_2$ in a wide range of species, including humans, monkeys, pigs, and rats, further observing greater $\boldsymbol{k_w}$ values in smaller animals. Although age- or body-size-dependent changes in the $\boldsymbol{k_w}$ values in growing infant rats remain unclear, this approach is considered to resolve the most critical bottleneck in ^{15}O-labelled gas PET.

2.6 Cerebral hypoxia

Cerebral hypoxia is a neurological condition caused by decreased oxygen supply to the brain. Hypoxic brain injury can stem from e.g. interruption of blood flow to the brain or systemic disorders that affect the oxygen content of the blood (Arora and Tantia, 2019). Brain cells are very sensitive to oxygen deprivation and can die within a few minutes after the oxygen supply is cut off. Long-term hypoxia can cause coma, seizures, and even brain death. Cardiac arrest is the most common cause of hypoxic brain injury; others include traumatic vascular injuries, near-drowning, carbon monoxide poisoning, and acute lung injury.

2.6.1 PET tracers targeting hypoxic tissues

Nitroimidazoles are hypoxia-selective compounds that have been adapted as imaging biomarkers to depict hypoxic, but viable, tissue in animals and humans (Chapman, 1979, Chapman *et al.*, 1981). Nitroimidazoles enter cells via diffusion, where they undergo a series of enzymatic reductions and eventually irreversibly bind to cellular macromolecules such as proteins and DNA (Nguyen and Kim, 2023). Under normal oxygen conditions, the presence of oxygen prevents the enzymatic reduction of nitroimidazoles, and hence no binding occurs. Several nitroimidazole-based radiotracers, such as [^{18}F]FMISO, [^{18}F]EF5, and [^{64}Cu]ATSM, have been developed (Nguyen and Kim, 2023). In general, they show slow pharmacokinetic properties, and imaging is usually performed 3–4 h post-injection (p.i.) (Williamson *et al.,* 2013). They are mostly used for imaging of tumour hypoxia in the context of overcoming hypoxia-dependent treatment resistance (Perez *et al.*, 2023). These tracers have also been marginally used to study cerebral ischaemia, particularly after ischaemic stroke (Takasawa *et al.,* 2008; Williamson *et al.,* 2013; Baskin *et al.,* 2015; Little *et al.,* 2021). A transient increase in [^{18}F]FMISO uptake was observed in a rat stroke model in the early phase after cerebral artery occlusion, but not after early reperfusion or in areas where tissue necrosis had developed (Takasawa *et al.,* 2007), whereas another study reported that [^{18}F]FMISO may provide efficient diagnostic imaging beyond the hyperacute phase (Little *et al.,* 2021).

2.7 Cerebral glucose metabolism

Although the brain accounts for only 2% of total body weight, its glucose consumption, the main source of energy in the brain, accounts for 25% of total body glucose consumption (Dienel, 2019). The infant brain undergoes a rapid increase in glucose consumption during the maturation process (Odorcyk *et al*., 2020), leading to unique resilience or vulnerability characteristics of the immature brain to injury. Therefore, monitoring cerebral glucose metabolism might provide functional information about the severity of cerebral damage, its recovery process, and potential neurological prognosis in HIE.

2.7.1 PET tracer targeting glucose metabolism

2-deoxy-2-[^{18}F]fluoro-D-glucose ([^{18}F]FDG) is an analogue of glucose and is similar to glucose in several respects. It is most commonly used as a PET tracer to identify *in vivo* local glucose utilisation in various clinical settings and is routinely used in oncology diagnosis and functional brain metabolic imaging. After i.v. administration, [^{18}F]FDG is transported from the blood to the brain via a carrier-mediated diffusion mechanism like glucose. Hexokinase catalyses the phosphorylation of glucose to

glucose-6-PO3 and [^{18}F]FDG to [^{18}F]FDG-6-PO4. [^{18}F]FDG is a competitive substrate of glucose in both transport via glucose transporter (GLUT) proteins and phosphorylation steps. However, [^{18}F]FDG-6-PO4 is not a significant substrate for further metabolism. It is not significantly converted into glycogen and is not further metabolised in the glycolytic pathways. [^{18}F]FDG-6-PO4 also does not diffuse across cell membranes; thus, it is metabolically trapped intracellularly, and it can be captured locally by PET. Of importance is that the rate of being converted to [^{18}F]FDG-6-PO4 in the interstitial space from [^{18}F]FDG in the blood as computed by means of a compartment model was shown to represent the production rate of ATP that is utilised to restore and maintain the Na^+ and K^+ gradients across the neuronal membrane by the Na^+-K^+ pump following the generation of action potentials under normal physiological conditions in the brain (Mata *et al*., 1980).

[^{18}F]FDG uptake has been thus proven to characterise cerebral metabolic activity and to detect decreased metabolism attributed to impaired cognitive function. It is also known that [^{18}F]FDG accumulation is reduced in regions of ischaemia and necrosis. Furthermore, many studies demonstrated that inflammation with activation of resident microglia and recruitment of monocytes/macrophages induced by focal cerebral ischaemia or haemorrhage causes increased uptake of [^{18}F]FDG (Ayubcha *et al*., 2023; Schroeter *et al*., 2009; Xiang *et al*., 2021). Expression of reactive microglia is triggered spontaneously due to damage-associated molecular patterns (DAMPs) when cerebral vascular events cause significant damage to cerebral tissue (Kono and Rock, 2008; Huang *et al*., 2015).

2.7.2 PET imaging of cerebral [^{18}F]FDG in HIE

Despite the scarcity of neonatal PET studies, a few experimental and clinical studies have indicated the prognostic value of [^{18}F]FDG PET early after HI insult, which impacts neurological impairment. Clinical [^{18}F]FDG PET studies of asphyxiated newborn infants demonstrated both decreased (Thorngren-Jerneck *et al*., 2001; Shi *et al*., 2012) and increased brain [^{18}F]FDG uptake (Chugani, 2021) post-insult and correlation with brain damage severity. The exact reason for these contradictory findings is unclear but may be due to inconsistent variables such as time point post-affection, severity of damage, and analytical methods. [^{18}F]FDG PET with experimental animal models mimicking neonatal patients with HIE also demonstrated various patterns of decreased [^{18}F]FDG uptake in the Rice–Vannucci rat (Odorcyk *et al*., 2020), piglets after global hypoxia (de Lange *et al*., 2012), and newborn lambs after foetal asphyxia (Thorngren-Jerneck *et al*., 2001). Odorcyk *et al.* (2020), on the other hand, observed a linear increase in the brain [^{18}F]FDG SUV during early neurodevelopment. Thus, systematic identification of time-dependently deranged [^{18}F]FDG accumulation in brain tissue *in vivo*, especially in the hyperacute phase after HI, would be of tremendous value.

3 Aims

The overall aim of this thesis was to evaluate novel PET imaging approaches for assessing neurodegenerative disease progression. Two experimental animal models representing neurodegenerative disorders were utilised: the NPP and neonatal HIE models. PET tracers targeting CNS inflammation, oxygen metabolism, hypoxia, and glucose uptake were utilised to clarify their efficacy as biomarkers for accurate diagnosis and progress monitoring, as well as their prognostic value, which could provide relevant advances towards the development of personalised therapies.

The specific objectives for each study were as follows:

I. To evaluate the efficacy of [^{18}F]F-DPA PET for visualising neuroinflammation in the spinal cord of a rat model of NPP.

   Hypothesis: [^{18}F]F-DPA PET can reliably identify NPP that correlates with the magnitude of glial activation at the spinal cord level caused by peripheral nerve injury.

II. To assess the value of ^{15}O-labelled gas PET setup for understanding disease progression in a rat model of neonatal HIE by quantitative assessment of CBF and $CMRO_2$.

   Hypothesis: This newly developed PET methodology can non-invasively depict temporal changes in cerebral oxygen metabolism in parallel with brain maturation after HI insult in rat neonates.

III. To explore the usefulness of PET tracers targeting neuroinflammation, hypoxia, and glucose metabolism for robust diagnosis and early outcome prediction in a rat model of HIE.

   Hypothesis: PET can detect different pathophysiological changes after brain injury and may have prognostic value for HI injury outcomes.

4 Materials and Methods

4.1 Experimental design (I–III)

Microglial activation in the spinal cord originating from peripheral nerve damage was examined using a recently developed TSPO-targeting PET tracer, [^{18}F]F-DPA, in a PSNL rat model (**I**, Figure 7). To estimate the magnitude of pain caused by nerve ligation, von Frey filament tests were conducted before surgery and on days 3 and 7 post-insult. The uptake of [^{18}F]F-DPA in the ipsilateral region of the lumbar spinal cord was determined at day 7 after surgery by *in vivo* PET imaging followed by *ex vivo* gamma counting (γ-counting), autoradiography (ARG), and immunohistochemistry (IHC) staining against biomarkers targeting ionized calcium-binding adapter molecule 1 (Iba1) (activated microglia) and glial fibrillary acidic protein (GFAP) (astrocytes). *Ex vivo* PET imaging of the removed spinal cord and brain was also performed. Finally, the performance of [^{18}F]F-DPA was compared with that of [^{11}C]PK11195, a commonly used TSPO tracer in clinical settings. Sham-operated animals were used as controls.

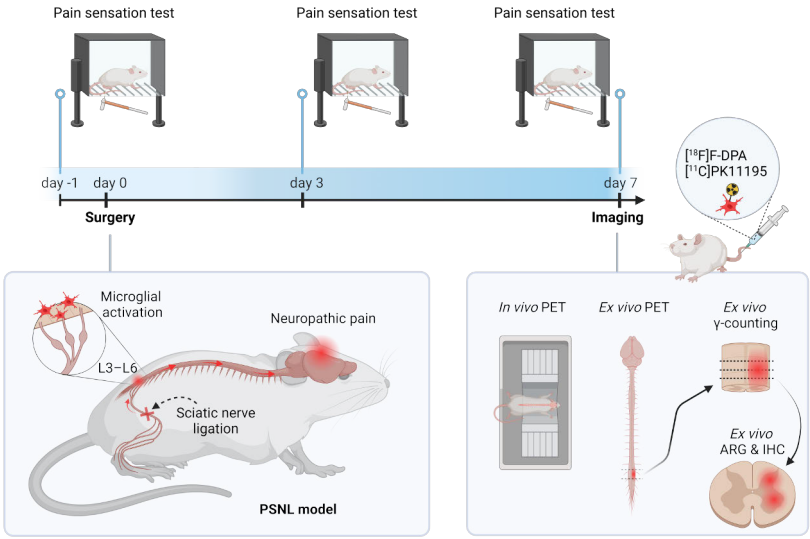

Figure 7. Experimental design for study I. *Created using BioRender.com.*

Study **II** utilised a new methodology under development to monitor changes in brain oxygen metabolism after HI insult in rat neonates. The 1st part of the study measured the production rate of metabolised [^{15}O]H_2O (k_w) in two age groups (Figure 8). In the 2nd part of the study, the integrated oxygen 15-labelled gas inhalation methodology allowed repetitive and fully quantitative assessment of CBF and $CMRO_2$ in the neonatal HIE rat model (Figure 9). Age-matched healthy or sham-operated animals served as controls. After the last PET scan on day 14, brain sections were histologically examined by haematoxylin and eosin (H&E) staining (morphology) and IHC staining against Iba1 to determine the correlation between changes in CBF and $CMRO_2$ and histopathological damage.

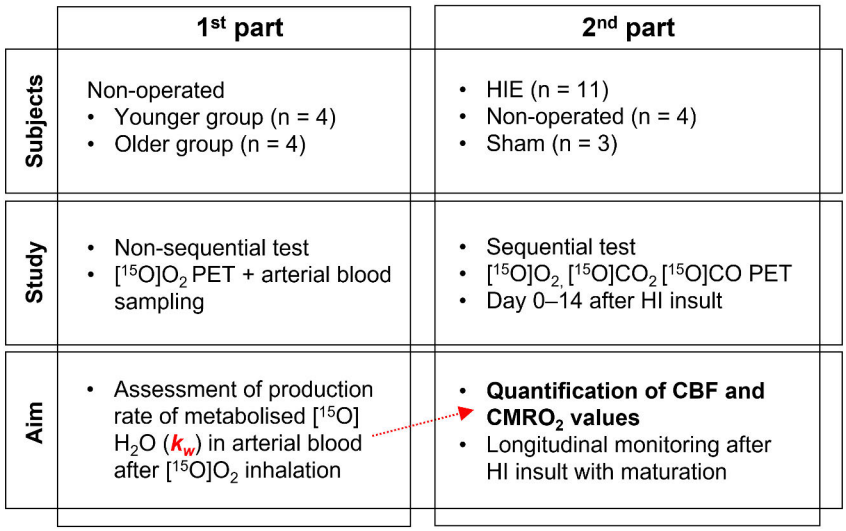

Figure 8. Study composition for study II. The 1st part of the study measured the production rate of metabolised [^{15}O]H_2O (k_w) in two age groups of non-operated rats. The red arrow indicates that the k_w value determined in the 1st part was applied to quantitate the $CMRO_2$ in the 2nd part without blood sampling.

Study **III** aimed to determine the interplay between the appearance of hypoxia ([^{18}F]EF5), glucose uptake ([^{18}F]FDG), and inflammation ([^{18}F]F-DPA) at different phases after HI insult in rat neonates (Figure 9). *In vivo* PET/CT imaging was performed with neonatal HIE or sham-operated animals on days 0, 1, 4, 7, and 21 after surgery, followed by *ex vivo* ARG and IHC against Iba1, GFAP, microtubule-associated protein 2 (MAP2), and neuronal nuclei (NeuN). The prognostic value of [^{18}F]FDG uptake 1 day after surgery was also compared with the level of brain damage detected 3 weeks later.

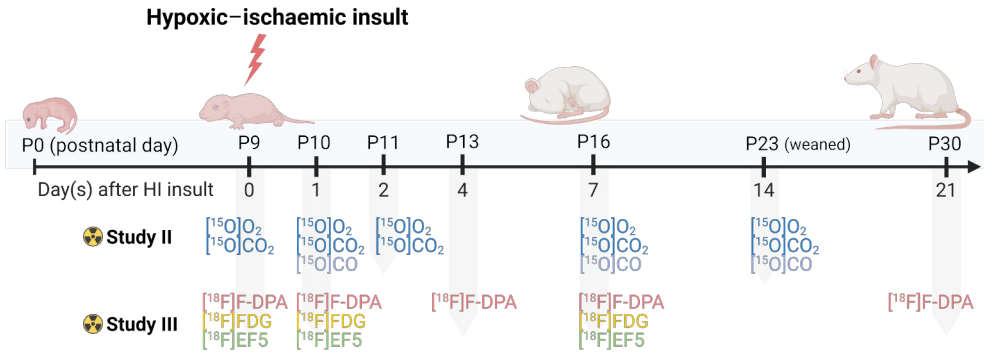

Figure 9. Schedule of PET scans with each tracer after HI insult in 9-day-old rat pups for studies II and III. *Created using BioRender.com*.

4.2 Animal models (I–III)

All animals were group housed under standard conditions (12-h light/dark cycle, temperature 21 ± 3°C, humidity 55 ± 15%) at the Central Animal Laboratory, University of Turku, with free access to tap water and food. Environmental enrichment was provided by chew blocks and cardboard tubes. Five-week-old male Sprague–Dawley rats were used in study **I**. In studies **II** and **III**, P9–P10 Sprague–Dawley rat pups were used and were kept with their dams until weaning. Sprague–Dawley rats aged 3 and 5 weeks were also used in the 1st part of study **III**. Both male and female rats were included in studies **II** and **III**. The animal models used in each study are summarised in Table 1.

All procedures and protocols were approved by the National Project Authorization Board of Finland, adhering to the 3R principles of replacement, reduction, and refinement, following Finnish National legislation (Act 497/2013, Decree 564/2013) and EU Directive 2010/EU/63 on the protection of animals used for scientific purposes. The project numbers were ESAVI/20863/2018 (**I, II**) and ESAVI/9611/2020 (**III**). All reported experiments complied with Animal Research: Reporting of *In Vivo* Experiments (ARRIVE) guidelines.

4.2.1 NPP model (I)

Chronic NPP was induced by PSNL under isoflurane anaesthesia (4% isoflurane for induction, 1.5–2% for maintenance) (Seltzer *et al*., 1990). Briefly, approximately one-third to one-half of the diameter of the right sciatic nerve (ipsilateral) was tightly ligated at the upper-thigh level, causing unilateral inflammation of the lumbar spinal cord at the L3–L6 level. Sham animals underwent a similar surgical procedure without the sciatic nerve ligation. Animals were housed separately for 2 days after

surgery to avoid biting the wounds of each other. For pain management, buprenorphine (0.3 mg/ml) was administered subcutaneously before surgery and twice daily for two consecutive days after injury.

Table 1. Animal models and experimental information for studies I–III.

Study	Animal model	Age*	Gender	PET tracer	Scanner	Target
I	PSNL	5 w/o	M	[^{18}F]F-DPA	β-cube Inveon	Spinal cord
		5 w/o	M	[^{11}C]PK11195	β-cube	Spinal cord
	Sham	5 w/o	M	[^{18}F]F-DPA	β-cube	Spinal cord
II						
1st part	Non-operated	3 w/o	M/F	[^{15}O]O_2	HRRT	Brain
		5 w/o	M/F	[^{15}O]O_2	HRRT	Brain
2nd part	HIE	9 d/o	M/F	[^{15}O]-gases	β-cube	Brain
	Non-operated	9 d/o	M/F	[^{15}O]-gases	β-cube	Brain
	Sham	9 d/o	M/F	[^{15}O]-gases	β-cube	Brain
III	HIE	9–10 d/o	M/F	[^{18}F]F-DPA	β-cube	Brain
		9–10 d/o	M/F	[^{18}F]FDG	β-cube	Brain
		9–10 d/o	M/F	[^{18}F]EF5	β-cube	Brain
	Sham	9–10 d/o	M/F	[^{18}F]F-DPA	β-cube	Brain
		9–10 d/o	M/F	[^{18}F]FDG	β-cube	Brain
		9–10 d/o	M/F	[^{18}F]EF5	β-cube	Brain

*Age at the time of the surgical intervention. **Abbreviations:** w/o = weeks old; d/o = days old; M = male; F = female.

4.2.2 Neonatal HIE model (II, III)

Neonatal HIE was induced using a widely recognised murine model in which brain injury results from a combination of unilateral ligation of the common carotid artery and systemic hypoxia (Rice *et al*., 1981; Vannucci and Vannucci, 2005). Rat pups underwent ligation of the left common carotid artery under isoflurane anaesthesia (4% for induction, 1.5–2% for maintenance) at P9 or P10 (the age equivalent to the brain development of a term infant at birth). Subcutaneous buprenorphine (0.3 mg/ml) was administered as analgesia once before surgery. The ligation was performed via neck incision, after which the common carotid artery was permanently severed. The pups were then returned to their dam for 1 h, after which they were exposed to systemic hypoxia for 2 h (8% O_2 and 92% N_2, P360 ProOx, BioSpherix) at a constant temperature (32°C) to cause unilateral HI brain injury. Sham controls underwent surgery without arterial ligation. Instead of hypoxic exposure, sham

animals were kept in a warm environment breathing normal room air isolated from their dam for 2 h. Non-operated pups experienced no interventions.

4.3 Pain sensation test (I)

Tactile-evoked mechanical allodynia following the induction of unilateral peripheral nerve neuropathy was detected using the von Frey filament test, which can examine changes in paw withdrawal threshold values using the up-down method (Rice *et al.*, 1981). Rats were placed on a mesh floor covered with an inverted transparent plastic box until exploratory behaviour ceased. Nine individual von Frey filaments with forces of 0.4, 0.6, 1.0, 1.4, 2.0, 4.0, 6.0, 8.0, and 10.0 g (Ugo Basile) were applied to the central region of the hindpaw plantar surface. The weakest stimulation causing the withdrawal response was set as the threshold value.

4.4 Radionuclide and PET tracer production (I–III)

Radionuclides were produced at the Accelerator Laboratory (Turku PET Centre, Åbo Akademi University). In studies **I** and **III**, ^{11}C via ^{14}N(p,α) and ^{18}F via ^{18}O(p,n) radionuclides were produced using a CC-18/9 cyclotron (Efremov Scientific Institute of Electrophysical Apparatus, St. Petersburg, Russia). In study **II**, ^{15}O via ^{14}N(d,n) was produced using a Cyclotron 3D (C3D, IBA solutions, Louvain, Belgium).

PET tracers were synthesised at the Radiopharmaceutical Chemistry Laboratory (Turku PET Centre, University of Turku). [^{18}F]F-DPA ((N,N-diethyl-2-(2-(4-([^{18}F]fluoro)phenyl)-5,7-dimethylpyrazolo[1,5-a]pyrimidin-3-yl)acetamide)) (Keller *et al.,* 2017), [^{11}C]PK11195 (Rissanen *et al.,* 2014), and [^{18}F]EF5 (2-(2-nitro-1H-imidazol-1-yl)-N-(2,2,3,3,3-[^{18}F]pentafluoropropyl)-acetamide) (Eskola *et al.,* 2012) were synthesised as previously published. [^{18}F]FDG was synthesised using the FASTlab synthesiser (GE Healthcare) as previously described (Takkinen *et al.*, 2017). The radiochemical purity exceeded 99% for [^{18}F]F-DPA, [^{11}C]PK11195, and [^{18}F]EF5, and 98% for [^{18}F]FDG. The injected doses, molar activities (A_m), and injected masses at the time of injection (only for [^{18}F]F-DPA) are summarised for PET studies in Table 2 and ARG in Table 3. For study **III**, the decay-corrected A_m at the end of synthesis exceeded 3.7 GBq/μmol for [^{18}F]EF5, and 100 GBq/μmol for [^{18}F]FDG.

Table 2. Animal groups, experimental set-up, and radiotracer information for PET imaging in studies I and III. Of note is that the dose limit for the β-cube scanner is 10 MBq, enabling injections of max. 5 MBq / animal when scanning two animals simultaneously (study III). The dose limit for Inveon is approx. 50 MBq. The range of injected doses varies due to both animal weight and used scanner. The A_m is the ratio between radioactivity and mass of the compound and play a role for radiotracers targeting saturable binding sites (e.g. receptors) but is not important for radiotracers of which endogenous levels are present in excess of the radiotracer itself (e.g. glucose).

Study	Tracer	Animal model	n	Animal weight (g)	Injected dose (MBq)	A_M Injected (GBq/μmol)	Injected mass (μg/kg)
I							
In vivo PET	[^{18}F]F-DPA (β-cube)	PSNL (7 d)	3	145 ± 10	8.9 ± 1.3	2.2 ± 1.1	11.2 ± 4.1
	[^{18}F]F-DPA (Inveon)	PSNL (7 d)	3	166 ± 3	49.6 ± 2.0	3.6 ± 0.9	31.2 ± 8.7
	[^{11}C]PK11195 (β-cube)	PSNL (7 d)	3	155 ± 1	10.6 ± 0.7	43.4 ± 11.6	0.59 ± 0.17
Ex vivo PET	[^{18}F]F-DPA	PSNL (7 d)	2	158, 149	48.5, 51.4	5.4, 3.1	29.7, 13.3
	[^{18}F]F-DPA	Sham (7 d)	2	219, 219	48.0, 50.8	1.0, 1.0	75.8, 82.2
III							
In vivo PET	[^{18}F]F-DPA	HIE (0 d)	2	19.3 ± 0.14	4.54 ± 0.12	0.77, 0.77	108.1 ± 2.0
		HIE (1 d)	14	25.5 ± 4.8	4.93 ± 0.22	0.76 ± 0.15	98.6 ± 36.8
		HIE (4 d)	11	32.2 ± 3.6	4.85± 0.26	0.73 ± 0.16	76.3 ± 18.7
		HIE (7 d)	11	40.5 ± 3.6	4.38 ± 0.39	0.78 ± 0.17	55.3 ± 12.4
		HIE (21 d)	5	98.0 ± 5.7	5.28 ± 0.24	0.88 ± 0.19	22.4 ± 4.5
		Sham (0 d)	5	19.7 ± 1.6	4.05 ± 1.21	1.09 ± 0.12	66.7 ± 20.0
	[^{18}F]EF5	HIE (0 d)	12	22.6 ± 1.4	3.96 ± 1.11	N/A	N/A
		HIE (1 d)	2	29.0 ± 2.1	4.53 ± 0.14	N/A	N/A
		HIE (7 d)	5	40.3 ± 1.4	3.35 ± 0.67	N/A	N/A
		Sham (0 d)	5	23.5 ± 2.7	3.48 ± 1.45	N/A	N/A
	[^{18}F]FDG	HIE (0 d)	12	25.2 ± 3.3	2.97 ± 0.16	N/A	N/A
		HIE (1 d)	15	24.7 ± 4.8	2.95 ± 0.23	N/A	N/A
		HIE (7 d)	5	39.2 ± 9.2	2.86 ± 0.05	N/A	N/A
		Sham (0 d)	5	22.7 ± 4.4	3.01 ± 0.06	N/A	N/A

Abbreviations: d = day(s) after surgical intervention; n = number of animals; N/A = not applicable

Table 3. Animal groups, experimental set-up, and radiotracer information for *ex vivo* ARG experiments in studies I and III. Of note is that in study III, some animals were scanned prior ARG experiments and hence limited to the maximum dose of 5 MBq/animal in the β-cube scanner (see Table 2). The range of injected doses varies due to both animal weight and used scanner.

Study	Tracer	Animal model	n	Animal weight (g)	Injected dose (MBq)	A_m Injected (GBq/μmol)	Injected mass (μg/kg)
I							
Ex vivo ARG	[^{18}F]F-DPA	PSNL (7 d)	6	161 ± 8	49.7 ± 1.8	3.8 ± 1.1	30.6 ± 9.1
	[^{18}F]F-DPA	Sham (7 d)	2	219, 219	48.0, 50.8	1.0, 1.0	75.8, 82.2
	[^{18}F]F-DPA (PK pretreated 1 mg)	PSNL (7 d)	1	179	36.8	1.1	66.5
	[^{18}F]F-DPA (PK pretreated 3 mg)	PSNL (7 d)	1	220	48.0	0.61	125.9
	[^{11}C]PK11195	PSNL (7 d)	3	148 ± 18	52.1 ± 1.7	35.3 ± 15.9	4.01 ± 1.6
III							
Ex vivo ARG	[^{18}F]F-DPA	HIE (0 d)	4	23.3 ± 4.6	4.64 ± 0.16	0.75 ± 0.03	96.4 ± 13.6
		HIE (1 d)	3	20.0 ± 3.7	5.06 ± 0.06	0.72 ± 0.16	134.4 ± 45.5
		HIE (4 d)	5	36.9 ± 3.3	4.96 ± 0.12	0.85 ± 0.07	55.9 ± 2.3
		HIE (7 d)	5	42.2 ± 2.7	4.60 ± 0.41	0.81 ± 0.16	48.8 ± 8.6
		HIE (21 d)	6	103 ± 14	5.00 ± 0.13	0.93 ± 0.10	19.0 ± 3.2
		Sham (0 d)	5	19.7 ± 1.6	4.05 ± 1.21	1.09 ± 0.12	66.7 ± 20.0
	[^{18}F]EF5	HIE (0 d)	8	21.8 ± 1.8	3.20 ± 1.05	N/A	N/A
		HIE (1 d)	2	29.0 ± 2.1	4.50 ± 0.14	N/A	N/A
		HIE (7 d)	4	33.8 ± 2.8	4.35 ± 0.23	N/A	N/A
		Sham (0 d)	8	24.8 ± 2.7	3.90 ± 1.27	N/A	N/A
	[^{18}F]FDG	HIE (0 d)	6	25.9 ± 3.0	3.64 ± 1.05	N/A	N/A
		HIE (1 d)	7	22.5 ± 5.5	4.04 ± 1.21	N/A	N/A
		HIE (7 d)	4	40.4 ± 10.1	2.86 ± 0.06	N/A	N/A
		Sham (0 d)	8	19.8 ± 1.3	4.00 ± 1.00	N/A	N/A
	[^{18}F]F-DPA (PK pretreated 1 mg)	HIE (7 d)	1	48.4	4.83	0.73	N/A

Abbreviations: d = day(s) after surgical intervention; n = number of animals; N/A = not applicable

[^{15}O]O_2, [^{15}O]CO_2, and [^{15}O]CO gases were produced in the target and purified as described in **II**. The radiochemical and chemical purity was assessed by gas chromatography before inhalation. The gases were mixed with pure oxygen and air at a ratio leading to animals inhaling 20% oxygen during the scan period. The typical flow rate of radioactive gas was 300 ml/min, corresponding to 250, 150, and 300 MBq/min for ^{15}O-O_2, ^{15}O-CO_2, and ^{15}O-CO, respectively. Inhalation gases were mixed with evaporated isoflurane gas at a concentration of 2–2.5% before transfer to the animal holder.

4.5 PET/CT imaging (I–III)

PET/CT scans were performed on day 7 after the PSNL injury (study **I**) using either X- and β-Cubes (Molecubes) or Inveon (Siemens) scanners. Following NEMA guidelines, a detailed comparison of the two PET scanner designs and performances was previously reported (Teuho *et al*., 2020). X- and β-Cubes were used to scan rat pups (**II**, **III**). In addition, the 1st part of study **II** utilised a dedicated HRRT PET scanner (CTI PET Systems). During all scans, animals were kept on a heating pad inhaling 2**–**2.5% isoflurane/oxygen gas, and their breathing conditions were continuously monitored. Scan durations and p.i. initiation (**I, III**) are summarised in Table 4. In study **III**, [^{18}F]EF5 was injected before the 2h hypoxia exposure, whereas [^{18}F]FDG and [^{18}F]F-DPA were injected immediately after hypoxia exposure.

Table 4. Timing of tracer injections in relation to initiation of PET scans and their durations for each radiotracer in studies I and III. Scan durations were selected based on the biological target under evaluation and known tracer-specific pharmacokinetic properties.

Study	Tracer	PET	PET scan started p.i. (min)	PET scan duration p.i. (min)
I	[^{18}F]F-DPA	Dynamic	0	0–60
	[^{11}C]PK11195	Dynamic	0	0–60
	[^{18}F]F-DPA	Static (*ex vivo*)	40	40–60
III	[^{18}F]EF5	Static	120	120–150
	[^{18}F]FDG	Static	40	40–60
	[^{18}F]F-DPA	Static	20	20–40

4.6 The integrated ^{15}O-gas PET system (II)

A comprehensive PET system was assembled to sequentially assess CBF and $CMRO_2$ in small animals. In its entirety, the system consists of a ^{15}O-oxygen–dedicated small cyclotron, a radiosynthesis and purification unit, a gas chromatograph for quality control, an inhalation controller, and a dedicated PET

scanner. In addition, a radioactive gas evacuation and decay-controlling system was required for effective scavenging of radioactive gases from the animal holder while ensuring radiation safety (Figure 10).

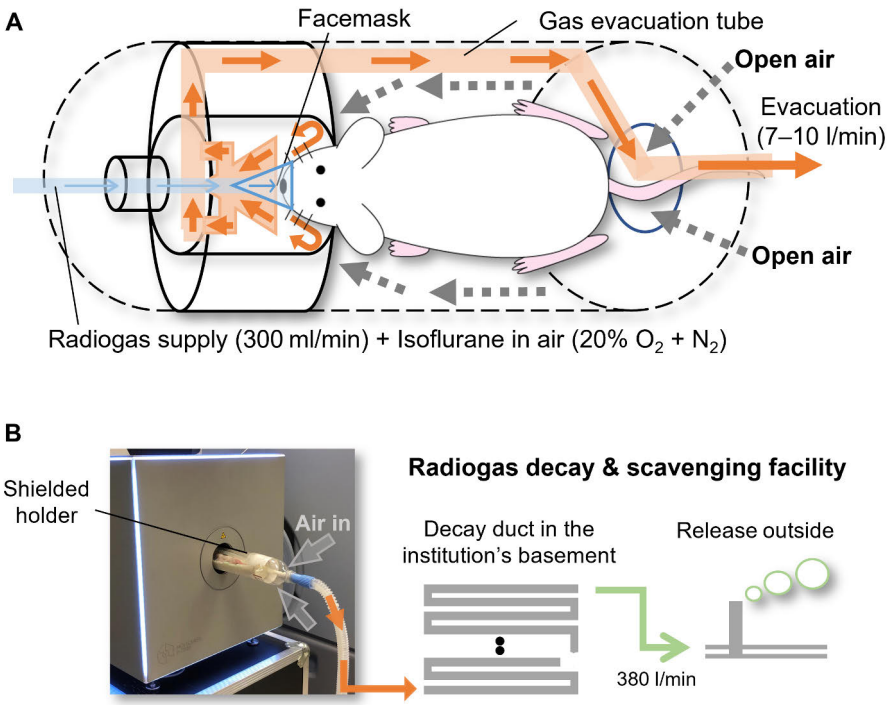

Figure 10. A schematic illustration of the integrated ^{15}O-labelled gas PET system assemblies. (**A**) The animal holder enables radioactive gases to be mixed with isoflurane in the air and inhaled spontaneously via a cone-shaped mask made of a thin fabric sheet covering the snout of the animal. Non-aspirated radioactive gas was scavenged from the front surrounding the gas supply tube through the gas evacuation tube (7–10 l/min). Fresh air passively entered the holder from the back. (**B**) The animal holder was completely sealed and radioactive gases were scavenged (380 l/min) from the animal holder to the decay ducts at the institute's basement. During the approximately 24-min passage through the duct, the radioactivity of ^{15}O-labelled gas (T½ = 2 min) decays before it is released externally from the chimney. *Adapted from II*.

4.6.1 Metabolism of inhaled [^{15}O]O_2

To assess the production rate of metabolised [^{15}O]H_2O (k_w) in arterial blood after [^{15}O]O_2 inhalation, an intravascular catheter was inserted in the left common carotid artery of healthy rats at 3 weeks (n = 7, 65.6 ± 1.0 g) and 5 weeks of age (n = 6, 155.0 ± 30.1 g). The animals were then placed in an animal holder attached to the HRRT scanner. After a 6-min attenuation correction scan, a 6-min dynamic PET scan was started 15 s before the initiation of [^{15}O]O_2 inhalation. Arterial blood samples (4–5

times at 30 s intervals) were manually obtained after initiating [^{15}O]O_2 inhalation (Figure 11). Plasma and whole-blood radioactivity concentrations were measured using a BeWell-Q3 well counter (Molecular Imaging Labo).

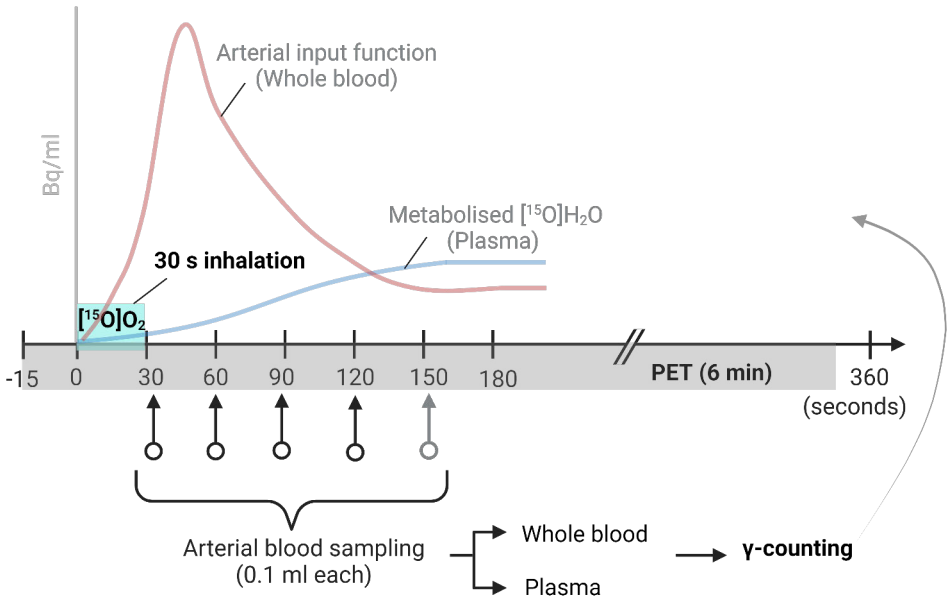

Figure 11. Blood sampling timeline to determine the rate of metabolised [^{15}O]H_2O (k_w). *Created using BioRender.com.*

4.6.2 PET imaging with [^{15}O]-labelled gases

Sequential PET/CT scans were performed with HIE, non-operated, and sham pups using β- and X-cubes. After the induction of isoflurane anaesthesia, a series of list-mode PET scans were acquired, as illustrated in Figure 12. Two 14-min scans were started at the time of continuous inhalation of both [^{15}O]O_2 and [^{15}O]CO_2 over 8 min. A separate 10-min scan was acquired from the time of initiating continuous inhalation of [^{15}O]CO over 3 min on one HIE pup on days 1, 7, and 14 before the [^{15}O]O_2 and [^{15}O]CO_2 scans to assess CBV. Thereafter, the holder containing the animal was moved to the CT scanner (X-cube) for attenuation correction. During all scans, animals were kept on a heating pad inhaling 2–2.5% isoflurane/oxygen gas, and their breathing conditions were continuously monitored.

These sequential scans were repeated four times, first within 6 h (day 0) and then at 24 h (day 1), 48 h (day 2), 7 days (day 7), and 14 days (day 14) post-insult for HIE pups. Age-matched non-operated pups were sequentially scanned four times at ages equivalent to those of HIE pups on days 0, 2, 7, and 14. Sham pups were scanned

only on day 7 after the surgical intervention. The PET imaging time course with postoperative days and ages for the three study groups is presented in Table 1 in **II**. Image data analysis excluded animals with poor radioactivity inhalation doses in the body during scanning or inconstant body positions between [^{15}O]O_2 and [^{15}O]CO_2 scans.

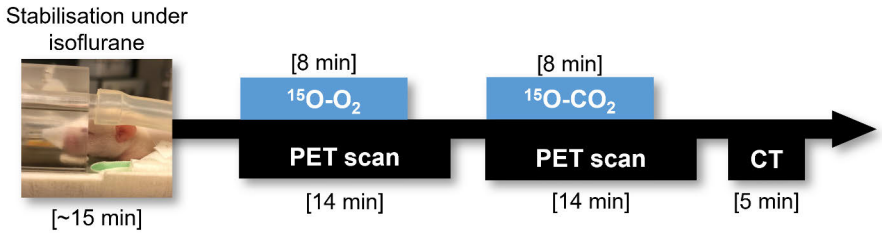

Figure 12. ^{15}O-gas PET/CT protocol consisting of two separate 14-min scans for 8 min inhalation of [^{15}O]O_2 and [^{15}O]CO_2 followed by CT acquisition, was applied to HIE, non-operated, and sham animals. *Adapted from II*.

4.7 PET data processing (I–III)

PET images were reconstructed using three-dimensional ordered-subsets expectation–maximisation (3D OSEM) with depth-of-interaction compensation in Molecubes and shifted Poisson model maximum-a-posteriori (SP-MAP) in Inveon. The time frames to generate dynamic images were 10 × 2 s, 4 × 10 s, 4 × 60 s, 5 × 300 s, 3 × 600 s for 60 min in study **I**; 12 × 5 s, 8 × 15 s, 6 × 30 s for 6 min in the 1st part, a 1-min frame duration for an entire period of 14 min for [^{15}O]O_2 and [^{15}O]CO_2 scans and 10 min for [^{15}O]CO scans in the 2nd part of study **II**. Study **III** only performed static scans. Data were corrected for injected activity and decay except for the 2nd part of study **II**.

4.8 PET data analysis (I–III)

Carimas® 2.1 software (Turku PET Centre) (Rainio *et al*., 2023) was used to analyse the PET/CT images in **I** and **II**. In study **III**, the Inveon Research Workplace (v. 4.2, Siemens) was used.

To determine the *in vivo* uptake of [^{18}F]F-DPA and [^{11}C]PK11195 (**I**), volumes of interest (VOIs) were drawn in the spinal cord at L3–L6 (inflammation site at lumbar level) and T11–T12 (reference region at thoracic level), as well as on the vertebral body to assess the bone accumulation of [^{18}F]F-DPA. Mean standardised uptake values (SUVs) for each VOI were calculated for the summed 40–60 min period. For *ex vivo* uptake of [^{18}F]F-DPA in the removed brain and spinal cord, CT-

guided images were used to locate VOIs of the exact same size in the lumbar and thoracic spinal cord areas of each rat.

In the 1st part of study **II**, whole-blood time-activity curves (TACs) were obtained from the left ventricular (LV) region in the reconstructed images. Counter-based radioactivity concentrations of whole blood were used to verify the use of the LV-based AIF. Plasma radioactivity concentrations were converted to arterial $[^{15}O]H_2O$ concentrations by referring plasma to the whole radioactivity concentration ratio. The arterial blood concentration of $[^{15}O]O_2$ (in Bq/ml) was then obtained by subtracting the $[^{15}O]H_2O$ concentration from the whole-blood radioactivity concentration at each sampling time point. VOIs were drawn in the LV cavity region, and the model formulations were employed to estimate the production rate of the metabolised $[^{15}O]H_2O$ (k_w), as described in **II**. A numerical simulation was also performed to evaluate the difference of results for $CMRO_2$ and CBF values if the true k_w differs from the fixed k_w value obtained as an average for each population.

In the 2nd part of study **II**, parametric values of CBF and $CMRO_2$ were calculated from two VOIs selected in the ipsilateral and contralateral hemispheres. Time courses of absolute CBF (ml/min/g) and $CMRO_2$ (ml/min/g) in the ipsi- and contralateral brain VOIs were evaluated in the HIE, non-operated, and sham groups over 14 days after the day of the HI insult (day 0) or at the age of P9. Age, group, and hemispheric region dependency of CBF and $CMRO_2$ were evaluated at each time point and between animal groups.

In study **III**, the uptake of $[^{18}F]$EF5 was determined by placing VOIs on the entire injured hemisphere (ipsilateral) and relating it to whole brain uptake. For $[^{18}F]$FDG and $[^{18}F]$F-DPA analyses, age-matched MRI templates were used as anatomic references for drawing VOIs over the whole hemisphere or each of the following brain subregions separately: hippocampus, cortex, striatum, and olfactory bulb. Mean SUV ratios were calculated for ipsilateral (injury)/contralateral (control) hemispheres (I/C ratio). For $[^{18}F]$FDG and $[^{18}F]$F-DPA analyses, I/C ratios were also obtained for each brain region.

4.9 *Ex vivo* biodistribution (I)

PSNL animals were sacrificed at 40 min p.i. of $[^{18}F]$F-DPA via cardiac puncture under deep anaesthesia with 4% isoflurane and perfused transcardially with PBS. The spinal cord (lumbar region at L3–L6 and thoracic region at T11–T12), vertebral body (L1), blood, and bone from the skull were harvested for γ-counting (2480 WIZARD2, PerkinElmer). Mean SUVs were calculated for each sample using the same equation used for PET images.

4.10 *Ex vivo* ARG (I, III)

Animals were sacrificed by cardiac puncture and transcardial perfusion at designated time points (Table 5). The brains or spinal cords were rapidly removed, frozen in chilled isopentane, and cut into 20-µm ([^{18}F]F-DPA, [^{18}F]EF5, [^{18}F]FDG) or 40-µm ([^{11}C]PK11195) thick coronal sections using a cryomicrotome (Leica CM3050S). The slides were then exposed to imaging plates (Fuji BAS Imaging Plate TR2025) for approximately two half-lives of the radioisotope and scanned with a Fuji BAS5000 analyser. The images were analysed for ^{18}F or ^{11}C radioactivity count densities expressed as background-subtracted photostimulated luminescence per area (PSL/mm^2).

Table 5. Animal sacrifice time points for each tracer p.i. in *ex vivo* studies I and III

Study	Tracer	Sacrifice time point p.i. (min)
I	[^{18}F]F-DPA	40
	[^{11}C]PK11195	30
III	[^{18}F]EF5	150
	[^{18}F]FDG	60
	[^{18}F]F-DPA	40
	[^{11}C]PK11195	40

Regions of interest (ROIs) were placed over the ipsilateral and contralateral regions of the spinal cord at the lumbar spinal cord (inflammation site) level, and I/C ratios were calculated (Figure 13) in study **I**. Additional ROIs were drawn over the whole spinal cord at the lumbar and thoracic levels, and lumbar-to-thoracic (L/T) ratios were calculated. The thoracic and contralateral lumbar spinal cord were used as reference regions.

In study **III**, ROIs were drawn over the entire ipsilateral and contralateral brain hemispheres at the hippocampal level in HIE and sham animals. The I/C uptake ratio was calculated from the PSL/mm^2 value in each ROI.

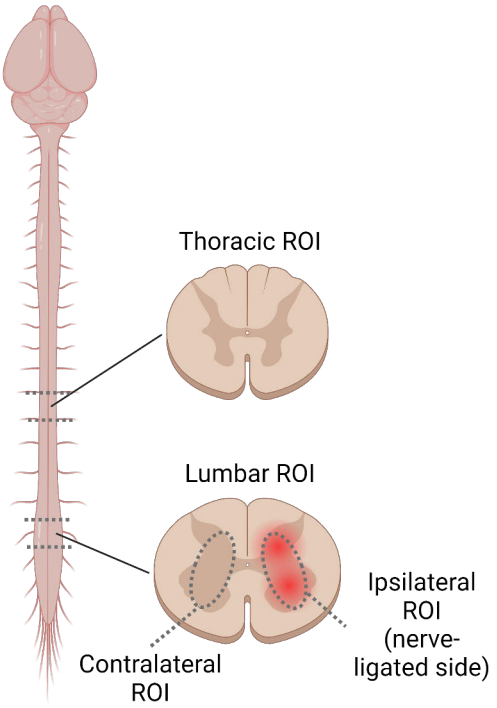

Figure 13. ROIs for ARG analysis (**I**) comparing the whole lumbar spinal cord (target) with the whole thoracic spinal cord (reference) or the ipsilateral side (target) with the contralateral side (reference) at the lumbar level. *Created using BioRender.com.*

4.11 Specificity of [^{18}F]F-DPA for targeting TSPO (I, III)

To determine the specific binding potential of the [^{18}F]F-DPA to TSPO, 1 mg or 3 mg of the TSPO-specific ligand, PK11195 (ABX GmbH), was injected intraperitoneally to two PSNL rats in study **I** and one HIE pup in study **III**, 30 min prior the [^{18}F]F-DPA injection. The animals were sacrificed 40 min after the [^{18}F]F-DPA injection and the spinal cords and brains were sliced for autoradiography analyses as described in 4.10.

4.12 Histology and IHC (I–III)

H&E (**II**) and Cresyl violet (**III**) staining procedures were used to detect morphological changes in paraffin-embedded brain sections after transcardial fixation with 4% paraformaldehyde (**II**) or 10 % formalin (**III**). In study **II**, coronal slices were obtained in 2-mm intervals from the frontal pole to the cerebellum of HIE and non-operated rat brains after PET scan on day 14. The hemispheric volume

of each brain was calculated by summing the hemispheric area (mm^2) of each H&E-stained brain slice and multiplying the sum of the section thickness. The mean I/C hemispheric volume ratios were compared between the HIE and non-operated groups. Additionally, the I/C hemispheric volume ratios in each HIE animal were compared with the I/C ratios of CBF and $CMRO_2$ obtained on day 14 (**II**). The I/C ratio of $CMRO_2$ in the early phase on day 2 was also compared with the hemispheric volume loss outcome on day 14. Study **III** assessed brain volume loss in hippocampus-level sections of HIE rats 21 days after injury to determine the predictive value of early [^{18}F]FDG uptake in injured brains. The area (mm^2) of volume loss in the injured brain hemisphere was determined as (contralateral-ipsilateral hemisphere)/contralateral brain hemisphere × 100, which was compared with [^{18}F]FDG SUV ratios (I/C) obtained from *in vivo* PET on day 1 after injury.

For IHC staining, fresh-frozen spinal cords (**I**) and paraffin-embedded brains (**II**, **III**) were used. Antigen retrieval was performed using citrate buffer (pH 6) and a pressure cooker. Staining was performed using a Labvision autostainer (Thermo-Fisher Scientific). Endogenous enzyme activity was blocked by hydrogen peroxide. The sections were then incubated with a primary antibody followed by the corresponding secondary antibody (Table 6). Staining was detected using BrightDAB substrate. All sections were counterstained with Mayer's haematoxylin.

Table 6. Antibodies used for IHC in studies I–III

Study	Ab	Imaging target	Dilution	Ab type	Provider Cat no.	Secondary Ab
I	Iba1	Activated microglia	1:1000	Polyclonal	Wako Ltd # 019-19741	Goat anti-rabbit (Orion)
	GFAP	Activated astrocytes	1:1000	Polyclonal	Sigma # G9269	Goat anti-rabbit (BrightVision)
II, III	Iba1	Activated microglia	1:2000	Polyclonal	Wako Ltd # 019-19741	Goat anti-rabbit (BrightVision)
III	GFAP	Activated astrocytes	1:100	Polyclonal	Abcam # ab4674	Goat anti-rabbit (BrightVision)
	MAP2	Neuronal dendrites	1:8000	Monoclonal	Abcam # ab183830	Goat anti-rabbit (BrightVision)
	NeuN	Neuronal cells	1:3000	Monoclonal	Abcam # ab177487	Goat anti-rabbit (BrightVision)

Abbreviations: Ab = antibody.

4.13 Statistical analysis (I–III)

In study **I**, pain sensation data was analysed with a linear mixed model for repeated measurements, in which a group was handled as the between factor and time as the

within factor. If significance was found, the contrast was programmed into pairwise time point interactions. Ratios were analysed using an unpaired t-test. Multi-way analysis of variance (ANOVA) was used to study the effects of the scanner, tracer, and region on SUVs. The testing assumptions were checked using studentised residuals. In study **II**, Student's paired or unpaired Student's t-test was used to compare two variables as appropriate. Pearson's correlation coefficient was used to test for correlations between two continuous variables. In study **III**, one-way ANOVA was used when the independent group means were compared over a continuous response. After obtaining significant results, pairwise comparisons were performed within the model, and Dunnett's pairwise correction was applied, when applicable. If the same rats were measured over time, linear mixed models for repeated measurements were used. The model included group (between effect), time point (within effect), and group × time interaction. Pairwise comparisons between groups and within-time comparisons were made in this model. A compound symmetry covariance structure was used. The Pearson correlation coefficient was calculated between two continuous variables to describe the strength of the association. Additionally, the SUV ratio was compared between grouped severity of brain volume loss in the whole hemisphere and hippocampus using the Wilcoxon rank sum test. In all studies, the threshold for statistical significance was set at $p < 0.05$.

5 Results

5.1 Characterisation of the NPP animal model

From day 3 onwards until day 7 postoperatively, all PSNL-operated animals showed symptoms of allodynia in the ipsilateral hind paw (Figure 14). The paw withdrawal response to the weakest stimulation of 0.67 ± 0.31 g filament on the ipsilateral side compared with that of 7.6 ± 3.0 g on the contralateral side ($p < 0.0001$) was detected on day 3. This decreased threshold value in the ipsilateral paw persisted until day 7 thereafter (0.77 ± 0.33 g vs. 7.3 ± 2.0 g, $p < 0.0001$).

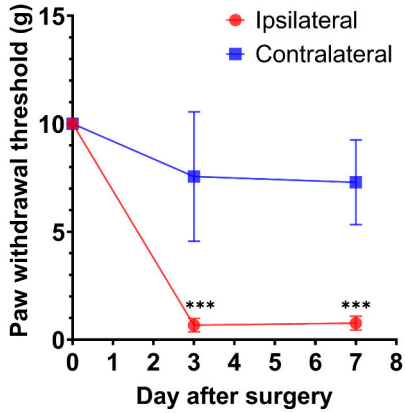

Figure 14. Tactile-evoked mechanical allodynia detected by the von Frey filament test after partial sciatic nerve ligation. A significantly decreased threshold (g) of the withdrawal response in the ipsilateral paw relative to the contralateral paw was observed from day 3 to day 7 post-injury. Data are presented as mean ± standard deviation (SD), ***$p < 0.0001$, n = 7/group. *Adapted from I.*

5.2 Assessment of the inflamed region

Assessment of PET tracers to reveal the inflamed spinal cord region was conducted 7 days after PSNL surgery by *in vivo* whole-body PET imaging, *ex vivo* PET imaging of the removed brain and spinal cord, and *ex vivo* γ-counting and *ex vivo* ARG of the spinal cord.

5.2.1 PET imaging of the inflamed spinal cord region

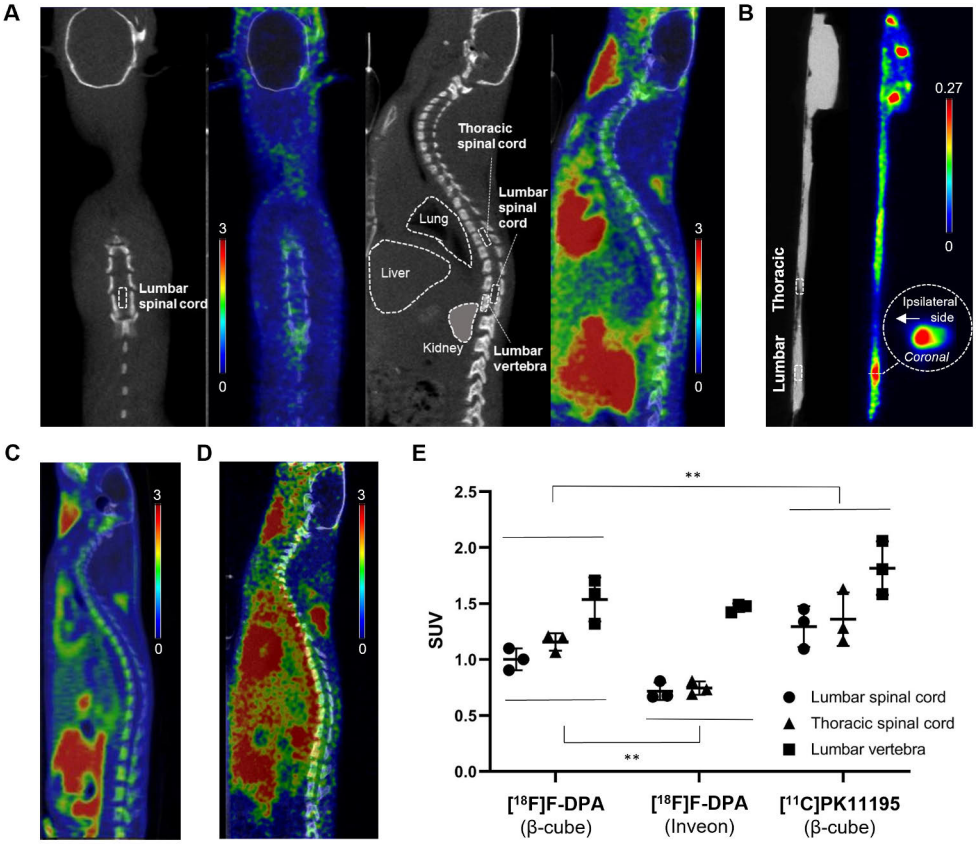

Figure 15. PET/CT imaging results of PSNL rats. (**A**) *In vivo* [^{18}F]F-DPA PET/CT with β-cube. Analysed VOIs with anatomical references are illustrated in CT images. (**B**) *Ex vivo* [^{18}F]F-DPA PET/CT with β-cube with enlarged coronal view of the lesion. (**C**) *In vivo* [^{18}F]F-DPA PET/CT with Inveon. (**D**) *In vivo* [^{11}C]PK11195 PET/CT with β-cube. (E) SUVs in selected VOIs were compared between three *in vivo* imaging conditions (A, C, and D). Data are presented as mean ± SD, $^{**}p < 0.01$, n = 3/group. Scale bars represent SUVs. *Adapted from I.*

A typical whole-body image of *in vivo* [^{18}F]F-DPA uptake in a PSNL rat taken by β-cube is presented in Figure 15A, not allowing any visual inspection of specific accumulation in the inflamed spinal cord region of PSNL animals. In contrast, e*x vivo* [^{18}F]F-DPA PET scans of the removed spinal cords with β-cube revealed a clearly increased uptake of [^{18}F]F-DPA at the inflammation site, which was furthermore located on the ipsilateral side of the lumbar spinal cord (Figure 15B). The [^{18}F]F-DPA uptake in the lumbar region of sham animals was homogenously distributed (**I**, Figure 4). The SUV_{max} at the lumbar inflammation site was

approximately 0.3 when measured with *ex vivo* PET imaging. In contrast, a higher level of low-frequency background was observed in the SUV values of 1.00 ± 0.10 and 1.16 ± 0.08 in the lumbar and thoracic regions of the spinal cord, respectively, in *in vivo* PET imaging with β-cube (Figure 15E). The corresponding values obtained using the Inveon scanner were 0.72 ± 0.08 and 0.75 ± 0.06, respectively (Figure 15E), indicating inferior spatial resolution and statistical noise compared with the β-cube (Figure 15C). Furthermore, [^{11}C]PK11195 also failed to visualise the inflamed area *in vivo*, in which an even significantly higher background was observed in the spinal cord and vertebral regions compared with that of [^{18}F]F-DPA (Figure 15D, E).

5.2.2 ^{18}F radioactivity uptake in tissues

Ex vivo tissue γ-counting for ^{18}F radioactivity divided by the mass of the whole removed lumbar spinal cord, including both inflamed and non-inflamed tissues, showed no significant difference in SUVs (0.23 ± 0.07) compared with thoracic spinal cords (0.27 ± 0.09). SUV uptake measured in the lumbar vertebral body (0.78 ± 0.20) was 2-fold higher than that detected in the skull (0.41 ± 0.17).

5.2.3 Localisation of inflamed area

Digital ARG revealed significantly higher ^{18}F radioactivity uptake in the ipsilateral dorsal and ventral horns of the lumbar spinal cord (Figure 16A). Animals premedicated with the TSPO ligand, PK11195, reduced the [^{18}F]F-DPA uptake by 70% (1-mg dose), whereas complete blockade was achieved with a 3-mg dose of PK11195 (**I**, Figure 3). IHC staining showed increased numbers of reactive microglia (Figure 16B) in these areas, whereas astrocyte upregulation was not distinctive.

The I/C and L/T ratios of [^{18}F]F-DPA uptake were significantly higher ($p < 0.01$) than those of [^{11}C]PK11195 (Figure 17C). No specific [^{18}F]F-DPA accumulation was observed in the spinal cords of the sham animals.

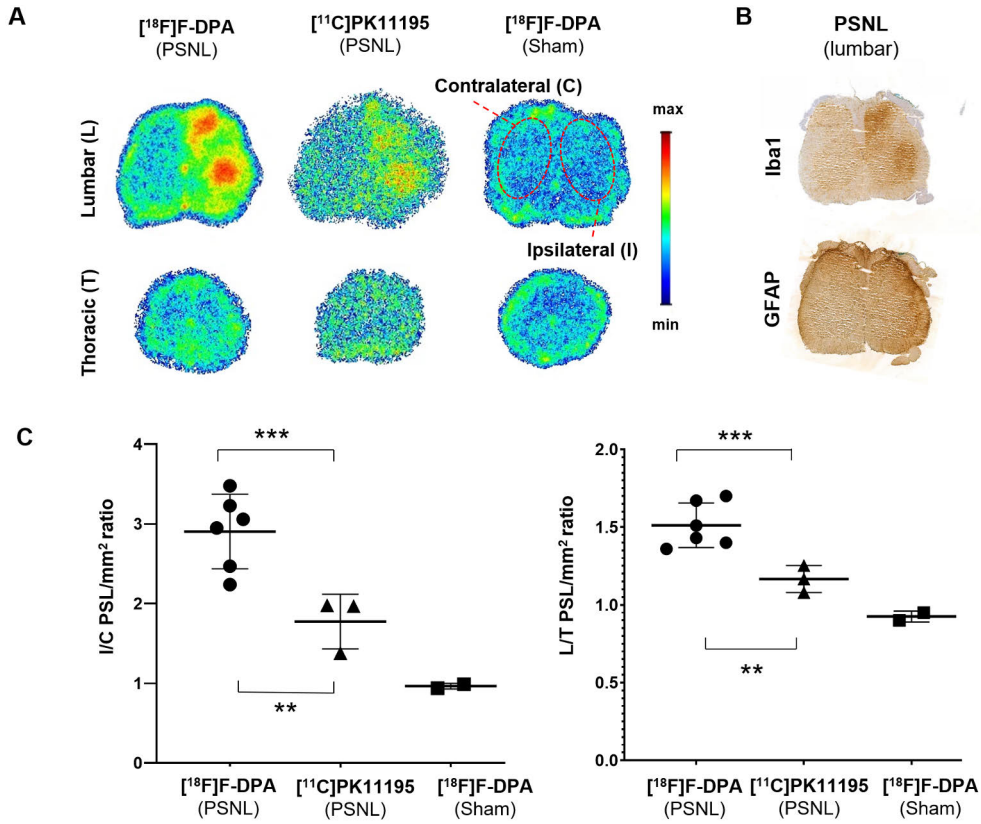

Figure 16. (**A**) Typical examples of *ex vivo* ARG images p.i. of [^{18}F]F-DPA and [^{11}C]PK11195 in PSNL rats, showing specific tracer accumulation in the ipsilateral dorsal and ventral horns of the lumbar spinal cord. Sham animals did not exhibit any specific [^{18}F]F-DPA accumulation. (**B**) Iba1 and GFAP staining showed increased microglial expression without astrogliosis in regions corresponding to [^{18}F]F-DPA uptake. (**C**) I/C and L/T ratios demonstrated better specificity for [^{18}F]F-DPA than [^{11}C]PK11195. Data are presented as mean ± SD, ***$p < 0.0001$, **$p < 0.01$. *Adapted from I.*

5.3 Production rate of metabolised [^{15}O] H_2O (k_w)

In the 1st part of **II**, non-operated rats in younger and older subject groups underwent multiple arterial blood samplings after a 30-s inhalation of [^{15}O]O_2 to obtain age-dependent k_w values. Whole-blood radioactivity concentrations measured by γ-counter were confirmed consistent with PET image-derived LV TAC. The predicted metabolised [^{15}O]H_2O TAC was then fitted to the manually separated [^{15}O]H_2O TAC. The resulting k_w values are summarised in Table 7, revealing no significant differences between each animal group. k_w value was accordingly defined as 0.33 min^{-1}, which was applied for the quantification of CBF and $CMRO_2$ for all subjects in the 2nd part of study **II**.

Table 7. Animal number, age, body weight, and resulting k_w values in each animal group in study II*.

	Number of animals	Age (d/o)	Body weight (g)	K_W value (min^{-1})
Younger group	7 (4)	25.7 ± 1.0 25.5 ± 1.0)	65.6 ± 1.0 (63.0 ± 0.8)	0.33 ± 0.06
Older group	6 (4)	40.3 ± 0.8 (40.0 ± 0.0)	155.0 ± 30.1 (166.5 ± 20.6)	0.33 ± 0.07

*Data are presented as mean ± SD. Numbers in parentheses denote values after exclusion from the image data analysis. **Abbreviations:** d/o = days old.

The numerical simulation in the case that the individual true k_w is different by ±20% (approximately one standard deviation [SD] of the variation in the k_w estimates) was further evaluated for the results of day 14 as a worst case because of the highest CBF and $CMRO_2$ in the 2nd part of the study (Table 8). This indicates that the magnitude of errors is small and most likely lies at a negligible level in practical use.

Table 8. Error propagation analysis of k_w affecting CBF and $CMRO_2$ in each VOI.

	CBF		**$CMRO_2$**	
Changing k_w	Ipsilateral	Contralateral	Ipsilateral	Contralateral
+20%	−3.7%	−7.5%	+8.4%	+3.1%
−20%	+0.0%	+2.9%	−4.1%	−1.0%

5.4 Evaluation of ^{15}O-labelled gas PET system

In the 2nd part of **II**, HIE and control animals underwent sequential ^{15}O-PET imaging over 14 days (Table 1, **II**). The images obtained during ^{15}O gas inhalation in a HIE rat at different developmental stages are presented in Figure 17, displaying the whole-body distribution of inhaled ^{15}O gases and excess radiogases that remained in the FOV as sagittal PET/CT images for the periods of 0–5 min ($[^{15}O]O_2$) and 0–8 min ($[^{15}O]CO_2$). Some radioactivity spots were visible around the gas supply tube in the animal holder but were negligible for image analysis. Lower accumulation in the brain and greater accumulation in the lung region relative to the heart were observed for $[^{15}O]O_2$ compared with $[^{15}O]CO_2$.

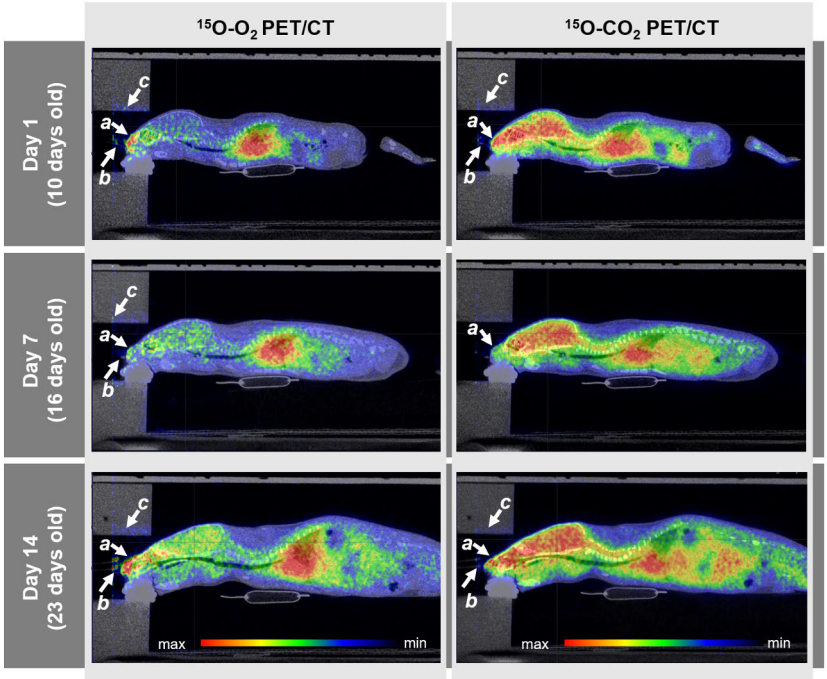

Figure 17. Representative sagittal whole-body PET/CT images of a HIE rat situated in the animal holder on days 1, 7, and 14 post-HI insult, displaying summed images over 0–5 min and 0–8 min with [^{15}O]O_2 and [^{15}O]CO_2 inhalation, respectively. White arrows (***a–c***) indicate the effects of radioactivity on the snout (***a***), gas supply tube (***b***), and inner surface of the animal holder (***c***). *Adapted from II.*

5.5 PET findings in neonatal HIE

5.5.1 Temporal changes in CBF and $CMRO_2$

Absolute values of CBF and $CMRO_2$ in each hemisphere were calculated through non-linear least square fitting (NLLSF) analysis of dual-tracer PET images with [^{15}O]O_2 and [^{15}O]CO_2 as described in **II**. The mean quantitative hemispheric CBF and $CMRO_2$ values are displayed as a function of postoperative time in HIE and sham animals or the corresponding postnatal days in non-operated animals (Figure 18). CBF and $CMRO_2$ in non-operated pups significantly increased along with normal maturation from 9 to 23 days of age ($p < 0.01$ and $p < 0.05$, respectively) by a factor of roughly 2.5 and 2, respectively. When comparing CBF and $CMRO_2$ between each hemisphere of HIE pups, ipsilateral hemispheres presented significantly lower values than contralateral ones at all time points in CBF (Figure 18A) and except on day 0 in $CMRO_2$ (Figure 18B). Sham animals scanned only on day 7 showed no significant interhemispheric differences in both values. Analysis of

time-dependent changes in each value in HIE pups revealed that CBF in the ipsilateral hemispheres significantly decreased to the lowest level on day 2 ($p < 0.0001$, compared with day 1) and then increased on day 7 ($p < 0.01$) and day 14 ($p < 0.01$) compared with day 2 (Figure 18A). $CMRO_2$ in the ipsilateral hemispheres also reached its lowest level on day 2 ($p < 0.01$, compared with day 1) and significantly increased on day 14 thereafter ($p < 0.05$) (Figure 18B).

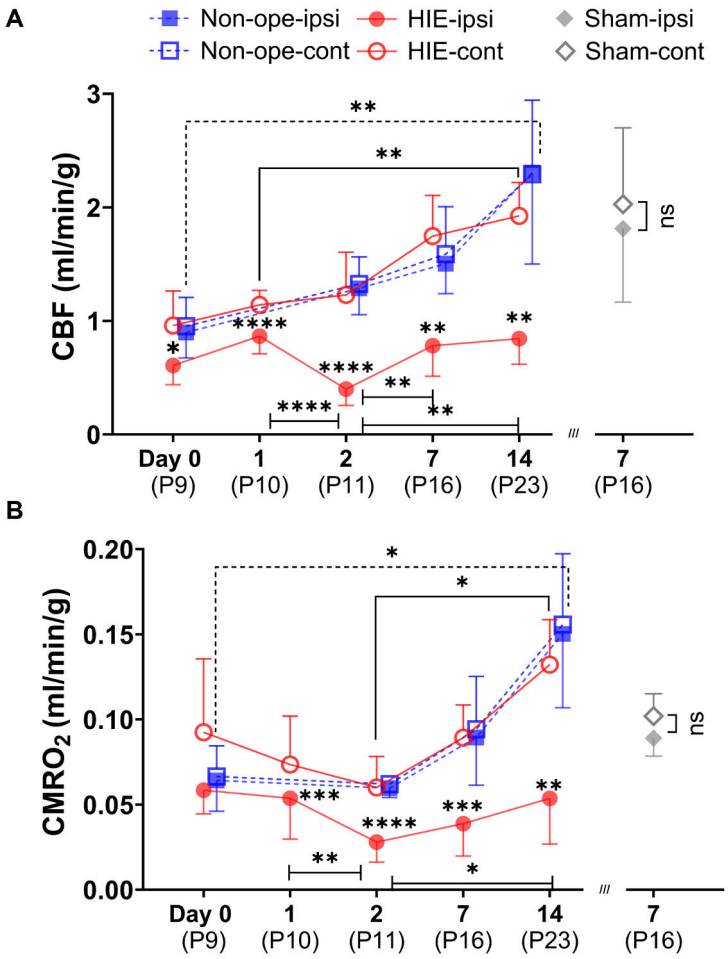

Figure 18. Mean temporal values of (**A**) CBF (ml/min/g) and (**B**) $CMRO_2$ (ml/min/g) in VOIs selected in the ipsilateral (closed) and contralateral (open) hemispheres of HIE (circle), non-operated (square), and sham (diamond) rats. HIE rats were scanned on days 0, 1, 2, 7, and 14 after surgery. Sham rats were scanned only on day 7. Non-operated pups were scanned at corresponding ages P9, P11, P16, and P23. Values are expressed as mean ± SD. A pair of each imaging time point or hemisphere was compared using Student's paired t-test. Asterisks shown above closed circles indicate significant differences between each hemisphere in HIE rats. *$p < 0.05$, **$p < 0.01$, ***$p < 0.001$, ****$p < 0.0001$, ns; not significant. *Adapted from II.*

5.5.2 *In vivo* PET evaluation of pathological progression

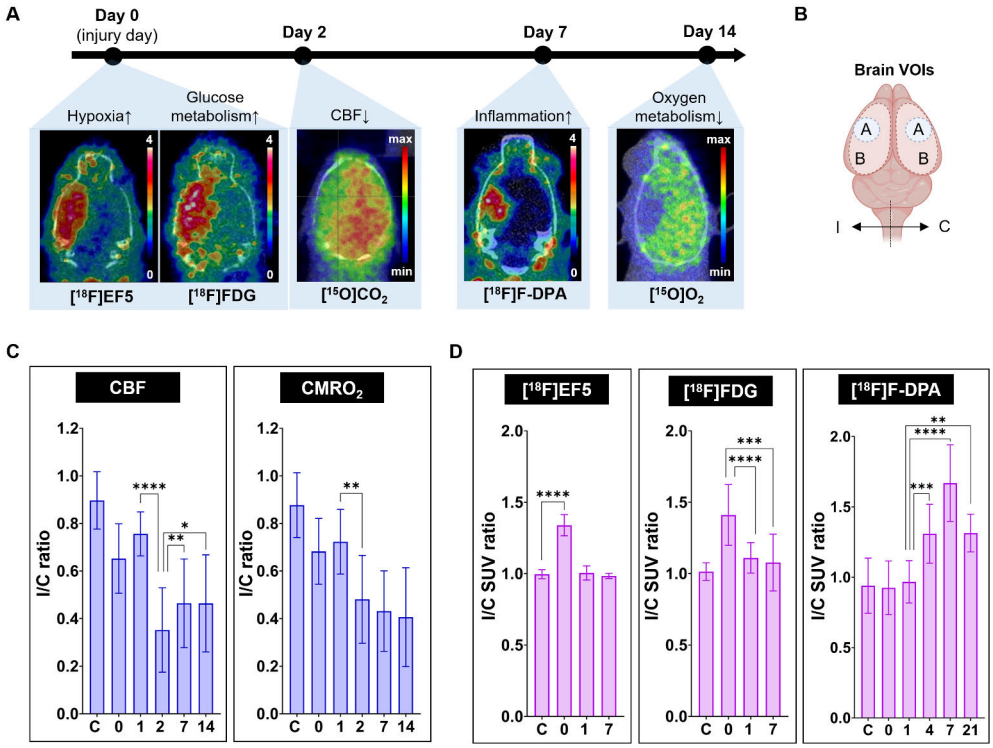

Figure 19. *In vivo* PET results of HI damage progression. (**A**) Representative transverse PET/CT images of each tracer, showing distinct uptake patterns at different phases post-insult. (**B**) CBF and $CMRO_2$ were calculated in VOIs (areas A) from $[^{15}O]CO_2$ and $[^{15}O]O_2$ images, whereas SUV_{mean} ratios were analysed in selected VOIs (areas B) from $[^{18}F]$EF5, $[^{18}F]$FDG, and $[^{18}F]$F-DPA images. (**C**) I/C ratios of CBF and $CMRO_2$ (0–14 d after injury). C: control group (non-operated). (**D**) I/C SUV_{mean} uptake ratios of $[^{18}F]$EF5 and $[^{18}F]$FDG (0–7 d after injury) and $[^{18}F]$F-DPA (1–21 d after injury). C: control group (sham-operated). Values are expressed as mean ± SD. $[^{18}F]$EF5: n = 2–12/group, $[^{18}F]$FDG: n = 5–12/group, $[^{18}F]$F-DPA: n = 5–14/group, CBF and $CMRO_2$: n = 4–11/group. *$p < 0.05$, **$p < 0.01$, ***$p < 0.001$, ****$p < 0.0001$. *Adapted from II and III.*

Figure 19A displays representative PET/CT images of each tracer, showing distinctive accumulation patterns at each time point after HI injury. Temporal changes in the I/C ratios of CBF and $CMRO_2$ (Figure 19C) or the I/C SUV_{mean} ratios of $[^{18}F]$EF5, $[^{18}F]$FDG, and $[^{18}F]$F-DPA (Figure 19D) in the selected VOIs in HIE pups are also shown. The I/C CBF ratio reached the lowest level on day 2 ($p < 0.0001$, compared with day 1) and gradually increased until day 14. I/C $CMRO_2$ ratios showed a significant reduction on day 2 from day 1 ($p < 0.01$), similar to CBF, but without any significant temporal changes thereafter. The highest SUV_{mean} I/C ratios of $[^{18}F]$EF5 and $[^{18}F]$FDG were seen on the injury day (day 0). These uptakes

significantly declined 1 day later ($p < 0.0001$) and remained at a similar level until day 7. Increased I/C SUV_{mean} ratios of [^{18}F]F-DPA became noticeable on day 4 ($p < 0.001$, compared with day 1), peaked on day 7 ($p < 0.0001$, compared with day 1), and remained evident until day 21. Regional I/C SUV_{mean} ratio analysis with [^{18}F]FDG and [^{18}F]F-DPA revealed that these uptake patterns were detectable in the hippocampus, cortex, and striatum (**III**, Figure 2).

5.5.3 *Ex vivo* localisation of brain pathology

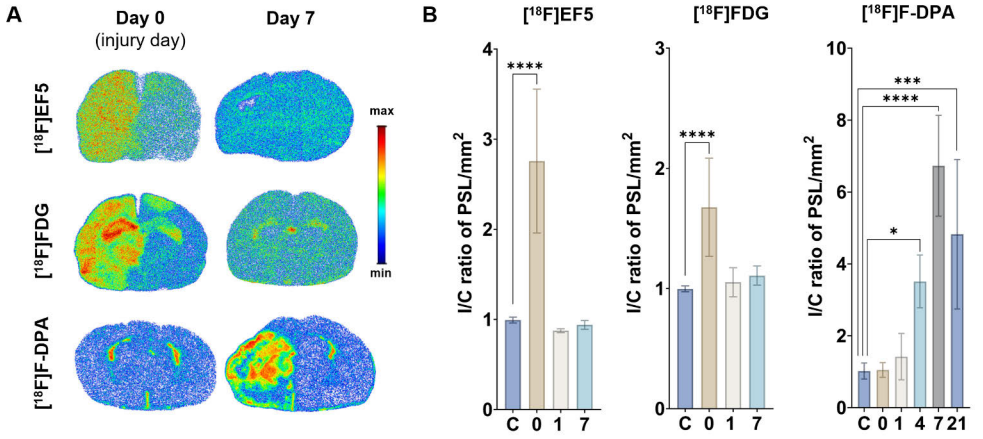

Figure 20. *Ex vivo* localisation of HI brain damage. (**A**) Representative ARG images of coronal brain sections at the hippocampal level from HIE animals showing different temporal and regional uptake patterns of [^{18}F]EF5, [^{18}F]FDG, and [^{18}F]F-DPA. (**B**) I/C ratios of [^{18}F]EF5 and [^{18}F]FDG (0–7 d after injury) and [^{18}F]F-DPA (0–21 d after injury) uptakes were analysed. C: control group (sham-operated). Data are expressed as mean ± SD of photostimulated intensity per area − background (PSL/mm^2). [^{18}F]EF5: n = 2–8/group, [^{18}F]FDG: n = 4–8/group, [^{18}F]F-DPA: n = 3–6/group. *p < 0.05, ***p < 0.001, ****p < 0.0001. *Adapted from III*.

The time-dependent ARG uptake patterns of [^{18}F]EF5, [^{18}F]FDG, and [^{18}F]F-DPA were consistent with the *in vivo* PET findings, as shown in Figure 20A. A uniform accumulation of [^{18}F]EF5 was observed in the entire ipsilateral hemisphere of HIE pups on day 0. This uptake was significantly higher in HIE pups than in control pups ($p < 0.0001$) (Figure 20B) and returned to baseline. When [^{18}F]EF5 was injected after a hypoxic insult (n = 7), transient [^{18}F]EF5 uptake was localised to the cortical region only (**III**, Supplementary Figure 3). [^{18}F]FDG showed the highest uptake on day 0 and diminished in the later phase ($p < 0.0001$). Increased [^{18}F]F-DPA uptake was observed from day 4 ($p < 0.05$), maximised on day 7 ($p < 0.0001$), and remained distinct on day 21 ($p < 0.001$). Pretreatment with 1 mg of PK11195 completely

inhibited [^{18}F]F-DPA uptake in the HIE brain (**III**, Supplementary Figure 4). Regional brain uptake analysis revealed that [^{18}F]FDG uptake on day 1 was the most prominent in the hippocampal region ($p < 0.05$), whereas [^{18}F]F-DPA showed preferential accumulation over the cortical ($p < 0.01$) and hippocampal ($p < 0.05$) areas on day 7 compared with the contralateral hemispheres (**III**, Figure 4).

5.6 Histopathology of HIE brains

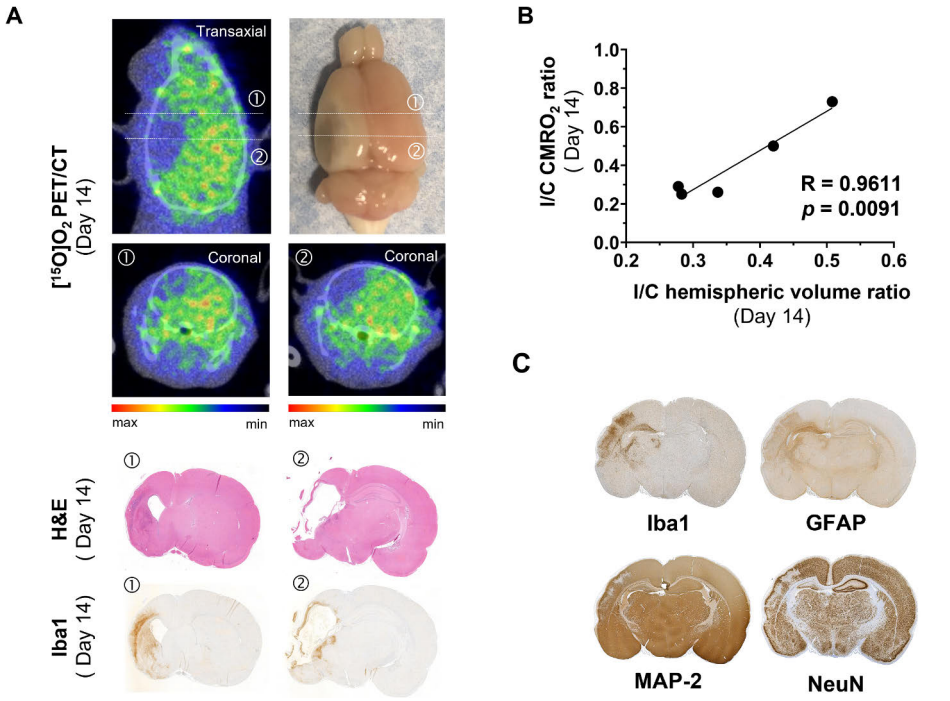

Figure 21. Histopathological findings compared with *in vivo* PET results. Representative [^{15}O]O_2 PET/CT images of the transaxial view in comparison with the dorsal view of the brain removed post-mortem from a HIE rat on day 14 post-injury. Coronal views at the level of the striatum (1) and hippocampus (2) are presented (**A**). PET images are shown as summed images over 0–5 min after the initiation of [^{15}O]O_2 inhalation. H&E- and Iba1-stained sections of the same animal are also displayed at equivalent coronal slicing levels. (**B**) Significant correlation between the I/C ratios of $CMRO_2$ and hemispheric volume in histology measured on day 14 in each HIE rat (n = 5) was revealed ($p = 0.0091$). (**C**) IHC staining patterns against Iba1 (microglia), GFAP (astrocytes), MAP2 (microtubules), and NeuN (neurones) in hippocampal level brain sections of a HIE rat 7 d after injury. *Adapted from II and III*.

Figure 21A shows the [^{15}O]O_2 PET/CT images of a HIE rat on day 14 and the corresponding H&E-stained post-mortem brain section obtained after the PET study. The region showing decreased [^{15}O]O_2 accumulation reasonably agreed with the

infarct area detected in the H&E-stained section. Iba1 staining detected increased expression of reactive microglia around the margins of the infarct cores, where a slight decrease in [^{15}O]O_2 accumulation was observed *in vivo*. The I/C ratios of $CMRO_2$ in HIE pups were significantly correlated with the I/C hemispheric volume ratio measured by histological analysis ($p = 0.0091$) (Figure 21B).

Representative IHC images of a HIE rat on day 7 are shown in Figure 21C. The inflamed lesion was detected in the cortical and hippocampal areas of the injured hemisphere by Iba1 and GFAP, targeting reactive microglia and astroglia, respectively. The neuronal losses detected by MAP2 and NeuN were most prominent in the cortex area and were also visible in the hippocampal region in the affected hemisphere.

5.7 Predictive value of *in vivo* PET

The association between early *in vivo* tracer uptake and morphological brain damage in the later phase was evaluated using Pearson's correlation analysis (Figure 22). Increased I/C [^{18}F]FDG SUV ratios detected by *in vivo* PET on day 1 after injury were significantly correlated with greater brain volume loss levels histologically measured on day 21 ($p = 0.0283$) (Figure 22A). Decreased I/C $CMRO_2$ ratios of HIE rats measured by [^{15}O]gas PET on day 2 were also significantly correlated with decreased I/C hemispheric volume ratios detected on day 14 ($p = 0.0123$) (Figure 22B).

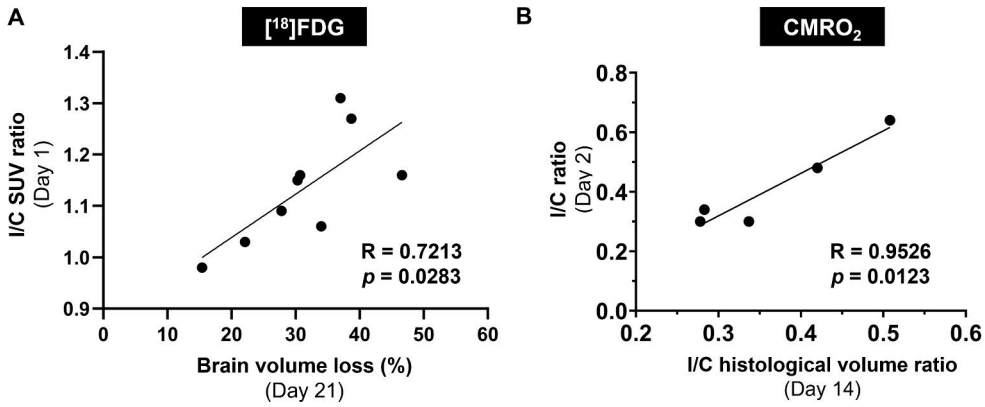

Figure 22. Predictive value of *in vivo* PET. Pearson's correlation analysis revealed significant correlations between I/C [^{18}F]FDG SUV ratios (1 d post-injury) and brain volume loss outcome (21 d post-injury) ($p = 0.0283$, n = 9) (**A**) and between I/C ratios of $CMRO_2$ (2 d post-injury) and I/C ratios of histological volume (14 d post-injury) ($p = 0.0123$, n = 5) (**B**) in individual HIE rats.

6 Discussion

6.1 Assessment of PET imaging of the NPP model

6.1.1 *Ex vivo* findings

Ex vivo ARG revealed a higher lesion-to-background uptake of [^{18}F]F-DPA than [^{11}C]PK11195 at inflamed spinal cord sites after PSNL. This specific binding of [^{18}F]F-DPA was significantly reduced by the pre-administration of unlabelled TSPO-selective ligand PK11195. The increased [^{18}F]F-DPA distribution was localised in the dorsal and ventral horn on the ipsilateral side of the injury. This area further coincided with the activated microglial proliferation region on IHC staining with Iba1 antibody, with negligible reactive astrocyte levels detected by GFAP antibody, suggesting that the majority of TSPO uptake was driven by reactive microglia rather than astrocytes. The greater microgliosis detected compared with astrocyte reactivity is probably due to the timing after injury, i.e. day 7 post-injury is the peak of microgliosis and too early to detect astrocyte reactivity. Indeed, Imamoto *et al.* (2013) reported that Iba1-positive cells significantly increased on day 7 and decreased on day 14 after PSNL in rats, whereas GFAP-positive cells only showed an increasing trend on day 7 followed by further enhancement on day 14. It has been proposed that microgliosis mainly contributes to the development of pain, whereas astrogliosis is involved in its maintenance during the transition from the acute to chronic phase (Donnelly *et al*., 2020).

Ex vivo PET of the entire spinal cord removed post-mortem using a β-cube scanner visualised an obvious hot spot of [^{18}F]F-DPA accumulation at the inflammatory site in the spinal cord with a SUV_{max} value of approximately 0.3. Its unilateral tracer distribution coincided with that of the injured side as did *ex vivo* ARG images, suggesting the adequacy of PET imaging in detecting restricted spinal inflammation sites in a rat PSNL model.

6.1.2 *In vivo* findings

In contrast, the *in vivo* PET results with the β-cube scanner failed to visualise increased uptake of [^{18}F]F-DPA in the lesion. This is likely attributable to a low-

frequency background along the entire spinal cord region, representing homogeneous SUV values of approximately 1.0, which is equal to the average tracer concentration administered to the animal. This negative finding was also the case with the Inveon PET scanner. A relatively high level of low-frequency background was also observed along the spinal cord region with this PET scanner, but the background SUV was smaller (approximately 0.7) than with the β-cube scanner.

In vivo PET with [^{11}C]PK11195 also failed to detect inflamed lesions and showed a higher background signal than [^{18}F]F-DPA, which contradicted the previous findings of Imamoto *et al.* (2013). They revealed that *in vivo* [^{11}C]PK11195 PET imaging visualises enhanced tracer uptake in the inflamed region of the lumbar spinal cord at 7 and 14 days after injury in the same rat model (PSNL) using a small animal PET scanner and LabPET-12 Pre-Clinical Imaging System (Gamma Medica, Inc.). On day 7 post-injury, the uptake was further confirmed to be significantly increased in the lumbar region (SUV = 1.16) compared with the reference thoracic region (SUV = 0.77). The reason for the large discrepancy between these two investigations is unclear, although the possibility cannot be completely excluded that minor differences in surgical procedures for modelling (e.g. different suture materials) may have affected the degree of inflammation. Moreover, the administration dose for PET imaging with the β-cube scanner is restricted to 10 MBq, compared to 26–35 MBq in a previous work, which presents a significant limitation. It should also be noted that the limited counting rate performance of the β-cube not only constrains the administered dose but also leads to increased electronic signals due to the significantly larger number of detector crystals.

6.1.3 Challenges in NPP PET imaging

In general, *in vivo* PET imaging of the spinal cord in small experimental rodents is particularly challenging because of its small diameter of 1–3 mm, as well as its anatomical location along the vertebral column and proximity to other highly metabolic organs such as the liver and kidneys (Figure 23), which often accumulate high radioactivity. Indeed, the present *in vivo* [^{18}F]F-DPA PET images indicated greater accumulation in the vertebral body than in the spinal cord region. A recent report revealed that [^{18}F]DPA-714 can detect enhanced bone marrow uptake associated with elevated haematopoietic activation after Ebola virus infection in a primate model (Shah *et al*., 2022). Keller *et al.* (2017) have shown that [^{18}F]F-DPA defluorination is very low, and our *ex vivo* γ-counting results revealed 2-fold higher [^{18}F]F-DPA uptake in vertebrae than in bone from the skull, indicating that this higher *in vivo* uptake can be explained by the large amount of bone marrow in the vertebral body. In line with our *in vivo* PET results showing a higher background signal with [^{11}C]PK11195 than [^{18}F]F-DPA, Gent *et al.* (2014) reported that

[^{11}C]DPA-713 and [^{18}F]DPA-714 achieved markedly lower bone/bone marrow uptake than [^{11}C]PK11195, providing enhanced target-to-background contrast in assessing TSPO expression in arthritic joints of rats using PET.

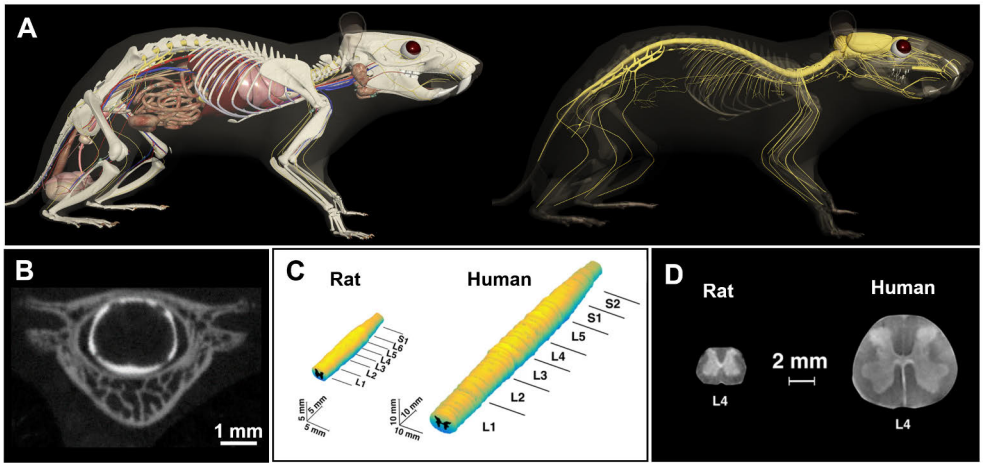

Figure 23 (**A**) Spinal cord anatomy of the rat, which is surrounded by a vertebral column and located close to other organs such as the liver and kidneys. *Created using 3D Rat Anatomy software v. 2.07 (Biosphera)*. (**B**) Coronal image of the rat spinal cord surrounded by the vertebral bone at T8 obtained by CT myelography. (**C**) 3D model of the L1–S1 spinal cords of rats and humans. (**D**) MR coronal images of the spinal cord at L4, comparing rat and human. *Modified from Toossi et al. (2021) and Sotome et al. (2022)*.

However, the effect of spillover from bone/bone marrow does not fully explain the large discrepancy in results between *ex vivo* and *in vivo* findings. Notably, despite the higher spatial resolution of β-cube than Inveon, β-cube showed higher *in vivo* SUV values in all spinal cord regions. This suggests the presence of low-frequency background noise along the spinal cord, originating from radioactivity, distributed not only in the vertebral marrow but also throughout the body. This may be attributed to various potential physical factors, such as scattering, high random rates, and reconstruction algorithms, but individual clarification is beyond the scope of this thesis.

A previous study demonstrated that *in vivo* [^{18}F]F-DPA PET with Inveon successfully visualised an inflamed spinal cord region in a traumatic SCI rat model via direct hemisection of the spinal cord at the thoracic level (Zhang *et al*., 2021). They showed an approximately 4-fold increase in the target/reference SUV ratio at 7 days post-injury, although the effect of up to a 5-fold greater weight of the rats used compared with our rats needs to be taken into account. Taken together, the high background activity in the spinal cord likely masked the subtle tracer uptake

attributed to the mild inflammation in small lesions derived from PSNL, which hampered the exact visual inspection of tracer uptake *in vivo*. For this reason, VOIs were drawn manually in the spinal cord lesion at the estimated anatomical location, unlike for *ex vivo* PET analysis, which may have further disrupted precise semi-quantification analysis. Indeed, *ex vivo* γ-counting did not detect increased SUVs in harvested lumbar spinal cords containing both inflamed and non-inflamed tissues compared with thoracic spinal cords.

Consequently, it is acknowledged that the *in vivo* identification of spinal gliosis originating from PSNL is likely below the detection limit even with the current state-of-the-art high-end PET and the excellent specificity of [^{18}F]F-DPA. Thus, the application of preclinical PET techniques to the *in vivo* tracking of progressive neuroinflammation in NPP, which was the original aim of this thesis, requires further systematic studies by addressing the challenges associated with nonspecific tracer binding and the source of background noise. Such work would be important not only for spinal cord imaging but also for many other fields aiming at sensitive *in vivo* PET imaging of small lesions.

6.2 Methodological advantages of [^{15}O]gas PET imaging

6.2.1 Quantification using a non-invasive approach

A newly installed comprehensive ^{15}O-labelled gas PET setup allowed rats to spontaneously inhale [^{15}O]O_2 and [^{15}O]CO_2 gases mixed with isoflurane without the need for invasive procedures such as tracheotomy for gaseous tracer administration or i.v. cannulation as is the case with [^{15}O]H_2O administration. The gas infusion and evacuation system implemented in the animal holder, orchestrated by a mass flow controller, a radiation detector, and a flow meter, was sufficiently efficient to supply the animals with an adequate amount of isoflurane and radioactivity together with air and cold oxygen. This sophisticated setup made it possible to maintain physiological homeostasis, prevent excess radioactivity from remaining around the animal's body, and ensure radiation safety for staff and facilities. The technique provided good-quality dynamic PET images, allowing quantitative and reproducible estimation of CBF and $CMRO_2$ values by the dual inhalation of [^{15}O]O_2 and [^{15}O]CO_2.

The physiological model-based estimation of metabolised [^{15}O]H_2O in arterial blood after [^{15}O]O_2 inhalation is essential to eliminate extra invasiveness and labour in assessing multiple blood samples. In neonatal rats, [^{15}O]O_2 is rapidly converted into [^{15}O]H_2O via aerobic metabolic processes in brain tissue. Thus, soon after initiating [^{15}O]O_2 inhalation, the metabolised and recirculating [^{15}O]H_2O replaced

[^{15}O]O_2 in arterial blood. Due to the more than 2-fold higher extraction rate of [^{15}O]H_2O to the brain in the capillary bed than [^{15}O]O_2, the contribution of metabolised [^{15}O]H_2O to the brain PET signals exceeds the original [^{15}O]O_2 level during continuous inhalation of [^{15}O]O_2. This phenomenon occurred 3–5 min after [^{15}O]O_2 inhalation initiation in this study. To correct for the contribution of metabolised [^{15}O]H_2O, an additional inhalation of [^{15}O]CO_2, equivalent to i.v. [^{15}O]H_2O administration, was applied, as is common for PET methods utilising a [^{15}O]O_2 inhalation protocol. Simultaneous NLLSF to a pair of dynamic PET images for [^{15}O]O_2 and [^{15}O]CO_2 enabled reliable and reproducible estimations of both $CMRO_2$ and CBF across subjects and each scan time point. One of the PET scans ([^{15}O]CO acquisition) was omitted by assuming a relationship between CBF and CBV, further reducing invasiveness with decreased scan time and total radioactivity exposure to the subject. Importantly, this approach also reduced potential errors in the final $CMRO_2$ estimation caused by possible physiological changes between each scan. One patient with HIE was scanned with [^{15}O]CO to address uncertainty in an accurate CBF–CBV relationship due to possible disease-driven metabolic changes.

6.2.2 Defining the k_w value

The use of a constant rate of recirculating [^{15}O]H_2O, k_w, plays an important role in reducing the logistical complexity of AIF determination (Iida *et al*., 1993; Kudomi *et al*., 2009). The contribution of metabolised [^{15}O]H_2O to the input curve at later periods after 30 s of inhalation of [^{15}O]O_2 was evaluated by assessing whole-blood ([^{15}O]O_2 plus [^{15}O]H_2O) and plasma ([^{15}O]H_2O) radioactivity concentrations. Consistent good fitting agreement was observed between the PET image-derived input function determined from the LV curve and the time-dependent radioactivity concentrations of distinct blood samples. This study obtained an average k_w value of 0.33 min^{-1} with no significant difference between age groups (i.e. P26 and P40). This value was less than half of that obtained in an earlier study on 7–8-week-old rats (Kudomi *et al*., 2009). One reason for this large discrepancy could be due to differences in age and body size, and another more likely reason may be differences in tracer administration procedures. For example, the earlier study used i.v. injection of [^{15}O]O_2–labelled oxyhaemoglobin instead of gaseous [^{15}O]O_2 inhalation. Accordingly, the obtained k_w of 0.33 min^{-1} is considered the best available and reliable value applicable to $CMRO_2$ estimation in all rat subjects at P9–P23 in study **II**.

6.2.3 Implementation of [^{15}O]gas PET in HIE

Overall, the key achievements are non-invasive radiotracer administration without intravascular or tracheal cannulation and quantitative estimation of CBF and $CMRO_2$

using image-derived arterial input function. The minimally invasive nature of this technique allowed repetitive measurements even on consecutive days initiated immediately after the HI insult in vulnerable infant rats at P9–P23. Due to ethical and technical limitations, little has been reported about the normal physiological values of CBF and $CMRO_2$ in healthy-term neonates in humans and experimental animals. To the best of my knowledge, the present [^{15}O]gas PET technique is the first to provide a standard range of time-dependent CBF and $CMRO_2$ changes associated with postnatal age and post-HI injury state in each brain region in rats from neonatal to juvenile age. Indeed, in healthy non-operated rats, both CBF and $CMRO_2$ showed linear increases by more than 2-fold from P9 to P23 along with their physiological maturation. This finding is in line with previous reports, demonstrating lower oxygen consumption measured in infants than in adults in both preclinical (Kreisman, 1989) and clinical studies (Altman *et al*., 1993; Takahashi *et al*., 1999). This growth-associated difference may be due to the escalating cerebral energy demand to compensate for increased Na+ pump activity in neuronal cells (Fukuda *et al*., 1992; Mata *et al.*, 1980) during structural and functional maturation. This fully quantitative approach would be of great value in monitoring the effects of novel treatment strategies that attenuate brain damage without disrupting normal postnatal development. Temporal changes in CBF and $CMRO_2$ associated with brain damage progression in neonatal HIE are discussed in section 6.3.

6.3 Pathophysiological findings of neonatal HIE

Multiparametric and sequential PET assessments detected time-dependent changes in various brain functions over acute, subacute, and chronic phases following HI insult in a neonatal rat model. Specific uptake patterns of [^{15}O]O_2/[^{15}O]CO_2 (cerebral oxygen metabolism and perfusion), [^{18}F]EF5 (hypoxia), [^{18}F]FDG (glucose analogue), and [^{18}F]F-DPA (inflammation) reflected differential pathological stages of neuronal damage progression. Image analysis of spatiotemporal brain function quantitatively estimated CBF and $CMRO_2$ based on [^{15}O]O_2/[^{15}O]CO_2 images and asymmetric SUV ratios over the affected relative to the unaffected hemisphere with other injectable tracers. The key findings at each time point post-injury are as follows: (1) within 6 h post-injury, transiently elevated hypoxia and glucose uptake, as well as decreased CBF, were detected in the injured hemisphere; (2) at 24 h, the elevated glucose uptake became restricted to the hippocampal region and an increasing trend in CBF occurred; (3) at 48 h, a significant drop in CBF and $CMRO_2$ was detected; (4) on day 4, initial inflammation occurred; (5) on day 7, the inflammatory reaction peaked; (6) on day 14, persistently low CBF and $CMRO_2$ levels were still measured; and (7) on day 21, a reduced, but still elevated, inflammatory reaction was detected.

6.3.1 Changes in CBF and $CMRO_2$

After an initial decrease in CBF in the ipsilateral hemisphere, a transient increase was detected at 24 h after injury. This result is in line with the reperfusion phase known to occur through the circle of Willis as compensatory collateral circulation within the first 24 h after HIE (Ohshima *et al*., 2012) and/or due to vasodilatation that may cause hyperperfusion injury (Marchal *et al*., 1996). At 48 h post-injury, both CBF and $CMRO_2$ in the affected hemisphere showed a significant decrease, reaching their lowest levels, presumably reflecting the peak in cellular necrosis and apoptosis, which reportedly occurs at 24–72 h after HI insult (Vannucci *et al*., 2005; Nakajima *et al*., 2000; Northingto *et al*., 2001). Thereafter, both CBF and $CMRO_2$ showed a continuous increase from day 2 until day 14. Despite this trend, CBF and $CMRO_2$ remained at significantly lower levels compared with their contralateral hemisphere and in non-operated control animals. This may reflect age-dependent growth and maturation of brain tissue that, at least in part, survived the secondary energy failure phase. Adult rodents do not exhibit such a time-dependent increase in CBF and $CMRO_2$ after ischaemic brain injury (Temma *et al.,* 2017). In contrast, the I/C $CMRO_2$ ratio showed no significant temporal changes from day 2 onwards. This long-term reduction in the $CMRO_2$ ratio indicates a permanent decrease in the oxygen metabolic rate at the injury site. Despite this decrease, these cells were still able to maintain a critical energy consumption rate, as no hypoxic brain areas or major changes in [^{18}F]FDG uptake were detected 2–3 days after injury.

Histological evaluation of brain tissue loss measured after the last [^{15}O]O_2 PET scan on day 14 after injury revealed reasonable spatial agreement with areas of significantly reduced oxygen metabolism and brain damage. A linear relationship between brain volume loss and the I/C $CMRO_2$ ratio was also observed 2 weeks after injury. These results indicate that PET imaging of oxygen metabolism at a later stage after injury might be a valuable measure for evaluating the severity of HIE. However, oxygen hypometabolism results reported in this study must be interpreted with caution as damage to the BBB, cell death, oxidative stress, and inflammation may have caused liquefaction, necrosis, and oedema in brain tissue. Hence, reduced oxygen metabolism may not only reflect cellular metabolism but also changes in morphological structures. Region-specific changes in CBF and $CMRO_2$ levels may be of interest to further understand regional vulnerability in brain metabolic function, especially in the HIE model, which results in varying levels of injury severity.

6.3.2 Hypoxic brain areas

Hypoxia imaging enabled early detection of cerebral hypoxia on the injury day. A uniformly elevated [^{18}F]EF5 uptake was detected throughout the affected hemisphere following [^{18}F]EF5 injection before hypoxia exposure. This finding

ensured that hypoxia occurred in the injured hemispheres of HIE animals. When [^{18}F]EF5 was injected immediately after hypoxia exposure and allowed to distribute for 2 h, an increased uptake was found in cortical regions. This local uptake probably reflects the most severe brain injury area as the rest of the hemisphere, at least in part, and recovers after being release from hypoxic conditions. Both uptake patterns disappeared within 24 h.

Previous findings using another hypoxia tracer, [^{18}F]FMISO, in an adult ischaemic stroke model also showed specific tracer accumulation in the affected cortex (Takasawa *et al*., 2007; Williamson *et al*., 2013). Lee *et al.* (2012) conducted hypoxia imaging in the acute and subacute phases after hypoxia–ischaemia in neonatal rats using a gamma camera with Tc-99m-HL91. Consistent with the present findings, the authors observed increased Tc-99m-HL91 uptake in the affected cortex in the early phase from 2 h to 20 h post-injury, which diminished in the late phase at 44 h.

6.3.3 Changes in brain [^{18}F]FDG uptake

Within 6 h after the HI insult, an increased I/C ratio of [^{18}F]FDG uptake was observed in the hippocampus and cortex of the ipsilateral hemisphere. Subsequently, at 24 h after injury, the [^{18}F]FDG uptake ratio became less conspicuous, but a slightly increased uptake ratio was observed in the hippocampus. This transiently elevated [^{18}F]FDG uptake ratio detected in damaged brain regions is in agreement with previous experimental studies using the Rice–Vannucci model, demonstrating an increased cerebral metabolic rate of glucose (CMRglc) in the focal lesion within 3–12 h post-HI insult (Vannucci *et al*., 1994; Gilland *et al*., 1998). Other studies also revealed transient upregulation of the neuronal brain glucose transporter isoform, GLUT-3, with (Vannucci *et al*., 1996) or without (Zovein *et al*., 2004) an increase in GLUT-1 within 4 h following HI injury in neonatal rats and mice, which resolved at 24 h post-insult. The transport of glucose across the BBB into the brain is mediated primarily by GLUT1, whereas GLUT 3 mainly regulates neuronal glucose transportation and utilisation (Vannucci *et al*., 1997). Decreased CBF levels were observed in the corresponding areas of the ipsilateral hemisphere within 6 h post-insult coinciding with the increased [^{18}F]FDG uptake phase. Collectively, the transiently increased [^{18}F]FDG uptake detected is speculated to be a compensatory response against the initially reduced blood supply and hypoxia by facilitating glucose transport into cells and/or across the BBB to maintain cellular oxidative metabolism for subsequent neuronal survival. Notably, abnormal hypermetabolism is also linked to increased seizure activity (Chugani, 2021). Another likely explanation is [^{18}F]FDG uptake in early infiltrating macrophages and microgliosis in response to regional cerebral oxygen shortages, as evidenced in a rat model of neurodegenerative disease (Xiang *et al*., 2021).

The present [^{18}F]FDG uptake showed no interhemispheric difference at 7 days post-insult, whereas histological analysis showed neuronal losses with the inflammatory response in the affected hemisphere. Recent studies using a middle cerebral artery occlusion (MCAO) rat model suggested that the contribution of glucose consumption of inflammatory cells to [^{18}F]FDG signals may hide hypometabolism with any accuracy in regions with neuronal damage (Fukumoto *et al*., 2011; Backes *et al*., 2016). Possible changes in metabolic and homeostatic inflammatory function in the contralateral hemisphere with growth should also be considered. A quantitative kinetic approach to assess regional brain [^{18}F]FDG uptake along with maturation at shorter intervals after insult would lead to an advanced interpretation of the deranged [^{18}F]FDG uptake in relation to inflammation, cellular necrosis, and apoptosis. However, several methodological challenges should be addressed, for example, the difficulty in obtaining accurate image-derived AIFs from such small neonatal rats, attributed to the high [^{18}F]FDG accumulation in the surrounding myocardium.

6.3.4 Inflammatory response

The [^{18}F]F-DPA uptake revealed intense inflammation in the injured hemisphere during the subacute and chronic phases. Elevated uptake was observed on day 4, peaked on day 7, and remained detectable until day 21. These results are in agreement with previous findings showing TSPO overexpression in microglia during the subacute neuroinflammation phase 3–7 days after injury (Dickens *et al*., 2014). Similarly, in an adult rat model of cerebral ischaemia, PET imaging of TSPO with [^{18}F]VUIIS1008 and [^{18}F]DPA-714 detected neuroinflammation from day 3, and this increased uptake became maximal at day 7 and started to decrease at day 14 following MCAO (Pulagam *et al*., 2017). In contrast, de Lange *et al.* (2018) failed to detect acute neuroinflammation using [^{18}F]GE180 within 32 h of global hypoxia in newborn piglets. The current study revealed that the $CMRO_2$ reduction was milder in the peri-infarct region in which increased microglial activation was detected by Iba1 staining. This relationship could be further investigated by combining [^{15}O]gas with [^{18}F]F-DPA imaging to clarify the time- and age-dependent role of post-ischaemic inflammation, as inflammatory cascades have been reported to exacerbate neural damage in HIE (Liu *et al*., 2013; Zhu *et al*., 2009).

6.3.5 Predictive value of PET for neonatal HIE

The increased uptake of [^{18}F]FDG on 1 day after injury was correlated with greater brain volume loss, as determined by histological evaluation 21 days later. This indicates that brain tissues with increased glucose uptake are at risk of developing

manifest infarction. Contrary to this finding, a previous study reported that decreased [^{18}F]FDG uptake at 72 h post-injury predicted impaired cognition and a worse outcome in a HIE rat model (Odorcyk *et al*., 2020). The relevance and role of glucose hyper- and hypometabolism in the early phase after injury warrant further investigation.

The current study showed that a reduced $CMRO_2$ level at 48 h after injury correlated with brain volume loss observed 14 days later. Oshima *et al.* (2012) revealed that CBF, measured by laser speckle imaging, at 24 h after injury predicts brain damage severity and outcome in a HIE model. In contrast, the current study showed no correlation between CBF at 24 h and brain volume loss at day 14.

Overall, this study found that both increased [^{18}F]FDG uptake and decreased oxygen metabolism within 48 h may have prognostic value, facilitating early diagnostic decision-making and therapeutic intervention before irreversible tissue damage occurs.

6.4 Limitations and future perspectives

6.4.1 Limitations

There are several potential limitations in all three studies. In study **I**, sufficient A_m in the synthesis of TSPO tracers is particularly important in the challenge to identify subtle accumulations in the neuropathic pain model. Due to the limited number of binding sites, the effective accumulation is directly proportional to the A_m or specific radioactivity. In study **I**, the A_m of [^{18}F]F-DPA was relatively low (1–4 GBq/µmol), which might have negatively influenced the *in vivo* results in the PSNL model. The electrophilic ^{18}F-fluorination method used for synthesizing [^{18}F]F-DPA typically results in lower A_m compared to nucleophilic approach. In a previous study, however, [^{18}F]F-DPA demonstrated significantly higher tracer uptake in the brain of transgenic APP/PS1-21 mice compared to wild type, in which the A_m at the time of injection was 2.25 ± 0.96 GBq/µmol with injected mass of 38 ± 15 µg/kg (Keller *et al*., 2020). Noteworthily, [^{11}C]PK11195 was also unable to detect lesions, even with much higher A_m. Regardless, it is essential to administer an appropriate balance of mass and activity to reliably assess specific binding in the target organ of a given animal model. Additional systematic investigation is therefore needed.

In study **II**, the age of the rat pups used to determine the k_w value ranged from P25 to P40 and were hence older and heavier than HIE pups (P9–P23), which were too small for repeated blood sampling required to determine the k_w value. The k_w value did not differ between P25 and P40 age pups, but it cannot be ruled out that the value differs for younger and smaller pups. This must be considered when interpreting the current results because the k_w value is critical to quantify CBF and

$CMRO_2$. Although the numerical simulation analysis by changing k_w by ±20% revealed negligible ranges of change in CBF and $CMRO_2$ estimations, a more systematic error propagation study is needed in future work. An indirect calorimeter utilising a ventilated chamber (Assaad *et al*., 2014; Even *et al*., 2012) would allow assessment of the k_w value without the need for blood sampling by assuming whole-body oxygen metabolism from O_2 consumption and CO_2 production, as demonstrated previously (Kudomi *et al*., 2009).

The β-cube scanner has high spatial resolution and sensitivity, enabling reliable quantification analysis of experimental rodents. The scanner is compact and light, allowing it to be relocated close to cyclotron facilities. However, it has limitations. The closed animal holder prevents thorough vital monitoring, which is essential especially in the [^{15}O]gas PET study. Physiological conditions are unlikely constant during the entire [^{15}O]gas PET scanning protocol, and possible transient changes in CBF and/or $CMRO_2$ may cause systematic errors during long scan times.

Study **III** employed three PET tracers, [^{18}F]EF5, [^{18}F]FDG, and [^{18}F]F-DPA, each of which has its own limitations. A major drawback of nitroimidazole tracers, especially in the study of cerebral ischaemia, is their slow tissue kinetics, which requires at least 2 h to reach equilibrium in rodents. In addition, due to the lipophilic properties of [^{18}F]EF5, background uptake in the brain is relatively high. Hence, rapid haemodynamic and metabolic changes causing hypoxia may not be detectable. Furthermore, nitroimidazole-based hypoxia tracers bind to macromolecules under relatively low hypoxia levels (< 5–10 mmHg), i.e. only severe hypoxia can be detected (Lawrentschuk *et al*., 2005; Zimny *et al*., 2006).

Although [^{18}F]FDG is the most commonly used PET tracer for imaging glucose uptake in normal brains, several aspects must be considered in the interpretation of diseased images attributed to its non-specific accumulation. Any cell types using glucose take up [^{18}F]FDG, thereby reflecting the net sum of glucose uptake in the tissue under investigation. Typically, dividing and inflammatory cells, in addition to cells that consume glucose under normal conditions, are [^{18}F]FDG avid. The physiological state (e.g. fasting state, temperature, cognitive activity) of the subject also has a significant impact on the arterial blood time-activity and the uptake of [^{18}F]FDG to the brain.

As the rat pups used in study **III** were still lactating, it was not possible to regulate glucose levels, e.g. by fasting before the [^{18}F]FDG scan. Blood glucose levels were measured on the study days and were fairly stable in most pups, although some fluctuations did occur. A stable glucose level is essential for using SUV values in assessing [^{18}F]FDG uptake, serving as a reference for regional glucose metabolism in both healthy and diseased brain tissues. It is also crucial to account for the plasma glucose levels and the individual arterial input functions in the SUV calculation. It

was thus decided to use the I/C SUV ratios in study **III** because of the lack of this information.

While SUV measurements, which provide a semiquantitative assessment of normalized radioactivity concentration in PET images, are easily accessible and user-friendly, they can be affected by a range of biological and technological factors. The volume of distribution (V_T), derived from an arterial plasma input function, is regarded as the gold standard for quantifying radioligands like [^{18}F]F-DPA and [^{11}C]PK11195 binding (Parente *et al*., 2016). However, arterial sampling presents several challenges in rodents, as it requires cannulating either the femoral or carotid artery (Laforest *et al*., 2005). While this is feasible for single-scan studies, it poses significant difficulties for longitudinal experiments particularly on the neonatal rat experiments in study **III**. As for study **I**, the challenge of estimating image-derived input function from the LV chamber (Lanz *et al*., 2014) or the A-V shunt method, along with continuous monitoring of arterial blood in the catheter tube (Weber *et al*., 2002), may be of value. Further studies are necessary to confirm the validity of using SUV values and I/C ratios of SUVs.

6.4.2 Alternative PET tracers for neuroinflammation

Despite the well-established role of TSPO PET tracers in imaging gliosis in numerous neurological disorders, several challenges remain in the ongoing search for the 'perfect' tracer. TSPO expression also occurs in endothelial and astrocyte cells, and some tracers have a low signal-to-noise ratio and are sensitive to genetic polymorphisms in humans. Alternative potential PET tracers targeting other aspects of neuroinflammation beyond TSPO are extensively under development (Janssen *et al*., 2018). Recently, the utility of [^{11}C]SMW139, a P2X7R-targeting PET tracer, was proposed for capturing specific glial phenotypes in the early onset of chronic inflammatory lesions in an autoimmune encephalomyelitis rat model of multiple sclerosis (Beaino *et al*., 2020). For ischaemic brain injury studies, differentiation of acute inflammation in the infarcted core from subsequent remodelling reactions in the peri-infarcted area could provide new insights into innovative therapeutic approaches. For example, PET tracers targeting matrix metalloproteinases and cannabinoid type 2 receptors may discriminate earlier inflammatory responses at 24 h after MCAO compared with TSPO tracers (Zinnhardt *et al*., 2015; Hosoya *et al.*, 2017).

6.4.3 Future technical perspectives

A PET scanner with a higher counting rate may have enabled more advanced findings. In the NPP study, the high random rate may have been a source of low-

frequency bias. This is at least partly due to the limited maximal dose (~10 MBq) that can be used in the β-cube. The limited slew rate (~8 Mcps) for transferring coincidence signals in the electronic circuit was also a bottleneck in the [^{15}O]gas PET study, in which a continuous inhalation protocol was employed. Moreover, a PET scanner with faster electronics would allow a single PET scan session for the dual inhalation of [^{15}O]O_2 followed by [^{15}O]CO_2 at a short interval, as demonstrated previously (Kudomi *et al*., 2013; Iguchi *et al*., 2018). Such a protocol would reduce the total anaesthesia duration, minimise the radiation exposure, and improve the physiological stability of animals. It will also allow parametric imaging with a much shorter acquisition period, as has been done in a recent study (Murayama *et al*., 2024).

Above mentioned technical advancements will also benefit future clinical applications. Conventional ^{15}O-gas PET tests have been logistically complex, requiring lengthy testing periods and the simultaneous management of production, quality control, and administration of three gaseous tracers, along with the need for arterial blood sampling. Additionally, the absence of dedicated analysis software complicated the process of image calculation. The findings of the present study have addressed these longstanding issues, and efforts are now focused on implementing the technology in clinical settings. Additionally, the reduced radiation exposure of ^{15}O-gas compared to other tracers is a significant benefit.

However, protocols must be developed that address ethical concerns related to radiation exposure from CT scans. To achieve this, the utilization of gamma rays and X-rays emitted from trace amounts of Lu-177 in PET detectors has recently become viable for research purpose (Teimoorisichani *et al*., 2022; Sari *et al*., 2022). Simultaneous PET/MRI imaging offers the benefit of significantly reduced radiation exposure since it eliminates the need for a CT scan. Additionally, this method can track the infant's movements, allowing the procedure to be performed without anaesthesia (Andersen *et al*., 2019). These technical advancements may facilitate the use of ^{15}O-gas, [^{18}F]FDG, and [^{18}F]EF5 PET for early identification of cellular abnormalities and tracking progress after treatment during the neonatal period in clinical settings. Additionally, assessing neuroinflammation through [^{18}F]F-DPA uptake may help pinpoint patients who could benefit from anti-inflammatory therapies.

6.4.4 Animals

Although PSNL has shown good reproducibility between subjects in the development of pain via spinal gliosis, an alternative NPP animal model may permit *in vivo* PET monitoring. For example, alternative sciatic nerve injury approaches such as nerve ligation at the more proximal site to the spinal cord like the SNL model

and bilateral nerve ligation would represent a larger lesion with a more severe inflammation magnitude, which could be visualised by *in vivo* [^{18}F]F-DPA PET. The use of more human-like size animal models, such as e.g. pigs, could yield enhanced *in vivo* [^{18}F]F-DPA uptake in the spinal cord. Regarding the HIE model, it does not mimic all pathophysiological aspects that occur in neonatal patients, as such severe CBF reduction is not accompanied in clinical practise and the resulting brain injury is unilateral. Given the collateral circulation impact, interhemispheric ratio analysis may have been biased, especially in the acute phase. Another issue is the relatively small sample size, especially in the technically challenging [^{15}O]gas PET study, which was performed in the practically limited imaging slots available at our facility. Thus, the obtained results may be affected by a small degree of bias. However, changes in cerebral oxygen metabolism in response to HI insult were consistent across individuals and time points. A single [^{15}O]gas PET scan protocol with a shorter scan time would help to increase the sample size, thereby enhancing the statistical power of future studies assessing advanced prognosis with greater variations in infarct levels.

6.4.5 Anaesthesia

General anaesthesia is inevitable in most preclinical *in vivo* imaging studies, whereas almost all clinical PET studies are conducted in the awake state. For repeated longitudinal experiments, isoflurane is recommended because of its easy control of anaesthetic depth and recovery post-anaesthesia. Anaesthetic agents have a direct impact on mitochondrial function (Kajimoto *et al*., 2014), and some preclinical investigations revealed that isoflurane exposure evokes gliosis and alters the development of pain circuits (Li *et al*., 2023). Additionally, isoflurane has been shown to pose a CBF autoregulation derangement effect, which could be a confounding factor in measuring cerebral haemodynamics (Wang *et al*., 2010). Chen *et al.* (2011) further suggested a correlation between isoflurane exposure time and decreased brain infarction in the HIE model because of its neuroprotective properties. Alternative anaesthetic agents may minimise these undesirable effects.

7 Conclusions

I. [^{18}F]F-DPA demonstrated higher specificity than [^{11}C]PK11195 in detecting inflamed lesions in the spinal cord of PSNL rats. *Ex vivo* PET imaging and autoradiographic evaluation allowed the visualisation of distinct hot spots in the lesion. However, *in vivo* imaging of relatively low-grade inflammation in spinal cord lesions remains limited in small animals because of the insufficient signal-to-background uptake ratio relative to high low-frequency background.

II. A novel ^{15}O-labelled gas inhalation PET setup enabled a fully quantitative assessment of temporal changes in CBF and $CMRO_2$ in a HIE rat model. This completely non-invasive imaging methodology is novel and useful for a wide range of preclinical and clinical studies. A particular application of this approach could be the *in vivo* follow-up of disease progression to develop early therapeutic interventions and monitor responses.

III. *In vivo* PET imaging utilising the [^{15}O]gas PET setup combined with 'traditional' imaging of hypoxia, glucose uptake, and inflammation, was demonstrated to be a powerful method for detecting distinct pathophysiological processes occurring after HI injury in rat neonates. Increased [^{18}F]FDG uptake and decreased oxygen metabolism in the early phase of HIE development correlated with the severity of brain damage at a later phase, indicating the potential predictive value of PET imaging. Moreover, this methodology can be valuable in the evaluation of new neonatal HIE treatment approaches in preclinical settings and may also, in the future, be used for early outcome prediction in clinical settings.

Acknowledgements

This thesis work was conducted at the Medicity Research Laboratory, University of Turku and Turku PET Centre. I am deeply grateful to Professor Juhani Knuuti, Director of the Turku PET Centre, and Adjunct Professor Jukka Kemppainen, Head of the Department of Clinical Physiology and Nuclear Medicine, for providing me with the opportunity to conduct my research and for granting access to the facilities. I also wish to acknowledge the financial support I received from the University of Turku Doctoral Programme in Clinical Research (DPCR), the Turku University Foundation, the Instrumentarium Tiedesäätiö, and the JSPS KAKENHI Grant Numbers JP17K15794 and JP21KK0183, which allowed me to focus on my research and complete this dissertation.

I extend my deepest gratitude to my supervisors, Visiting Professor Hidehiro Iida, Adjunct Professor Tove Grönroos, and Adjunct Professor Emrah Yatkin, for their unwavering support and guidance throughout my dissertation journey. Professor Iida, your passion for research has profoundly influenced my academic path and inspired me to pursue my studies in this beautiful country, Finland. Thank you for encouraging me to take this bold leap, and for guiding me every step of the way. Tove, your invaluable advice, thoughtful feedback, and steadfast mentorship have been crucial in achieving my goal, and I am profoundly grateful for the time and care you've dedicated to my academic growth. Emrah, your commitment to ethical research practices and your dedication to fostering a supportive and collaborative research environment have greatly enriched my experience and expanded my understanding of the field.

I am also sincerely grateful to Research Director Patricia Iozzo from the Italian National Research Council (CNR) and Professor Olof Eriksson from the Uppsala University for their thorough and thoughtful review of my thesis. Your feedback and valuable suggestions have significantly enhanced the quality of my work. I am deeply honoured that Professor Gitte Moos Knudsen from the University of Copenhagen has graciously accepted the role of my esteemed opponent. I truly appreciate her taking the time to engage critically with this work.

I would also like to express my heartfelt gratitude to Professors Pirjo Nuutila and Mika Teräs, members of the follow-up committee, for their invaluable guidance and

support throughout the entire duration of my doctoral programme. Their expertise and insight in the field of nuclear medicine were crucial in shaping my research and in overcoming the complexities of my project.

I am particularly grateful to Vilhelmiina Parikka for generously sharing her expertise and deep knowledge throughout the HIE project. Your willingness to offer ideas, constructive feedback, and encouragement has had a profound impact on my research. I would also like to express my sincere appreciation for the opportunity to collaborate with Emma Saha on the HIE project, which led to a publication that is a key component of my dissertation.

I am deeply thankful to Thomas Keller and Professor Olof Solin for their invaluable contributions to the radiosynthesis of the tracer and for sharing their specialized knowledge. I also wish to acknowledge the dedicated personnel at the Accelerator Laboratory and the Radiopharmaceutical Chemistry Laboratory for their essential role in the production of the tracers used in my research.

I would like to express my profound gratitude to Jukka Ihalainen, Heidi Partanen, Tuula Tolvanen, Ari Hietanen, Esa Kokkomäki, and Stefan Johansson for their essential contributions to the GasPET project. Your expertise and collaborative spirit were pivotal to the success of this complex and challenging endeavour.

My heartfelt thanks go to all the personnel and colleagues at the Turku PET Centre Preclinical PET unit—Merja Haaparanta-Solin, Aake Honkaniemi, Jatta Helin, Marko Vehmanen, Mira Eisala, Susanne Vainio, Francisco Lopez Picon, Luciana Kovacs dos Santos, Heidi Nykanen, Richard Aarnio, Maxwell Miner, Obada Al-Zghool, Anna Jalo, Sanni Tuominen, Petra Ketonen as well as all the students and post-docs— whose practical help and camaraderie have been a constant source of support throughout my doctoral studies. Working alongside such a talented and dedicated group has been an incredibly enriching experience. I would like to extend a special thank you to Aake for his exceptional assistance in managing the PET scan; without his support, none of this work would have been possible.

I would also like to thank all co-authors and collaborators, including Associate Professor Nobuyuki Kudomi, Professor Masahiro Tsuji, Professor Shigehiko Kanaya, Johan Rajander, and Eliisa Löyttyniemi. Additionally, I acknowledge the Histology Core Facility of the Institute of Biomedicine, University of Turku for their technical support in histological analysis.

My sincere appreciation extends to Heidi Liljenbäck at the Turku PET Centre, and Varpu Laine, Joonas Khabbal, Ella Kujala, Petra-Paulina Kahila, and the entire animal laboratory staff at the University of Turku Central Animal Facility (UTUCAL) for their crucial assistance throughout my animal laboratory work. Your expertise, professionalism, and attention to animal welfare have been indispensable in conducting my experiments, and I am thankful for the supportive and caring environment you provided for my work.

I also wish to thank Adjunct Professors Miho Nakamura and Pere Puigbò from the University of Turku for their ongoing support and friendship. Your guidance, both academic and personal, has greatly enriched this journey, making it far more fulfilling and enjoyable.

Finally, I would like to express my heartfelt gratitude to my family and friends, both in Finland and Japan. Your support and friendship have made this journey not only possible but also profoundly meaningful. A special note of thanks to my parents, Takashi and Yuriko, whose constant encouragement and belief in me have been an enduring source of strength. I am eternally grateful for all you have given me.

Turku, December 2024
Saeka Shimochi

References

Albertsson, A. M., Bi, D., Duan, L., Zhang, X., Leavenworth, J. W., Qiao, L., Zhu, C., *et al*. (2014) The immune response after hypoxia-ischemia in a mouse model of preterm brain injury. *J Neuroinflammation*, 11:153.

Altman, D. I., Perlman, J. M., Volpe, J. J., & Powers, W. J. (1993) Cerebral oxygen metabolism in newborns. *Pediatrics*, 92:99–104.

Andersen, J. B., Lindberg, U., Olesen, O. V., Benoit, D., Ladefoged, C. N., Larsson, H. B., Højgaard, L., *et al*. (2019) Hybrid PET/MRI imaging in healthy unsedated newborn infants with quantitative rCBF measurements using ^{15}O-water PET. *J Cereb Blood Flow Metab*, 39:782–793.

Arlicot, N., Vercouillie, J., Ribeiro, M. J., Tauber, C., Venel, Y., Baulieu, J. L., Maia, S., *et al*. (2012) Initial evaluation in healthy humans of [^{18}F]DPA-714, a potential PET biomarker for neuroinflammation. *Nucl Med Biol*, 39:570–578.

Arora, S., & Tantia, P. (2019) Physiology of Oxygen Transport and its Determinants in Intensive Care Unit. *Indian J Crit Care Med*, 23:172–177.

Assaad, H., Yao, K., Tekwe, C. D., Feng, S., Bazer, F. W., Zhou, L., Carroll, R. J., *et al*. (2014) Analysis of energy expenditure in diet-induced obese rats. *Front Biosci*, 19:967–985.

Ayubcha, C., Amanullah, A., Patel, K. H., Teichner, E., Gokhale, S., Marquez-Valenzuela, U., Werner, T. J., & Alavi, A. (2023) Stroke and molecular imaging: a focus on FDG-PET. *Am J Nucl Med Mol Imaging*, 13:51–63.

Backes, H., Walberer, M., Ladwig, A., Rueger, M. A., Neumaier, B., Endepols, H., Hoehn, M., *et al*. (2016) Glucose consumption of inflammatory cells masks metabolic deficits in the brain. *Neuroimage*, 128:54–62.

Barthel, H., Villemagne, V. L., & Drzezga, A. (2022) Future directions in molecular imaging of neurodegenerative disorders. *J Nucl Med*, 63:68S–74S.

Baskin, A., Buchegger, F., Seimbille, Y., Ratib, O., & Garibotto, V. (2015) PET molecular imaging of hypoxia in ischemic stroke: An update. *Curr Vasc Pharmacol*, 13:209–217.

Batista, C. E., Chugani, H. T., Juhász, C., Behen, M. E., & Shankaran, S. (2007) Transient hypermetabolism of the basal ganglia following perinatal hypoxia. *Pediatr Neurol*, 36:330–333.

Beaino, W., Janssen, B., Kooijman, E., Vos, R., Schuit, R. C., O'Brien-Brown, J., Kassiou, M., *et al*. (2020) PET imaging of P2X7R in the experimental autoimmune encephalomyelitis model of multiple sclerosis using [^{11}C]SMW139. *J neuroinflammation*, 17:300.

Bennett, G. J., & Xie, Y. K. (1988) A peripheral mononeuropathy in rat that produces disorders of pain sensation like those seen in man. *Pain*, 33:87–107.

Bergeron, M., Evans, S. M., Sharp, F. R., Koch, C. J., Lord, E. M., & Ferriero, D. M. (1999) Detection of hypoxic cells with the 2-nitroimidazole, EF5, correlates with early redox changes in rat brain after perinatal hypoxia-ischemia. *Neuroscience*, 89:1357–1366.

Bonsack, F., & Sukumari-Ramesh, S. (2018) TSPO: An evolutionarily conserved protein with elusive functions. *Int J Mol Sci*, 19:1694.

Boutin, H., Prenant, C., Maroy, R., Galea, J., Greenhalgh, A. D., Smigova, A., Cawthorne, C., *et al*. (2013) [^{18}F]DPA-714: direct comparison with [^{11}C]PK11195 in a model of cerebral ischemia in rats. *PloS One*, 8:e56441.

Chapman J. D. (1979) Hypoxic sensitizers--implications for radiation therapy. *N Engl J Med*, 301:1429–1432.

Chapman, J. D., Franko, A. J., & Sharplin, J. (1981) A marker for hypoxic cells in tumours with potential clinical applicability. *Br J Cancer*, 43:546–550.

Chauveau, F., Boutin, H., Van Camp, N., Dollé, F., & Tavitian, B. (2008) Nuclear imaging of neuroinflammation: a comprehensive review of [^{11}C]PK11195 challengers. *Eur J Nucl Med Mol Imaging*, 35:2304–2319.

Chen, H., Burris, M., Fajilan, A., Spagnoli, F., Tang, J., & Zhang, J. H. (2011) Prolonged exposure to isoflurane ameliorates infarction severity in the rat pup model of neonatal hypoxia-ischemia. *Transl Stroke Res*, 2:382–390.

Chugani H. T. (2021) Hypermetabolism on pediatric PET scans of brain glucose metabolism: what does it signify? *J Nucl Med*, 62:1301–1306.

Colloca, L., Ludman, T., Bouhassira, D., Baron, R., Dickenson, A. H., Yarnitsky, D., Freeman, R., *et al*. (2017) Neuropathic pain. *Nat Rev Dis Primers*, 3:17002.

Conti, M., & Eriksson, L. (2016) Physics of pure and non-pure positron emitters for PET: a review and a discussion. *EJNMMI Phys*, 3:8.

Cotten, C. M., Fisher, K., Malcolm, W., Gustafson, K. E., Cheatham, L., Marion, A., Greenberg, R., & Kurtzberg, J. (2023) A pilot phase I trial of allogeneic umbilical cord tissue-derived mesenchymal stromal cells in neonates with hypoxic-ischemic encephalopathy. *Stem Cells Transl Med*, 12:355–364.

Decosterd, I., & Woolf, C. J. (2000) Spared nerve injury: an animal model of persistent peripheral neuropathic pain. *Pain*, 87:149–158.

de Lange, C., Malinen, E., Qu, H., Johnsrud, K., Skretting, A., Saugstad, O. D., & Munkeby, B. H. (2012) Dynamic FDG PET for assessing early effects of cerebral hypoxia and resuscitation in new-born pigs. *Eur J Nucl Med Mol Imaging*, 39:792–799.

de Lange, C., Solberg, R., Holtedahl, J. E., Tulipan, A., Barlinn, J., Trigg, W., Wickstrøm, T., *et al*. (2018) Dynamic TSPO-PET for assessing early effects of cerebral hypoxia and resuscitation in new born pigs. *Nucl Med Biol*, 66:49–57.

Dienel G. A. (2019) Brain glucose metabolism: integration of energetics with function. *Physiol Rev*, 99:949–1045.

Dickens, A. M., Vainio, S., Marjamäki, P., Johansson, J., Lehtiniemi, P., Rokka, J., Rinne, J., *et al*. (2014) Detection of microglial activation in an acute model of neuroinflammation using PET and radiotracers 11C-(R)-PK11195 and 18F-GE-180. *J Nucl Med*, 55:466–472.

Dingley, J., Tooley, J., Liu, X., Scull-Brown, E., Elstad, M., Chakkarapani, E., Sabir, H., & Thoresen, M. (2014) Xenon ventilation during therapeutic hypothermia in neonatal encephalopathy: a feasibility study. *Pediatrics*, 133:809–818.

Dixon, B. J., Reis, C., Ho, W. M., Tang, J., & Zhang, J. H. (2015) Neuroprotective strategies after neonatal hypoxic ischemic encephalopathy. *Int J Mol Sci*, 16:22368–22401.

Donnelly, C. R., Andriessen, A. S., Chen, G., Wang, K., Jiang, C., Maixner, W., & Ji, R. R. (2020) Central nervous system targets: glial cell mechanisms in chronic pain. *Neurotherapeutics*, 17:846–860.

Echeverry, S., Shi, X. Q., Yang, M., Huang, H., Wu, Y., Lorenzo, L. E., Perez-Sanchez, J., *et al*. (2017) Spinal microglia are required for long-term maintenance of neuropathic pain. *Pain*, 158:1792–1801.

Eskola, O., Grönroos, T. J., Forsback, S., Tuomela, J., Komar, G., Bergman, J., Härkönen, P., *et al*. (2012) Tracer level electrophilic synthesis and pharmacokinetics of the hypoxia tracer [^{18}F]EF5. *Mol Imaging Biol*, 14:205–212.

Even, P. C., & Nadkarni, N. A. (2012) Indirect calorimetry in laboratory mice and rats: principles, practical considerations, interpretation and perspectives. *Am J Physiol Regul Integr Comp Physiol*, 303:459–476.

Fan, Z., Calsolaro, V., Atkinson, R. A., Femminella, G. D., Waldman, A., Buckley, C., Trigg, W., *et al*. (2016) Flutriciclamide (^{18}F-GE180) PET: first-in-human PET study of novel third-generation in vivo marker of human translocator protein. *J Nucl Med*, 57:1753–1759.

Fukuda, A., & Prince, D. A. (1992) Postnatal development of electrogenic sodium pump activity in rat hippocampal pyramidal neurons. *Brain Res Dev Brain Res*, 65:101–114.

Fukumoto, D., Hosoya, T., Nishiyama, S., Harada, N., Iwata, H., Yamamoto, S., & Tsukada, H. (2011) Multiparametric assessment of acute and subacute ischemic neuronal damage: a small animal positron emission tomography study with rat photochemically induced thrombosis model. *Synapse*, 65:207–214.

Gent, Y. Y., Weijers, K., Molthoff, C. F., Windhorst, A. D., Huisman, M. C., Kassiou, M., Jansen, G., *et al*. (2014) Promising potential of new generation translocator protein tracers providing enhanced contrast of arthritis imaging by positron emission tomography in a rat model of arthritis. *Arthritis Res Ther*, 16:R70.

Gilland, E., Bona, E., & Hagberg, H. (1998) Temporal changes of regional glucose use, blood flow, and microtubule-associated protein 2 immunostaining after hypoxia-ischemia in the immature rat brain. *J Cereb Blood Flow Metab,* 18:222–228.

Greco, P., Nencini, G., Piva, I., Scioscia, M., Volta, C. A., Spadaro, S., Neri, M., *et al*. (2020) Pathophysiology of hypoxic-ischemic encephalopathy: a review of the past and a view on the future. *Acta Neurol Belg*, 120:277–288.

Hamdy, N., Eide, S., Sun, H. S., & Feng, Z. P. (2020) Animal models for neonatal brain injury induced by hypoxic ischemic conditions in rodents. *Exp Neurol*, 334:113457.

He, W. J., Cui, J., Du, L., Zhao, Y. D., Burnstock, G., Zhou, H. D., & Ruan, H. Z. (2012) Spinal P2X(7) receptor mediates microglia activation-induced neuropathic pain in the sciatic nerve injury rat model. *Behav Brain Res*, 226:163–170.

Hildebrandt, I. J., Su, H., & Weber, W. A. (2008) Anesthesia and other considerations for in vivo imaging of small animals. *ILAR J*, 49:17–26.

Ho Kim, S., & Mo Chung, J. (1992) An experimental model for peripheral neuropathy produced by segmental spinal nerve ligation in the rat. *Pain*, 50:355–363.

Hosoya, T., Fukumoto, D., Kakiuchi, T., Nishiyama, S., Yamamoto, S., Ohba, H., Tsukada, H., *et al*. (2017) In vivo TSPO and cannabinoid receptor type 2 availability early in post-stroke neuroinflammation in rats: a positron emission tomography study. *J Neuroinflammation*, 14:69.

Huang, J., Xie, Y., Sun, X., Zeh, H. J., 3rd, Kang, R., Lotze, M. T., & Tang, D. (2015) DAMPs, ageing, and cancer: The 'DAMP Hypothesis'. *Ageing Res Rev*, 24:3–16.

Huang, L., Zhao, F., Qu, Y., Zhang, L., Wang, Y., & Mu, D. (2017) Animal models of hypoxic-ischemic encephalopathy: optimal choices for the best outcomes. *Rev Neuroscience*, 28:31–43.

Iguchi, S., Moriguchi, T., Yamazaki, M., Hori, Y., Koshino, K., Toyoda, K., Teuho, J., *et al*. (2018) System evaluation of automated production and inhalation of ^{15}O-labeled gaseous radiopharmaceuticals for the rapid ^{15}O-oxygen PET examinations. *EJNMMI Phy*, 5:37.

Iida, H., Jones, T., & Miura, S. (1993) Modeling approach to eliminate the need to separate arterial plasma in oxygen-15 inhalation positron emission tomography. *J Nucl Med*, 34:1333–1340.

Imamoto, N., Momosaki, S., Fujita, M., Omachi, S., Yamato, H., Kimura, M., Kanegawa, N., *et al*. (2013) [^{11}C]PK11195 PET imaging of spinal glial activation after nerve injury in rats. *Neuroimage*, 79:121–128.

Inoue, K., & Tsuda, M. (2018) Microglia in neuropathic pain: cellular and molecular mechanisms and therapeutic potential. *Nat Rev Neurosci*, 19:138–152.

Jacobs, S. E., Berg, M., Hunt, R., Tarnow-Mordi, W. O., Inder, T. E., & Davis, P. G. (2013) Cooling for newborns with hypoxic ischaemic encephalopathy. *Cochrane Database Syst Rev*, 2013:CD003311.

Jaggi, A. S., Jain, V., & Singh, N. (2011) Animal models of neuropathic pain. *Fundam Clin Pharmacol*, 25:1–28.

Janssen, B., Vugts, D. J., Windhorst, A. D., & Mach, R. H. (2018) PET imaging of microglial activation-beyond targeting TSPO. *Molecules*, 23:607.

Jensen, T. S., Baron, R., Haanpää, M., Kalso, E., Loeser, J. D., Rice, A. S. C., & Treede, R. D. (2011) A new definition of neuropathic pain. *Pain*, 152:2204–2205.

Kabatas, S., Civelek, E., Savrunlu, E. C., Kaplan, N., Boyalı, O., Diren, F., Can, H., *et al*. (2021) Feasibility of allogeneic mesenchymal stem cells in pediatric hypoxic-ischemic encephalopathy: Phase I study. *World J Stem Cells*, 13:470–484.

Kajimoto, M., Atkinson, D. B., Ledee, D. R., Kayser, E. B., Morgan, P. G., Sedensky, M. M., Isern, N. G., *et al*. (2014) Propofol compared with isoflurane inhibits mitochondrial metabolism in immature swine cerebral cortex. *J Cereb Blood Flow Metab*, 34:514–521.

Karimi, S. A., Zahra, F. T., & Martin, L. J. (2024) IUPHAR review: Navigating the role of preclinical models in pain research. *Pharmacol Res*, 200:107073.

Keller, T., Krzyczmonik, A., Forsback, S., Picón, F. R. L., Kirjavainen, A. K., Takkinen, J., Rajander, *et al*. (2017) Radiosynthesis and Preclinical Evaluation of [^{18}F]F-DPA, A Novel Pyrazolo[1,5a]pyrimidine Acetamide TSPO Radioligand, in Healthy Sprague Dawley Rats. *Mol Imaging Biol*, 19:736–745.

Keller, T., López-Picón, F. R., Krzyczmonik, A., Forsback, S., Kirjavainen, A. K., Takkinen, J. S., Alzghool, O., *et al*. (2018) [^{18}F]F-DPA for the detection of activated microglia in a mouse model of Alzheimer's disease. *Nucl Med Biol*, 67:1–9.

Keller, T., López-Picón, F. R., Krzyczmonik, A., Forsback, S., Takkinen, J. S., Rajander, J., Teperi, S., *et al*. (2020) Comparison of high and low molar activity TSPO tracer [^{18}F]F-DPA in a mouse model of Alzheimer's disease. *J Cereb Blood Flow Metab*, 40:1012–1020.

Kierdorf, K., & Prinz, M. (2017) Microglia in steady state. J Clin Invest, 127:3201–3209.

Kobayashi, K., Yamanaka, H., Yanamoto, F., Okubo, M., & Noguchi, K. (2012) Multiple P2Y subtypes in spinal microglia are involved in neuropathic pain after peripheral nerve injury. *Glia*, 60:1529–1539.

Koehler, R. C., Yang, Z. J., Lee, J. K., & Martin, L. J. (2018) Perinatal hypoxic-ischemic brain injury in large animal models: Relevance to human neonatal encephalopathy. *J Cereb Blood Flow Metab*, 38:2092–2111.

Kohno, K., Shirasaka, R., Yoshihara, K., Mikuriya, S., Tanaka, K., Takanami, K., Inoue, K., *et al*. (2022) A spinal microglia population involved in remitting and relapsing neuropathic pain. *Science*, 376:86–90.

Kono, H., & Rock, K. L. (2008). How dying cells alert the immune system to danger. *Nat Rev Immunol*, 8:279–289.

Kreisl, W. C., Fujita, M., Fujimura, Y., Kimura, N., Jenko, K. J., Kannan, P., Hong, J., *et al*. (2010) Comparison of [^{11}C]-(R)-PK 11195 and [^{11}C]PBR28, two radioligands for translocator protein (18 kDa) in human and monkey: implications for positron emission tomographic imaging of this inflammation biomarker. *Neuroimage*, 49:2924–2932.

Kreisman, N. R., Olson, J. E., Horne, D. S., & Holtzman, D. (1989) Cerebral oxygenation and blood flow in infant and young adult rats. *Am. J. Physiol*, 256:R78–R85.

Krishnamoorthy S, Schmall JP, Surti S. (2017) PET Physics and Instrumentation. Basic science of PET imaging. Ed. Magdy M. Khalil. Springer, Switzerland, 173–197.

Kudomi, N., Hayashi, T., Watabe, H., Teramoto, N., Piao, R., Ose, T., Koshino, K., *et al*. (2009) A physiologic model for recirculation water correction in $CMRO_2$ assessment with $^{15}O_2$ inhalation PET. *J Cereb Blood Flow Metab*, 29:355–364.

Kudomi, N., Hirano, Y., Koshino, K., Hayashi, T., Watabe, H., Fukushima, K., Moriwaki, H., *et al*. (2013) Rapid quantitative CBF and $CMRO_2$ measurements from a single PET scan with sequential administration of dual ^{15}O-labeled tracers. *J Cereb Blood Flow Metab*, 33:440–448.

Kurinczuk, J. J., White-Koning, M., & Badawi, N. (2010) Epidemiology of neonatal encephalopathy and hypoxic-ischaemic encephalopathy. *Early Hum Dev*, 86:329–338.

Laforest, R., Sharp, T. L., Engelbach, J. A., Fettig, N. M., Herrero, P., Kim, J., Lewis, J. S., *et al*. (2005) Measurement of input functions in rodents: challenges and solutions. *Nucl. Med. Biol.*, 32:679–685.

Lanz, B., Poitry-Yamate, C., & Gruetter, R. (2014) Image-derived input function from the vena cava for ^{18}F-FDG PET studies in rats and mice. *J. Nucl. Med*, 55:1380–1388.

Largeau, B., Dupont, A. C., Guilloteau, D., Santiago-Ribeiro, M. J., & Arlicot, N. (2017) TSPO PET imaging: from microglial activation to peripheral sterile inflammatory diseases? *Contrast Media Mol Imaging*, 2017:6592139.

Lawrentschuk, N., Poon, A. M., Foo, S. S., Putra, L. G., Murone, C., Davis, I. D., Bolton, D. M., & Scott, A. M. (2005) Assessing regional hypoxia in human renal tumours using 18F-fluoromisonidazole positron emission tomography. *BJU Int*, 96:540–546.

Le Fur, G., Perrier, M. L., Vaucher, N., Imbault, F., Flamier, A., Benavides, J., Uzan, A., *et al*. (1983) Peripheral benzodiazepine binding sites: effect of PK11195, 1-(2-chlorophenyl)-N-methyl-N-(1-methylpropyl)-3-isoquinolinecarboxamide. I. In vitro studies. *Life Sci*, 32:1839–1847.

Lee, B. H., Won, R., Baik, E. J., Lee, S. H., & Moon, C. H. (2000) An animal model of neuropathic pain employing injury to the sciatic nerve branches. *Neuroreport*, 11:657–661.

Lee, B. F., Wang, L. W., Lin, S. H., Jhuo, T. J., Chiu, N. T., Huang, C. C., Hsia, C. C., & Shen, L. H. (2012) Tc-99m-HL91 imaging in the early detection of neuronal injury in a neonatal rat model of hypoxic ischemia. *Crit Care Med*, 40:1930–1938.

Levine S. (1960) Anoxic-ischemic encephalopathy in rats. *Am J Pathol*, 36:1–17.

Lin, L., Wang, X., & Yu, Z. (2016) Ischemia-reperfusion injury in the brain: Mechanisms and potential therapeutic strategies. *Biochem Pharmacol*, 5:213.

Li, Q., Mathena, R. P., Li, F., Dong, X., Guan, Y., & Mintz, C. D. (2023) Effects of early exposure to isoflurane on susceptibility to chronic pain are mediated by increased neural activity due to actions of the mammalian target of the rapamycin pathway. *Int J Mol Sci*, 24:13760.

Little, P. V., Arnberg, F., Jussing, E., Lu, L., Ingemann Jensen, A., Mitsios, N., Mulder, J., *et al*. (2021) The cellular basis of increased PET hypoxia tracer uptake in focal cerebral ischemia with comparison between [^{18}F]FMISO and [^{64}Cu]CuATSM. *J Cereb Blood Flow Metab*, 41:617–629.

Liu, F., & McCullough, L. D. (2013) Inflammatory responses in hypoxic ischemic encephalopathy. *Acta Pharmacol Sin*, 34:1121–1130.

López-Picón, F. R., Keller, T., Bocancea, D., Helin, J. S., Krzyczmonik, A., Helin, S., Damont, A., *et al*. (2022) Direct comparison of [^{18}F]F-DPA with [^{18}F]DPA-714 and [^{11}C]PBR28 for neuroinflammation imaging in the same Alzheimer's disease model mice and healthy controls. *Mol Imaging Biol*, 24:157–166.

Marchal, G., Furlan, M., Beaudouin, V., Rioux, P., Hauttement, J. L., Serrati, C., de la Sayette, V., *et al*. (1996) Early spontaneous hyperperfusion after stroke. A marker of favourable tissue outcome? *Brain*, 119: 409–419.

Martín, A., Boisgard, R., Thézé, B., Van Camp, N., Kuhnast, B., Damont, A., Kassiou, M., *et al*. (2010) Evaluation of the PBR/TSPO radioligand [^{18}F]DPA-714 in a rat model of focal cerebral ischemia. *J Cereb Blood Flow Metab*, 30: 230–241.

Martin J. B. (1999) Molecular basis of the neurodegenerative disorders. *N Engl J Med*, 340:1970–1980.

Maruyama, D., Iida, H., Koshino, K., Nakagawa, J., Morita, Y., Hashimura, N., Mori, H., *et al*. (2024) Comparative Analysis of Peri-Nidal Cerebral Blood Flow and Metabolism Using a Novel Quantitative ^{15}O-PET Method in Patients with arteriovenous Malformations. *J Cereb Blood Flow Metab*, in press.

Mason, N. S., & Mathis, C. A. (2003) Positron emission tomography radiochemistry. *Neuroimaging Clin N Am*, 13:671–687.

Mata, M., Fink, D. J., Gainer, H., Smith, C. B., Davidsen, L., Savaki, H., Schwartz, W. J., & Sokoloff, L. (1980) Activity-dependent energy metabolism in rat posterior pituitary primarily reflects sodium pump activity. *J Neurochem*, 34:213–215.

McRae, A., Gilland, E., Bona, E., & Hagberg, H. (1995) Microglia activation after neonatal hypoxic-ischemia. *Brain Res. Dev. Brain Res*, 84:245–252.

Millar, L. J., Shi, L., Hoerder-Suabedissen, A., & Molnár, Z. (2017) Neonatal hypoxia ischaemia: mechanisms, models, and therapeutic challenges. *Front Cell Neurosci*, 11:78.

Miranda, A., Bertoglio, D., Stroobants, S., Staelens, S., & Verhaeghe, J. (2021) Translation of preclinical PET imaging findings: challenges and motion correction to overcome the confounding effect of anesthetics. *Front Med*, 8:753977.

Murnion B. P. (2018) Neuropathic pain: current definition and review of drug treatment. *Aust Prescr*, 41:60–63.

Nair, J., & Kumar, V. H. S. (2018) Current and emerging therapies in the management of hypoxic ischemic encephalopathy in neonates. *Children*, 5:99.

Nakajima, W., Ishida, A., Lange, M. S., Gabrielson, K. L., Wilson, M. A., Martin, L. J., Blue, M. E., & Johnston, M. V. (2000) Apoptosis has a prolonged role in the neurodegeneration after hypoxic ischemia in the newborn rat. *J Neurosci*, 20:7994–8004.

Narita, M., Yoshida, T., Nakajima, M., Narita, M., Miyatake, M., Takagi, T., Yajima, Y., & Suzuki, T. (2006) Direct evidence for spinal cord microglia in the development of a neuropathic pain-like state in mice. *J Neurochem*, 97:337–1348.

Nguyen, A. T., & Kim, H. K. (2023) Recent developments in PET and SPECT radiotracers as radiopharmaceuticals for hypoxia tumors. *Pharmaceutics*, 15:1840.

Northington, F. J., Ferriero, D. M., Graham, E. M., Traystman, R. J., & Martin, L. J. (2001) Early neurodegeneration after hypoxia-ischemia in neonatal rat is necrosis while delayed neuronal death is apoptosis. *Neurobiol Dis*, 8:207–219.

Odorcyk, F. K., Duran-Carabali, L. E., Rocha, D. S., Sanches, E. F., Martini, A. P., Venturin, G. T., Greggio, S., *et al*. (2020). Differential glucose and beta-hydroxybutyrate metabolism confers an intrinsic neuroprotection to the immature brain in a rat model of neonatal hypoxia ischemia. *Exp Neurol*, 330:113317.

Ohshima, M., Tsuji, M., Taguchi, A., Kasahara, Y., & Ikeda, T. (2012) Cerebral blood flow during reperfusion predicts later brain damage in a mouse and a rat model of neonatal hypoxic-ischemic encephalopathy. *Exp Neurol*, 233:481–489.

Parente, A., Feltes, P. K., Vállez García, D., Sijbesma, J. W., Moriguchi Jeckel, C. M., Dierckx, R. A., de Vries, E. F., & Doorduin, J. (2016) Pharmacokinetic Analysis of ^{11}C-PBR28 in the Rat Model of Herpes Encephalitis: Comparison with (R)-^{11}C-PK11195. *J. Nucl. Med*, 57:785–791.

Patel, S. D., Pierce, L., Ciardiello, A. J., & Vannucci, S. J. (2014) Neonatal encephalopathy: pre-clinical studies in neuroprotection. *Biochem Soc Trans*, 42:564–568.

Perez, R. C., Kim, D., Maxwell, A. W. P., & Camacho, J. C. (2023) Functional imaging of hypoxia: PET and MRI. *Cancers*, 15:3336.

Pulagam, K. R., Colás, L., Padro, D., Plaza-García, S., Gómez-Vallejo, V., Higuchi, M., Llop, J., & Martín, A. (2017). Evaluation of the novel TSPO radiotracer [^{18}F] VUIIS1008 in a preclinical model of cerebral ischemia in rats. *EJNMMI Res*, 7:93.

Rainio, O., Han, C., Teuho, J., Nesterov, S. V., Oikonen, V., Piirola, S., Laitinen, T., *et al*. (2023) Carimas: An Extensive Medical Imaging Data Processing Tool for Research. *J Digit Imaging*, 36:1885–1893.

Ransohoff R. M. (2016) How neuroinflammation contributes to neurodegeneration. *Science*, 353:777–783.

Rice, J. E., 3rd, Vannucci, R. C., & Brierley, J. B. (1981) The influence of immaturity on hypoxic-ischemic brain damage in the rat. *Ann Neurol*, 9:131–141.

Rissanen, E., Tuisku, J., Rokka, J., Paavilainen, T., Parkkola, R., Rinne, J. O., & Airas, L. (2014) In vivo detection of diffuse inflammation in secondary progressive multiple sclerosis using PET Imaging and the radioligand ^{11}C-PK11195. *J Nucl Med*, 55:939–944.

Rong, J., Haider, A., Jeppesen, T. E., Josephson, L., & Liang, S. H. (2023) Radiochemistry for positron emission tomography. *Nat Commun*, 14:3257.

Sari, H., Teimoorisichani, M., Mingels, C., Alberts, I., Panin, V., Bharkhada, D., Xue, S., *et al*. (2022) Quantitative evaluation of a deep learning-based framework to generate whole-body attenuation maps using LSO background radiation in long axial FOV PET scanners. *Eur J Nucl Med Mol Imaging*, 49:4490–4502.

Scholz, J., & Woolf, C. J. (2002) Can we conquer pain? *Nat Neurosci*, 5 Suppl:1062–1067.

Scholz, J., Finnerup, N. B., Attal, N., Aziz, Q., Baron, R., Bennett, M. I., Benoliel, R., *et al.* Classification committee of the neuropathic pain special interest group (NeuPSIG) (2019) The IASP classification of chronic pain for ICD-11: chronic neuropathic pain. *Pain*, 160:53–59.

Schroeter, M., Dennin, M. A., Walberer, M., Backes, H., Neumaier, B., Fink, G. R., & Graf, R. (2009) Neuroinflammation extends brain tissue at risk to vital peri-infarct tissue: a double tracer [^{11}C]PK11195- and [^{18}F]FDG-PET study. *J Cereb Blood Flow Metab*, 29:1216–1225.

Seltzer, Z., Dubner, R., & Shir, Y. (1990) A novel behavioral model of neuropathic pain disorders produced in rats by partial sciatic nerve injury. *Pain*, 43:205–218.

Selway L. D. (2010) State of the science: hypoxic ischemic encephalopathy and hypothermic intervention for neonates. *Adv Neonatal Care,* 10:60–68.

Semple, B. D., Blomgren, K., Gimlin, K., Ferriero, D. M., & Noble-Haeusslein, L. J. (2013) Brain development in rodents and humans: Identifying benchmarks of maturation and vulnerability to injury across species. *Prog Neurobiol*, 106–107:1–16.

Shah, S., Sinharay, S., Patel, R., Solomon, J., Lee, J. H., Schreiber-Stainthorp, W., Basuli, F., *et al*. (2022) PET imaging of TSPO expression in immune cells can assess organ-level pathophysiology in high-consequence viral infections. *Proc Natl Acad Sci U S A*, 119:e2110846119.

Sheldon, R. A., Sedik, C., & Ferriero, D. M. (1998) Strain-related brain injury in neonatal mice subjected to hypoxia-ischemia. *Brain Res*, 810:114–122.

Shi, Y., Zhao, J. N., Liu, L., Hu, Z. X., Tang, S. F., Chen, L., & Jin, R. B. (2012) Changes of positron emission tomography in newborn infants at different gestational ages, and neonatal hypoxic-ischemic encephalopathy. *Pediatr Neurol*, 46:116–123.

Sotome, A., Kadoya, K., Suzuki, Y., & Iwasaki, N. (2022) Spinal canal and spinal cord in rat continue to grow even after sexual maturation: Anatomical study and molecular proposition. *Int J Mol Sci*, 23:16076.

Takahashi, T., Shirane, R., Sato, S., & Yoshimoto, T. (1999) Developmental changes of cerebral blood flow and oxygen metabolism in children. *AJNR Am J Neuroradiol*, 20:917–922.

Takasawa, M., Beech, J. S., Fryer, T. D., Hong, Y. T., Hughes, J. L., Igase, K., Jones, P. S., *et al*. (2007) Imaging of brain hypoxia in permanent and temporary middle cerebral artery occlusion in the rat using ^{18}F-fluoromisonidazole and positron emission tomography: a pilot study. *J Cereb Blood Flow Metab,* 27:679–689.

Takasawa, M., Moustafa, R. R., & Baron, J. C. (2008) Applications of nitroimidazole in vivo hypoxia imaging in ischemic stroke. *Stroke*, 39:1629–1637.

Takkinen, J. S., López-Picón, F. R., Al Majidi, R., Eskola, O., Krzyczmonik, A., Keller, T., Löyttyniemi, E., *et al*. (2017) Brain energy metabolism and neuroinflammation in ageing APP/PS1-21 mice using longitudinal 18F-FDG and 18F-DPA-714 PET imaging. *J Cereb Blood Flow Metab*, 37:2870–2882.

Teimoorisichani, M., Panin, V., Rothfuss, H., Sari, H., Rominger, A., & Conti, M. *et al*. (2022) A CT-less approach to quantitative PET imaging using the LSO intrinsic radiation for long-axial FOV PET scanners. *Med. Phys*., 49:309–323.

Temma, T., Kuge, Y., Sano, K., Kamihashi, J., Obokata, N., Kawashima, H., Magata, Y., & Saji, H. (2008) PET O-15 cerebral blood flow and metabolism after acute stroke in spontaneously hypertensive rats. *Brain Res*, 1212:18–24.

Temma, T., Iida, H., Hayashi, T., Teramoto, N., Ohta, Y., Kudomi, N., Watabe, H., *et al*. (2010) Quantification of regional myocardial oxygen metabolism in normal pigs using positron emission tomography with injectable (15)O-O(2). *Eur J Nucl Med Mol Imaging*, 37:377–385.

Temma, T., Yamazaki, M., Miyanohara, J., Shirakawa, H., Kondo, N., Koshino, K., Kaneko, S., & Iida, H. (2017) Sequential PET estimation of cerebral oxygen metabolism with spontaneous respiration of 15O-gas in mice with bilateral common carotid artery stenosis. *J Cereb Blood Flow Metab,* 37:3334–3343.

Ter-Pogossian M. M. (1992) The origins of positron emission tomography. *Nucl Med Semin*, 22:140–149.

Tetorou, K., Sisa, C., Iqbal, A., Dhillon, K., & Hristova, M. (2021) Current therapies for neonatal hypoxic-ischaemic and infection-sensitised hypoxic-ischaemic brain damage. *Front Synaptic Neurosci*, 13:709301.

Teuho, J., Riehakainen, L., Honkaniemi, A., Moisio, O., Han, C., Tirri, M., Liu, S., *et al*. (2020) Evaluation of image quality with four positron emitters and three preclinical PET/CT systems. *EJNMMI Res*, 10:155.

Thorngren-Jerneck, K., Ohlsson, T., Sandell, A., Erlandsson, K., Strand, S. E., Ryding, E., & Svenningsen, N. W. (2001) Cerebral glucose metabolism measured by positron emission tomography in term newborn infants with hypoxic ischemic encephalopathy. *Pediatr Res*, 49:495–501.

Thorngren-Jerneck, K., Ley, D., Hellström-Westas, L., Hernandez-Andrade, E., Lingman, G., Ohlsson, T., Oskarsson, G., *et al*. (2001) Reduced postnatal cerebral glucose metabolism measured by PET after asphyxia in near term fetal lambs. *J Neurosci Res*, 66:844–850.

Toossi, A., Bergin, B., Marefatallah, M., Parhizi, B., Tyreman, N., Everaert, D. G., Rezaei, S., *et al*. (2021) Comparative neuroanatomy of the lumbosacral spinal cord of the rat, cat, pig, monkey, and human. *Sci Rep*, 11:1955.

Tsuda, M., Shigemoto-Mogami, Y., Koizumi, S., Mizokoshi, A., Kohsaka, S., Salter, M. W., & Inoue, K. (2003) P2X4 receptors induced in spinal microglia gate tactile allodynia after nerve injury. *Nature*, 424:778–783.

Tsuda, M., Ueno, H., Kataoka, A., Tozaki-Saitoh, H., & Inoue, K. (2008) Activation of dorsal horn microglia contributes to diabetes-induced tactile allodynia via extracellular signal-regulated protein kinase signaling. *Glia*, 56:378–386.

Tsuda, M., Masuda, T., Tozaki-Saitoh, H., & Inoue, K. (2013) P2X4 receptors and neuropathic pain. *Front Cell Neurosci*, 7:191.

Van Camp, N., Lavisse, S., Roost, P., Gubinelli, F., Hillmer, A., & Boutin, H. (2021) TSPO imaging in animal models of brain diseases. *Eur J Nucl Med Mol Imaging*, 49:77–109.

van Hecke, O., Austin, S. K., Khan, R. A., Smith, B. H., & Torrance, N. (2014) Neuropathic pain in the general population: a systematic review of epidemiological studies. *Pain*, 155:654–662.

Vannucci, R. C., Yager, J. Y., & Vannucci, S. J. (1994) Cerebral glucose and energy utilization during the evolution of hypoxic-ischemic brain damage in the immature rat. *J Cereb Blood Flow Metab,* 14:279–288.

Vannucci, S. J., Seaman, L. B., & Vannucci, R. C. (1996) Effects of hypoxia-ischemia on GLUT1 and GLUT3 glucose transporters in immature rat brain. *J Cereb Blood Flow Metab,* 16:77–81.

Vannucci, S. J., Maher, F., & Simpson, I. A. (1997) Glucose transporter proteins in brain: delivery of glucose to neurons and glia. *Glia*, 21:2–21.

Vannucci, S. J., & Hagberg, H. (2004) Hypoxia-ischemia in the immature brain. *J Exp Biol*, 207:3149–3154.

Vannucci, R. C., Brucklacher, R. M., & Vannucci, S. J. (2005) Glycolysis and perinatal hypoxic-ischemic brain damage. *Dev Neurosci*, 27:185–190.

Vannucci, R. C., & Vannucci, S. J. (2005) Perinatal hypoxic-ischemic brain damage: evolution of an animal model. *Dev Neurosci*, 27:81–86.

Vannucci, S. J., & Back, S. A. (2022) The Vannucci model of hypoxic-ischemic injury in the neonatal rodent: 40 years later. *Dev Neurosci*, 44:186–193.

Wang, Z., Schuler, B., Vogel, O., Arras, M., & Vogel, J. (2010) What is the optimal anesthetic protocol for measurements of cerebral autoregulation in spontaneously breathing mice?. *Exp Brain Res*, 207:249–258.

Watabe, T., Shimosegawa, E., Watabe, H., Kanai, Y., Hanaoka, K., Ueguchi, T., Isohashi, K., *et al*. (2013) Quantitative evaluation of cerebral blood flow and oxygen metabolism in normal anesthetized rats: 15O-labeled gas inhalation PET with MRI Fusion. *J Nucl Med,* 54:283–290.

Weber, B., Burger, C., Biro, P., & Buck, A. (2002) A femoral arteriovenous shunt facilitates arterial whole blood sampling in animals. *Eur J Nucl Med Mol Imaging*, 29:319–323.

Williamson, D. J., Ejaz, S., Sitnikov, S., Fryer, T. D., Sawiak, S. J., Burke, P., Baron, J. C., & Aigbirhio, F. I. (2013) A comparison of four PET tracers for brain hypoxia mapping in a rodent model of stroke. *Nucl Med Biol*, 40:338–344.

Wodarski, R., Clark, A. K., Grist, J., Marchand, F., & Malcangio, M. (2009) Gabapentin reverses microglial activation in the spinal cord of streptozotocin-induced diabetic rats. *Eur J Pain,* 13:807–811.

Wu, Y. W., Comstock, B. A., Gonzalez, F. F., Mayock, D. E., Goodman, A. M., Maitre, N. L., Chang, T., *et al*. (2022) Trial of erythropoietin for hypoxic-ischemic encephalopathy in newborns. N Engl J Med, 387:148–159.

Xiang, X., Wind, K., Wiedemann, T., Blume, T., Shi, Y., Briel, N., Beyer, L., *et al*. (2021) Microglial activation states drive glucose uptake and FDG-PET alterations in neurodegenerative diseases. *Sci Transl Med*, 13:5640.

Yıldız, E. P., Ekici, B., & Tatlı, B. (2017) Neonatal hypoxic ischemic encephalopathy: an update on disease pathogenesis and treatment. *Expert Rev Neurother*, 17:449–459.

Zhang, L., Zhuang, X., Kotitalo, P., Keller, T., Krzyczmonik, A., Haaparanta-Solin, M., Solin, O., *et al*. (2021) Intravenous transplantation of olfactory ensheathing cells reduces neuroinflammation after spinal cord injury via interleukin-1 receptor antagonist. *Theranostics*, 11:1147–1161.

Zhang, Z., Zhang, Z. Y., Fauser, U., & Schluesener, H. J. (2008) Mechanical allodynia and spinal up-regulation of P2X4 receptor in experimental autoimmune neuritis rats. *Neuroscience*, 152:495–501.

Zhu, C., Qiu, L., Wang, X., Xu, F., Nilsson, M., Cooper-Kuhn, C., Kuhn, H. G., & Blomgren, K. (2009) Age-dependent regenerative responses in the striatum and cortex after hypoxia-ischemia. *J Cereb Blood Flow Metab*, 29:342–354.

Zimny, M., Gagel, B., DiMartino, E., Hamacher, K., Coenen, H. H., Westhofen, M., Eble, M., *et al*. (2006) FDG--a marker of tumour hypoxia? A comparison with [^{18}F]fluoromisonidazole and pO_2-polarography in metastatic head and neck cancer. *Eur J Nucl Med Mol Imaging*, 33:1426–1431.

Zinnhardt, B., Viel, T., Wachsmuth, L., Vrachimis, A., Wagner, S., Breyholz, H. J., Faust, A., *et al*. (2015) Multimodal imaging reveals temporal and spatial microglia and matrix metalloproteinase activity after experimental stroke. *J Cereb Blood Flow Metab,* 35:1711–1721.

Zovein, A., Flowers-Ziegler, J., Thamotharan, S., Shin, D., Sankar, R., Nguyen, K., Gambhir, S., & Devaskar, S. U. (2004) Postnatal hypoxic-ischemic brain injury alters mechanisms mediating neuronal glucose transport. *Am J Physiol Regul Integr Comp Physiol*, 286:R273–R282.

TURUN
YLIOPISTO
UNIVERSITY
OF TURKU

ISBN 978-951-29-9998-9 (PRINT)
ISBN 978-951-29-9999-6 (PDF)
ISSN 0355-9483 (Print)
ISSN 2343-3213 (Online)

Painosalama, Turku, Finland 2024